ABSTRACT

Title of dissertation: A DUAL MODALITY, DCE-MRI AND X-RAY, PHYSICAL PHANTOM FOR QUANTITATIVE EVALUATION OF BREAST IMAGING PROTOCOLS

Melanie Freed, Doctor of Philosophy, 2010

Dissertation directed by: Dr. Aldo Badano
Department of Bioengineering

The current clinical standard for breast cancer screening is mammography. However, this technique has a low sensitivity which results in missed cancers. Dynamic contrast-enhanced magnetic resonance imaging (DCE-MRI) has recently emerged as a promising technique for breast cancer diagnosis and has been reported as being superior to mammography for screening of high-risk women and evaluation of extent of disease. At the same time, low and variable specificity has been documented in the literature as well as a rising number of mastectomies possibly due to the increasing use of DCE-MRI. In this study, we developed and characterized a dual-modality, x-ray and DCE-MRI, anthropomorphic breast phantom for the quantitative assessment of breast imaging protocols. X-ray properties of the phantom were quantitatively compared with patient data, including attenuation coefficients, which matched human values to within the measurement error, and tissue structure using spatial covariance matrices of image data, which were found to be similar in size to patient data. Simulations of the phantom scatter-to-primary ratio (SPR)

were produced and experimentally validated then compared with published SPR predictions for homogeneous phantoms. SPR values were as high as 85% in some areas and were heavily influenced by the heterogeneous tissue structure. MRI properties of the phantom, T_1 and T_2 relaxation values and tissue structure, were also quantitatively compared with patient data and found to match within two error bars. Finally, a dynamic lesion that mimics lesion border shape and washout curve shape was included in the phantom. High spatial and temporal resolution x-ray measurements of the washout curve shape were performed to determine the true contrast agent concentration as a function of time. DCE-MRI phantom measurements using a clinical imaging protocol were compared against the x-ray truth measurements. MRI signal intensity curves were shown to be less specific to lesion type than the x-ray derived contrast agent concentration curves. This phantom allows, for the first time, for quantitative evaluation of and direct comparisons between x-ray and MRI breast imaging modalities in the context of lesion detection and characterization.

A DUAL-MODALITY, DCE-MRI AND X-RAY,
PHYSICAL PHANTOM FOR
QUANTITATIVE EVALUATION OF
BREAST IMAGING PROTOCOLS

by

Melanie Elizabeth Freed

Dissertation submitted to the Faculty of the Graduate School of the
University of Maryland, College Park in partial fulfillment
of the requirements for the degree of
Doctor of Philosophy
2010

Advisory Committee:
Dr. Aldo Badano, Chair/Advisor
Dr. Jacco A. de Zwart
Dr. Jeff H. Duyn
Professor Yu Chen
Professor Yang Tao
Professor Wolfgang Losert

Dedication

To Phil Hinz

for his support and common human decency

at a time when both were in short supply.

To Gene O'Bryan

for always being positive.

Acknowledgments

My journey to complete this Ph.D. has been a long and difficult one and it would have been impossible to reach this point without the people that lifted my spirits and encouraged me to keep going. Thanks to...

...my parents for being such great role models and confidants. For being successful without playing the game. For never putting me down. For being so good at balancing work and life. For raising me to be completely ignorant of society's expectations of me. For being the best source of professional advice. For understanding everything. For making me laugh.

...my brothers for having the courage to follow their dreams.

...Julio for picking me up every day without making me feel like it cost him anything, for always making time to help, and for understanding everything.

...Phil Hinz, to whom this dissertation is dedicated, for standing up for me and for believing in me. Every single day was a struggle to keep going and it was his support that, in the end, pushed me forward. If there was one person that was pivotal in getting me this far, it was him.

...Andreu for being a friend.

...those volleyball guys for a few kind words that were an unlikely source of inspiration.

Table of Contents

List of Tables

List of Figures

List of Abbreviations

2D	two-dimensional
3D	three-dimensional
ACR	American College of Radiology
AIF	arterial input function
AUC	area under the curve
CC	cranio-caudal
CCD	charge-coupled device
CsI	cesium iodide
CT	computed tomography
DCE	dynamic contrast-enhanced
DTPA	diethylene triamine pentaacetic acid
FOM	figure of merit
FOP	fiber-optic plate
FWHM	full width at half the maximum
Gd	gadolinium
HVL	half value layer
IR	inversion recovery
L-BFGS	limited-memory Broyden-Fletcher-Goldfarb-Shanno
LSF	line spread function
MANTIS	monte carlo x-ray electron optical imaging simulation
MRI	magnetic resonance imaging
MPE	mean photon energy
MTF	modulation transfer function
NCI	National Cancer Institute
NNPS	normalized noise power spectrum
PET	positron emission tomography
PRF	point response function
PSF	point spread function
QIBA	Quantitative Imaging Biomarkers Alliance
RMS	root mean squared
ROC	receiver operating characteristic
ROI	region-of-interest
rpm	rotations per minute
RSNA	Radiological Society of North America
SE	spin echo
SEM	scanning electron microscope
SNR	signal-to-noise ratio
SPECT	single photon emission computed tomography
SPR	scatter-to-primary ratio
TE	echo time
TI	inversion time
Tl	thalium
TR	repetition time
USDA	United States Department of Agriculture

Chapter 1

Introduction

With 12% of the US female population expecting to be diagnosed with breast cancer in their lifetime [1], effective screening and early diagnosis of this disease is a major public health concern. The current standard for breast cancer screening and diagnosis is palpation and mammography [2, 3]. A review, published in 2002 by the U.S. Preventative Services Task Force [4], of eight randomized, controlled trials found that x-ray mammography is effective at reducing mortality for women aged 40 and over. Evidence for a benefits of screening was stronger for older women (aged 50-69 years) than for younger women (aged 40-49 years). However, x-ray mammography has a relatively low sensitivity (69-90%) [5], which results in many missed cancers. This is particularly true for young patients with dense breasts that complicate the interpretation of mammograms due to the masking effect of glandular tissue [9, 10]. Additionally, dense breast tissue results in a larger radiation dose during mammography [3] and has been correlated with an elevated risk for developing breast cancer [6, 7, 8]. Therefore, the group with the highest risk of developing breast cancer suffers the highest dose from x-ray mammography while receiving the lowest diagnostic advantage.

With this as a backdrop, breast MR has been rapidly gaining momentum in the breast imaging community. While initial studies in the 1980s using intrinsic tis-

sue contrast methods yielded unimpressive results [5], the introduction of dedicated breast coils, higher magnetic field systems, and Gd-based contrast agents have transformed breast MR into a high-sensitivity method capable of detecting 77-100% of cancers [11]. Dedicated breast coils and higher field systems have helped to increase signal-to-noise, while Gd-based contrast agents have allowed MR to overcome the overlap of intrinsic T_1 and T_2 relaxation values of cancerous and benign tissues. Gd-based contrast agents preferentially increase the signal in lesions as well as provide information about the vasculature around any suspicious regions when time-resolved data is acquired. In this way, DCE-MRI can provide both morphological and kinetic information about a suspected lesion. The inclusion of both of these components has been shown to improve the detection of invasive lesions. A study by Schnall *et al.* [12] showed that the best area under the receiver operating characteristic (ROC) curve (AUC) for a single morphology feature was 0.78 and for a single kinetic feature was 0.66. But when both morphology and kinetic information were combined into a multivariate model, an AUC of 0.88 was achieved. DCE-MRI has been shown to be useful in screening of high-risk women [13, 14] as well as in evaluating the extent of disease [14, 15, 16, 17, 18, 19]. Studies of screening in high-risk women have shown that DCE-MRI can detect cancers that are not visible in either x-ray mammography or ultrasound. In a review of the literature, Kuhl [14] showed that, for screening of high-risk women, the sensitivity of MR imaging ranged from 71-100% as compared to 0-59% for x-ray mammography. For evaluating the extent of disease after diagnosis, MR helps identify additional cancers in 14-27% of patients and unsuspected synchronous cancer in the opposite breast in 3-6% of patients [14].

In response to these recent advancements in breast MR, there has been an enthusiastic reaction both in the medical/scientific community as well as in the public. In 2007, the American Cancer Society released guidelines recommending screening MRI as an adjunct to x-ray mammography for women with a 20-25% lifetime risk of developing breast cancer [11]. A dedicated breast MRI system, manufactured by Aurora Imaging Technology, Inc., has also been approved by the FDA and, as of March 29, 2007, 23 units have been installed at facilities worldwide, with more than double that number expected by the end of that year [20]. In addition, some insurance companies have started to reimburse the cost of breast MR for high-risk patients [21], overcoming a major hurdle for widespread use of the technology. The diagnosis of actress Christina Applegate in August 2008 has also helped bring breast MR into the public eye since MRI was considered key in the early detection of her breast cancer [22].

However, despite the many advances made in DCE-MRI, there are numerous issues that have yet to be fully addressed. Although DCE-MRI demonstrates high sensitivity, it has a well-documented low and highly variable specificity (26%-97%) [17, 23, 24]. A lower specificity results in more false positives which lead to more unnecessary and costly biopsies and procedures. In addition to the obvious burden of additional cost and time incurred from these unnecessary procedures, they also lead to increased patient anxiety. In some cases, after a false positive result from breast MR, patients have opted for mastectomies rather than undergo additional biopsies to verify the test results [25]. DCE-MRI has also been shown to overestimate margins and produce false positives when used in preoperative assessment of

local extent of cancer [17, 18]. Perhaps one of the most compelling controversies of DCE-MRI has been the recent recognition of a link between increased MR use in breast cancer evaluation and an increased number of mastectomies being performed. As a result of studies showing that survival for breast conserving surgery followed by radiotherapy was equivalent to survival after mastectomy, the number of mastectomies being performed had been steadily decreasing during the 1990s and early 2000s [26, 27]. However, the increasing use of MR for breast cancer staging seems to be correlated with an unsettling trend towards a rate of mastectomies that approaches the previous level [26]. Several studies have shown that the addition of DCE-MRI to the evaluation of patients with breast cancer results in more extensive surgery (7.8-33.3%), where a significant fraction (0-53%) of that change in surgical management is later proved unnecessary at histology [25, 28, 29, 30, 31, 32].

In addition to MRI, other emerging x-ray technologies that are under development include breast tomosynthesis and dedicated breast CT. Both of these modalities attempt to improve on the sensitivity of mammography by including additional three-dimensional information and removing some of the confounding tissue overlap that makes interpretation of high breast density mammograms so problematic. Preliminary studies using tomosynthesis have shown improved lesion visibility and reduced recall rate, but may require additional dose [33, 34, 35]. The use of breast CT seems to improve visualization of masses at the expense of visualization of microcalcifications and the use of an intravenously administered, iodinated contrast medium can further improve lesion and malignant microcalcification (malignant lesion that manifests as a microcalcification in mammography) conspicuity

[36, 37].

With such a variety of technologies available, each with its own unique advantages and disadvantages, the ability to perform quantitative performance comparisons is critical in determining the optimal imaging parameters and clinical utility of each modality. The ideal platform for quantitative comparisons would be a well-characterized phantom that can be used to evaluate lesion detection across all of the available modalities. The requirements for such a phantom include the ability to mimic image contrast, tissue structure, and lesion characteristics present in the breast. Image contrast is produced via two different mechanisms in MRI and x-ray imaging which are characterized by different inherent tissue properties; T_1 and T_2 relaxation times for MRI and attenuation coefficient for x ray. Therefore, phantom materials must simultaneously mimic both of these inherent tissue properties. In addition, it is important that the phantom mimics the complex structure between fibroglandular and adipose tissues present in the human breast since this provides a confounding signal that can obscure or emulate lesions, complicating the diagnosis. Lesions included in the phantom must mimic properties that clinicians use to diagnose breast cancer, including border shape and dynamic contrast uptake profiles for MRI. The border shape and dynamic contrast uptake profiles for the lesion model must be well known so that acquired data, and estimations derived from that data, can be quantitatively compared against the true lesion properties.

In this dissertation, we present a phantom that addresses all of the above-described requirements for multi-modality imaging assessment. In Chapter 2, the response of indirect x-ray detectors used in breast imaging systems including mam-

mography breast tomosynthesis, and breast CT are explored. Current modeling efforts in indirect detector response are summarized. Detailed understanding of the influence of x-ray detectors on acquired images is useful for research and development and system optimization. The knowledge gained from investigations presented in this chapter will be applied to the analysis of x-ray phantom images for the quantification of tissue structure in Chapter 5 and to the measurements of the true lesion washout curves in Chapter 6. In this chapter, experimental measurements were made of point responses and light output for CsI scintillator screens and the results were used to validate Monte Carlo predictions using the program MANTIS. Experimental data were acquired at four difference incidence angles and with two different spectra for four screens with different scintillator thicknesses, columnar tilt angles, and substrate types. A quantitative comparison was performed between experimental and simulated PRFs showing that the simulated PRFs provide a better match to the experimental data than symmetric two-dimensional (2D) Gaussians fit to the experimental data itself. Therefore, MANTIS predictions are more representative of experimental data than commonly assumed 2D Gaussian functions and can be used to provide more accurate studies of system characterization and optimization and can be incorporated into image reconstruction approaches.

Chapter 3 is an extension of Chapter 2 and describes the development of an analytical model for indirect detector point response functions. This model can be used to provide more rapid predictions of deterministic CsI detector PRFs than MANTIS and makes real-time system optimizations and reconstructions using this information feasible. The analytical model is x-ray energy and incidence angle dependent

and draws on results from MANTIS to indirectly include complicated interactions that are not explicitly included in the mathematical model. Once the mathematical expression was derived, values of the coefficients were adjusted using a 2D fit to MANTIS-generated results based on a figure-of-merit (FOM) that measures the normalized differences between the MANTIS and analytical model results averaged over a region of interest. This analysis was performed for a monochromatic x-ray energy of 25 keV, a CsI scintillator thickness of 150 μm, and four incidence angles (0, 15, 30, and 45 degrees). The analytical model was found to match MANTIS results much better than a 2D Gaussian fit to the zero-angle PRF. A comparison was also made against experimental data for a 170 μm thick CsI screen and an x-ray energy of 25.6 keV. The analytical model was shown to fit the experimental data about as well as MANTIS. This performance is achieved in less than one millionth the computation time required to generate a comparable PRF with MANTIS.

In Chapter 4, we present the static MRI properties of the phantom. A brief overview of the literature, including a discussion of existing MR breast phantoms, is provided. The phantom construction procedures are discussed as well as the motivation for the choice of phantom materials. T_1 and T_2 relaxation times of the phantom materials were estimated at 1.5 T from inversion recovery and spin-echo scans, respectively, using maximum likelihood methods. Comparison of the phantom relaxation times with human values from the literature shows good agreement, particularly for T_1 values, which are most important for the T_1-weighted images typically used for breast MRI. Stability of the relaxation times was also evaluated over 9 months. Tissue structure of the phantom was quantitatively evaluated by

7

calculating and comparing spatial covariance matrices of phantom and patient images. Comparison of the phantom and patient covariance matrices shows that they have similar image structure within uncertainties due to measurement error and population variations. Finally, a static, enhancing lesion was introduced by creating a hollow, plastic mold with stereolithography and filling it with a gadolinium-doped water solution.

In Chapter 5, we characterize the x-ray properties of the phantom and describe the production of a phantom with a compressed shape as used in mammography. A review of anthropomorphic x-ray phantoms is provided. Mass attenuation coefficients of the phantom materials were estimated using elemental compositions from the USDA National Nutrient Database for Standard Reference and the atomic interaction models from the Monte Carlo code PENELOPE and compared with human values from the literature. The image structure was examined quantitatively by calculating and comparing spatial covariance matrices of phantom and patient mammography images. Finally, a computerized version of the phantom was created by segmenting a computed tomography scan and used to simulate x-ray scatter of the phantom in a mammography geometry. Mass attenuation coefficients of the phantom materials were within 20% and 15% of the values for adipose and glandular tissues, respectively, which is within the estimation error of these values. Tissue structures in the phantom have a similar size to those in patient data, but are slightly larger on average. Correlations in the patient data appear to be longer than those in the phantom data in the anterior-posterior direction, however they are within the error bars of the measurement. Simulated scatter-to-primary ratio values of the

phantom images were as high as 85% in some areas and were strongly affected by the heterogeneous nature of the phantom. Since the MRI properties of the phantom have been previously evaluated in Chapter 4, these measurements complete a set of comprehensive evaluation tests of the phantom for quantitative evaluation of two- and three-dimensional x-ray and MRI breast imaging modalities.

Chapter 6 describes the development of the dynamic lesion component of the phantom for evaluation of dynamic contrast-enhanced MRI. Existing dynamic MR phantoms are discussed. Models for both lesion border shape and washout curve shape are described. The washout curve shape is controlled via a fluid pump that varies the amount of contrast agent solution in the lesion as a function of time. High spatial and temporal resolution x-ray measurements were used to calculate the true concentration of contrast agent in the lesion model over time. The optimal fluid flow rate and the ability of the fluid pump to reproducibly create benign and malignant-shaped washout curves were evaluated. Finally, MRI data were acquired with a clinical imaging sequence and a variety of spatial/temporal resolutions. MRI signal intensity curves are shown to be flatter and less specific to lesion type than the true contrast agent concentration curves, as verified by x rays. Methods for improving the match between the MRI data and the contrast agent concentration curves are discussed.

Chapter 7 provides the conclusion to the thesis and Chapter 8 discusses areas of future work.

Chapter 2

Experimental validation of Monte Carlo (MANTIS) simulated x-ray response of columnar CsI scintillator screens

2.1 Overview

Thallium-activated[1] cesium iodide (CsI:Tl) scintillator screens coupled with optical readout arrays are currently the most commonly implemented detection method for digital x-ray imaging [86]. X rays are absorbed by the CsI:Tl crystal, which then produces a shower of optical photons that are detected with a flat-panel array of amorphous Silicon photodiodes. The crystal itself has a complex columnar structure that directs the optical photons down the thickness of the crystal and improves the detector resolution as compared with unstructured crystals [86, 87, 88]. This columnar structure also affects the point response function (PRF) of the detector in a complex manner that is difficult to model. The PRF fully describes the blurring behavior of the scintillator and is simply the image that results from x rays that are incident on the detector at a single, infinitesimally small point. This definition of the PRF is ambiguous since x rays with different incidence angles will result in dissimilar responses. This fact has lead investigators to provide a more formal analysis of the response function of x-ray detectors that include directionality of the primary beam (see for instance Ref. [89]). Therefore, for

---

[1]Work in this chapter published in Medical Physics [85].

the purpose of the analysis included in this paper, our definition of PRF includes the direction of the incoming x rays. Proper modeling of the PRF and its dependence on scintillator properties is critical to performing rigorous system optimizations that correctly predict image quality and forward-problem image reconstructions that accurately reproduce the imaged object.

To the authors' knowledge, the only computational model that provides a detailed treatment of the internal structure of CsI:Tl columnar scintillators and is capable of predicting the full two-dimensional PRF as a function of the scintillator properties is a package called MANTIS (Monte Carlo x-rAy electroN opTical Imaging Simulation) [90]. Several studies have investigated models of detector performance for megavoltage photons for radiotherapy applications [91, 92, 93, 94, 95]. These studies focus on single- or segmented-crystal scintillators and have been used to simulate light output as well as symmetric detector spread via the modulation transfer function (MTF). Experimental validation of both light output and symmetric detector response has been reported in the cited works. A recently developed Monte Carlo code, PHOTON, for simulating optical photon transport in scintillation detectors was used to model the light output of a single-crystal plastic scintillator for 662 keV gamma rays and was validated with experimental data [96]. The main difference between the code MANTIS and the work cited above is the fact that MANTIS uses a list-mode approach for accounting of energy depositions and optical photon generation in the scintillator and can accommodate a structure with a large number of columns in the scintillator device. A recent study by Blakesley and Speller[97] implemented a Monte Carlo-based model of the full x-ray detection process in flat

panel arrays (both indirect and direct detection types) from generation of the x-ray photons to charge readout and electronic noise in the photodiode layer. However, their model was meant to provide broad comparisons between theoretical detectors and not to give detailed descriptions of detector image quality. For this reason, while their model does provide a simplified treatment of the scintillator internal columnar structure, their model does not produce two-dimensional PRFs capable of fully capturing the blurring behavior of the detector.

MANTIS is a publicly available Monte Carlo simulation code capable of tackling the problem of detailed simulation of the imaging properties of these columnar CsI:Tl scintillator screens [90]. It provides a complete Monte Carlo simulation of the entire experimental setup including sources and objects in their respective geometries and is the only tool that can accurately predict the anisotropic nature of the columnar scintillator response. Comprehensive validation of the code is necessary to have confidence in the derived results. Once validated, MANTIS can be used to perform system optimizations and accurate reconstructions of data for a variety of applications. It has already been applied to characterize breast tomosynthesis [98] and breast computed tomography (CT) systems [99]. Incorporation of the complete, anisotropic scintillator response has the potential to substantially improve system design and reconstruction techniques.

Previous validation work on this and other detector models has focused on reproducing summary measures of the scintillator performance (*i.e.*, MTF, Swank factor) [92, 93, 95, 98, 100]. In this paper, we approach the validation of the MANTIS package from the perspective of comparing the complete PRFs of the system, while

12

maintaining the information (Swank) factor I and the light output consistent with previously published data. Typically, experimental measures of detector PRFs are performed using edge or slit devices, which can not completely reproduce angular variations in the true PRFs [89]. Here, we use a pinhole-based experimental setup to perform a complete measurement of the PRFs of four different CsI:Tl screens at four incidence angles (0, 15, 30, and 45 degrees) and two x-ray spectra (40 and 70 kVp). In addition, simulated PRFs, that incorporate the detailed experimental setup parameters and CsI:Tl structural information, are produced by MANTIS for each of these screens. A quantitative comparison of the experimental and analogous simulation results is then performed. Note that while the pinhole-based measurements (using a 30 μm diameter pinhole) provide an approximation to the true PRF, since the true PRF requires an infinitesimal incidence point, the simulated data uses the same system setup and therefore also produces an analogous response.

Section 2.2 provides a description of the experimental setup and MANTIS code. The results are presented in Section 2.3 and a discussion is given in Section 2.4. Finally, conclusions are given in Section 2.5.

2.2   Materials and methods

Validation of columnar CsI detector response as simulated by MANTIS was performed by experimentally measuring both relative light output and PRF shape using two different experimental setups. Simulations mimicking those experimental setups as closely as possible were then performed with MANTIS and the results were

compared. In the following subsections we first describe the experimental setups then the corresponding MANTIS simulations, and the FOM used for evaluating the data.

2.2.1 Experiments

We have designed a custom imaging system that allows us to capture high-resolution images of screen output with the additional benefit of having an open faceplate where different screens can easily be mounted. The optical detector setup consists of a high-resolution CCD camera with a 1-to-1 fiber optic faceplate (FOP) that allows measurements on different screens by providing an interface between the detector inside of the thermoelectrically cooled vacuum dewar and the outside environment. The CCD is a Quantix 6303 Photometrics 3072×2048 imaging array with 9×9 μm-pixels. A standard Quantix 6303 camera was modified with a 4.5 cm length 1-to-1 fiber optic faceplate, with 4.5 μm fibers, bonded to the CCD chip on one side, and leaving the other side accessible (outside the vacuum) so that scintillator screens can be positioned and measured (see Figure 2.1).

Individual scintillator screens are held in pressure contact with the FOP by a piece of dense foam inserted between the 0.635 mm thick beryllium window cap and the screen. The use of optical index-matching fluid was investigated to improve contact between the screen and FOP (data not shown), but did not improve the image quality. The indices of refraction were 1.48 for the FOP (Incom, Inc., Charlton, MA) and 1.55 for the optical index-matching fluid (NYE optical fluid OCF-455,
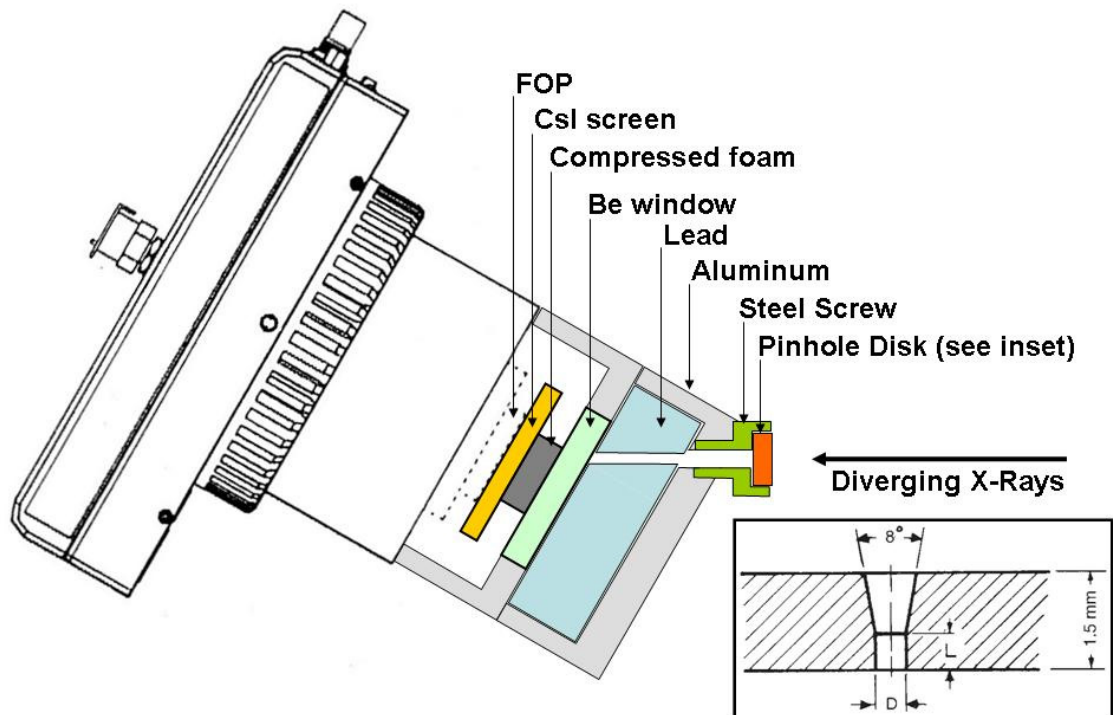
Figure 2.1: Schematic of CCD setup with a 30 degree pinhole holder (not to scale). Diverging x-rays enter from the right. The pinhole is mounted in a caphead screw and positioned in an aluminum holder at the desired angular orientation. lead lining within the aluminum holder provides shielding from background signal and has a hole oriented to allow the primary signal through. The signal then passes through a Be window and compressed foam before impacting the screen and producing the optical signal that travels down the FOP to the optical detector. A cross-sectional view (not to scale) of the pinhole disk is shown in the inset [101]. The manufacturer specifies L=75 μm$\pm$10 μm and D=30 μm$\pm$5 μm for the 30 μm pinhole. Note that, when drawn to scale, the size of the straight edged portion of the pinhole is much smaller than the angled opening.

NYE Lubricants, Inc., Fairhaven, MA).

2.2.1.1 Relative light output

For the light output experiments, four different screens (Screens 1-4) were investigated (see Section 2.2.1.3 for more detail on the screens). Two screens were placed directly against the FOP of the CCD camera, side-by-side, at the same time and a set of 11 exposures was taken with the x-ray tube at 70 kVp (see Section 2.2.1.4 for more details about the x-ray source) and an exposure of 50 mA and 100 ms. One of the screens was always Screen 1, so that the light output relative to Screen 1 could be measured. The light output was then calculated, on the median of the 11 exposures, as the ratio of the average of values within a circular region-of-interest (ROI) on the screen area.

2.2.1.2 Point response function

For the PRF experiments, an additional aluminum cap with lead shielding was bolted onto the beryllium window cap to hold a pinhole (see Section 2.2.1.5 for details about the pinhole) as close to the screen as possible. A total of four aluminum caps were manufactured, each holding the pinhole at a different, fixed angle (0, 15, 30, and 45 degrees) with respect to the screen. Figure 2.1 shows a schematic of the 30° pinhole holder in place. These four angles were chosen to cover the range of typical incidence angles seen in mammography, tomosynthesis, and breast CT systems (see Ref. [98]). Additional shielding is provided by a lead sleeve

that fits around the outside of the camera and a lead window near the end of the CCD assembly.

This entire camera/screen/pinhole assembly is bolted to a motorized rotation stage controlled via a LabView program to allow accurate angular alignment with the x-ray source. Alignment at zero degrees is achieved with a laser assembly between the beryllium window cap and the x-ray tube window. A small laser is mounted in a circular cap that bolts onto the window cap and a circular mirror is secured in front of the x-ray tube window with two plastic pressure tabs. Positions of the x-ray tube and detector are adjusted until the reflected laser beam coincides with the original laser beam location. Once this condition is achieved all stages controlling the x-ray tube and detection position are locked in place except for the rotational stage that controls the angle of the CCD camera. For all measurements, the distance from the source to the pinhole was 130.0 cm. The distance from the screen to the pinhole varied in the range 17.78-25.4 mm, depending on what angle was being measured and the thickness of the measured screen.

PRFs were measured on all four screens with 40 and 70 kVp spectra for each of the four incidence angles (0, 15, 30, and 45 degrees). Eleven images were acquired for each of the experimental conditions so that error bars could be estimated from the sample variance. Pixels in the individual experimental images that were more than 5 standard deviations from the median over all 11 images were replaced with the median value for that spatial pixel location before further analysis.

2.2.1.3 Screens

A total of four different columnar CsI scintillator screens (provided by Radiation Monitoring Devices, Inc., Watertown, MA) were measured. Their manufacturer's specifications are given in Table 2.1. In order to characterize screen morphology, cross-sectional views were imaged with a scanning electron microscope (SEM, model ISI SS40, now Topcon, Tokyo)[2]. This allowed measurements of not only the thickness of the CsI layer, but also of the approximate diameter and angle of the columns relative to the substrate. Note that, while SEM measurements provide a means of probing the internal structure of the screens, they do have several important shortcomings. First, an SEM can never be acquired of exactly the same position that is used to acquire an image. Second, only a very small number of SEM measurements can be performed on a single screen, resulting in a poor sampling of the crystal structure. Finally, the act of acquiring the SEM image for a cross-sectional view can modify the structure of the crystal itself. All of these shortcoming arise from the fact that acquisition of an SEM image for a cross-sectional view requires the screen to be physically broken, and is, therefore, inherently destructive. Figure 2.2 shows the SEM measurements of each of the screens. From this figure we can see how the tilt angles and layer thicknesses vary between the different screens. In addition, we can see the transition from columnar to amorphous CsI close to the substrate. This figure demonstrates the variety of structures seen in the different screens as well as allows the reader to evaluate the ability of the simulation code to

---

[2]by Stuart Miller
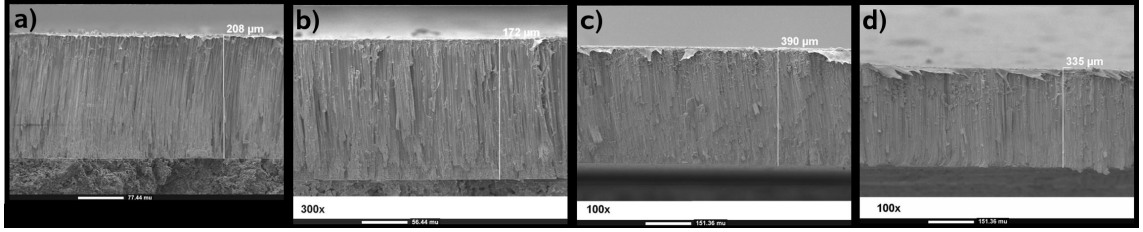
Figure 2.2: SEM measurements of all screens. The physical size of the white scale bar at the bottom of each SEM as well as the magnification are given following the screen number. a) Screen 1 (77.4 μm, 200x), b) Screen 2 (56.44 μm, 300x), c) Screen 3 (151.36 μm, 100x), and d) Screen 4 (151.36 μm, 100x)

reproduce these complicated structures.

The measured screens cover a range of different properties including reflective and absorptive substrates, thin and thick columnar scintillator layers, a variety of different layer structures, and varying columnar tilt angles. An estimate of the columnar tilt angle of each of the screens was performed by using a graphics program to measure the angle of a line drawn over the SEM following a column judged to be representative of the area imaged by the SEM. The error in estimation of this tilt angle was approximately ± 0.5 degrees. In Section 2.4.5 we discuss the importance of accurately determining this parameter and find that an error of as large as ± 6 degrees does not significantly affect the results.

For one of the screens (Screen 3), a second SEM measurement was taken at a different orientation (data not shown), approximately perpendicular to the first orientation, to provide a more accurate characterization of the CsI structure. For the two corners of Screen 3, the measured columnar tilt angles were 2.5 and 6.0 degrees. The combination of these two tilt angles gave the final tilt angle of 6.5 degrees as indicated in Table 2.1. For Screen 2, the range in columnar tilt angle is

Table 2.1: Manufacturer specifications and model parameters of the four measured CsI scintillator screens.

Screen	Manufacturer	Part No.[a]	CsI Thickness [microns][b]	Screen Dims [mm]	Substrate	Estimated Column Tilt [deg][c]	Simulated Layers
1	RMD Inc.[d]	B31-3	208	50x50x1	graphite	6.0	4 μm organic polymer 166.4 μm columnar CsI 41.6 μm homogeneous CsI
2	RMD Inc.	B39-2	170	50x50x1	graphite +Al	2.6-4[e]	4 μm organic polymer 136.0 μm columnar CsI 34.0 μm homogeneous CsI
3	RMD Inc.	B40-3	450	50x50x1	graphite +Al	6.5	4 μm organic polymer 360.0 μm columnar CsI 90.0 μm homogeneous CsI
4	RMD Inc.	B40-7	380	50x50x1	graphite	2.0	4 μm organic polymer 304.0 μm columnar CsI 76.0 μm homogeneous CsI

[a]Manufacturer's Part Number
[b]Determined from SEM measurements for Screen 1 and by optical microscopy for Screens 2-4
[c]Estimated from SEM measurements.
[d]Radiation Monitoring Devices, Inc., Watertown, MA, http://www.rmdinc.com/products/p005.html
[e]A constant value of 3.3 degrees was used in the simulations.

due to the fact that the tilt angle varied over the area imaged in the SEM. Overall, the measured tilt angles of the screens varied from between approximately 2.0 and 6.5 degrees. In all but one of the screens (Screen 3) the magnitude of the tilt angle was only measured in one direction and is therefore a lower limit to the true tilt angle at that location. Additional uncertainty arises from the fact that the columnar tilt angle may vary over the screen surface. See Section 2.4.1 for further discussion of errors associated with quantification of the SEM structure.

2.2.1.4   X-ray source

The x-ray source is a Varian B180 (Varian Corp., Salt Lake City, UT) x-ray tube with a tungsten anode, a 0.3 mm focal spot, 1.0 mm Al internal filtration, and no additional filtration. For the current measurements, data were taken with peak energies of 40 kVp and 70 kVp.

2.2.1.5   Pinhole

The pinhole assembly consists of a small, 90:10 Gold-Platinum alloy disk with a pinhole aperture machined through the center of the disk face and mounted in the head of a cap screw (Fluke Biomedical X-Ray Pinhole Assembly #07-613, Everett, WA). The manufacturer's specifications are shown in the inset of Figure 2.1 (L=75±10 μm, D=30±5 μm) [101].

2.2.2   Simulations

The simulations were performed using MANTIS[3], a tool for modeling x-ray imaging systems with CsI:Tl columnar scintillator screens. MANTIS simulates the transport of x-ray photons, electrons, and optical photons within the same geometric model[102, 103]. The code MANTIS, which is publicly available online[4], incorporates the PENELOPE [104] physics for x ray and electron interaction physics models, along with the optical transport models and geometry descriptors. For validation of previous versions of the code, we have focused on the statistics of the screen optical signal using Swank factor measurements[100]. Results of that validation show that the predictions of MANTIS are well within the uncertainties of experimental measurements.

In this paper, we have incorporated the detailed geometrical structure of each specific scintillator screen (see Table 2.1). Additional parameters, such as material and surface optical properties and columnar packing density, remain unchanged from previous simulations and are listed in Table 2.2. Details we can model include scintillator thickness, additional top and bottom layers that are present in the overall detector such as the substrate and protective layers, and uniform tilt angle and direction of the CsI:Tl columns. For this study, each individual PRF was produced with 5×10^5 histories and required approximately 14 minutes of CPU time on a 768-core Linux cluster with MANTIS version 2.0. This number of histories produced PRFs

---

[3]by Aldo Badano

[4]A current version of the code, tutorials, and examples are available from http://code.google.com/p/mantismc.

with low enough uncertainties to allow for precise comparisons of the figures-of-merit (FOMs) for the different cases compared in this study.

2.2.2.1   Relative light output

Relative light output values were calculated by counting the number of detected optical photons from PRF simulations for 0 degrees and 70 kVp and dividing by the value for Screen 1 with a substrate reflectivity of 10%. Reflectivities of 10%, 17%, and 40% were investigated for the graphite substrates and 35%, 80%, and 90% for the aluminum-coated substrates. A range of reflectivities was investigated in simulation since it was not possible to directly measure the substrate reflectivities of the actual screens.

2.2.2.2   Point response function

Here, the incoming beam was modeled a parallel beam from a circular source of 100 μm diameter. The x-ray spectra used in the simulations were calculated using IPEM Report 78 [105] for 40 kVp and 70 kVp spectra with 1.0 mm Al filtration. The spectra are shown in Figure 2.3. The mean photon energy (MPE) and half-value layer (HVL) for the 40 kVp spectrum are 25.6 keV and 0.8926 mm Al respectively. For the 70 kVp spectrum, the MPE and HVL are 36.5 keV and 1.593 mm Al. The pinhole disk and Be window were both simulated using the exact material composition and geometrical measurements as provided by the manufacturers.

Table 2.2: Simulation parameters of the MANTIS model

Column diameter	10.2 μm
Packing density	85% (approx)
Photodiode thickness	10 μm
FOP	slab of glass (material #171 in PENELOPE)
Column surface roughness parameter a	0.2

Optical properties	n	$\mu_{absorption}$ (cm^{-1})	$\mu_{scatter}$ (cm^{-1})
Scintillator	1.8	1.0	1.0
Ni Gas between columns	1.0	0.0	0.0
Photodiode	1.7	0.1	10.0

Figure 2.3: Spectra used in MANTIS simulations of the experimental PRFs: 40 kVp (solid line) and 70 kVp (dashed line). Both spectra include 1.0 mm Al filtration.

Measurements of the columnar tilt angle and layer thicknesses for each individual screen, as described in Section 2.2.1.3, were incorporated in the geometric model implemented in MANTIS. In the current version of the code (version 2), the columnar shape and tilt angle are required to be constant for the entire array of columns across the screen. From inspection of Figures 2.2 and 2.4 we can see that this is an oversimplification since both the columnar shape and tilt angle can change in a complicated manner over the screen surface. We are currently working on more sophisticated geometrical models for future versions of the code. Figure 2.4 shows a side-by-side comparison of the SEM measurement of Screen 1 and the corresponding model structure used in MANTIS. All of the measured screens were modeled with 4 different layers; a 4 μm planar protective layer of organic polymer, a variable thickness layer (depending on the SEM-derived thickness of the individual screens) of columnar CsI, a layer of homogeneous CsI crystal with 20% the thickness of the total CsI layer, and a 1-mm-thick substrate of either graphite or aluminum-coated graphite depending on the individual screen. The CsI columns in the columnar layer had a uniform diameter and tilt angle over the entire screen. The tilt angle of the columns was along the same direction as the oblique angle of x-ray incidence. The reflectivities of the graphite and aluminum-coated graphite substrates were assumed to be 10% and 90% respectively in MANTIS.

The photodiode layer was placed immediately following the screens. This was then followed by as a solid glass slab (PENELOPE material 171) to model the FOP. We chose to model the FOP and photodiode layer in this manner to
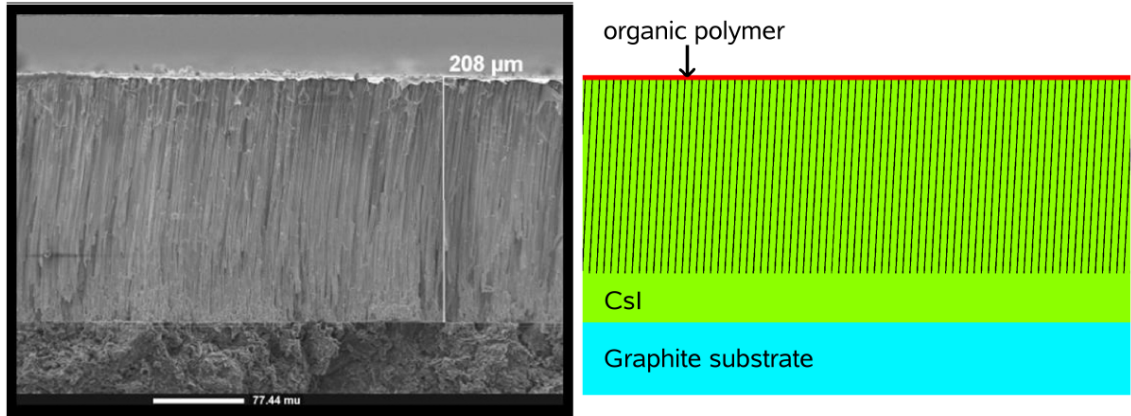
Figure 2.4: (left) SEM of Screen 1 (white scale bar = 77.4 μm, magnification=200x) (right) Schematic of MANTIS model of the same screen (to scale). The thin layer at the top of the image represents the organic polymer. The organic polymer layer is followed by the columnar zone, where light gray indicates CsI and dark grey is the inter-columnar space. The next layer is the homogeneous CsI and, finally, the bottom layer is the substrate.

capture the scatter associated with the FOP. We are currently unable to simulate the transmission properties of the FOP itself. Although in reality, the photodiode layer is after the FOP, we do not expect this inconsistency to significantly affect the results, as discussed later in Section 2.4.4.

Using the above-mentioned parameters, PRFs were simulated on all four screens with 40 and 70 kVp spectra for each of the four incidence angles (0, 15, 30, and 45 degrees). Eleven images were simulated for each of the cases to allow for estimation of error bars.

2.2.3   Figure of merit

A quantitative comparison of the experimental and simulated PRFs was performed by computing a FOM for each of the eleven pairs of experimental and simulated images for each different screen/spectrum/incidence angle combination. The

27

mean and standard deviation of the eleven independent FOMs were taken as estimates of the FOM and its error. The FOM was calculated as

$$FOM = \sqrt{\frac{1}{N_{ROI}} \sum_{i=1}^{N_{ROI}} \Delta_i^2}, \tag{2.1}$$

where N_{ROI} is the number of pixels in the ROI and Δ is the normalized difference. The normalized difference is defined as

$$\Delta_i = 1 - \frac{s_i / \sum_i s_i}{(e_i - b) / \sum_i (e_i - b)}, \tag{2.2}$$

where b is a background value calculated by summing the values in a corner of the image where there is no signal and s_i and e_i are elements of the vectors $\mathbf{s}$ and $\mathbf{e}$ that contain all the simulated and experimental PRF values, respectively, within the selected ROI. The vectors $\mathbf{s}$ and $\mathbf{e}$ are defined by

$$\mathbf{s} = \{\mathbf{PRF}^{sim}; PRF_j^{exp} \geq 50\,\sigma \text{ and } PRF_j^{sim} > 0, j \in [1, N_{PRF}]\} \tag{2.3}$$

and

$$\mathbf{e} = \{\mathbf{PRF}^{exp}; PRF_j^{exp} \geq 50\,\sigma \text{ and } PRF_j^{sim} > 0, j \in [1, N_{PRF}]\}, \tag{2.4}$$

respectively, where $\mathbf{PRF}^{sim}$ is the simulated PRF, $\mathbf{PRF}^{exp}$ is the experimental PRF, PRF_j^{exp} is an element of the experimental PRF image, PRF_j^{sim} is an element of the simulated PRF image, N_{PRF} is the number of pixels in the PRFs (the simulated and experimental PRFs have the same number of pixels), and σ is the noise in the

experimental image calculated as the standard deviation of the lower left corner of the image. Therefore, the ROI is identical for both the simulated and experimental images and consists of those pixels with a signal-to-noise ratio (SNR), PRF_j^{exp}/σ, of greater than or equal to 50 in the experimental data and a non-zero value in the simulated data. This ROI was chosen so that pixels in the peak and tails of the ROI contributed equally to the FOM. Note that the ROI is not square or circular, rather it only includes pixels that satisfy the SNR condition. The extent of the ROI is indicated in Figure 2.5. Figure 2.9 in Section 2.3.2 gives an indication of the ROI size since all pixels outside of the ROI are set to zero in these images. The number of pixels in the ROI ranged from 206 to 736 pixels (equivalent to 16686 to 59616 μm^2) over all PRFs investigated.

To ensure that the two PRFs were correctly aligned before calculation of the FOM, the maximum of the two-dimensional (2D) cross-correlation function was used to determine the optimal relative shifts and rotations of the two images prior to calculation of the FOM. The resolution of the cross-correlation algorithm was one pixel (9 μm) for x and y shifts and one degree for rotations.

Finally, to provide a benchmark to put the FOM values in context, the same FOM was also calculated using a symmetric 2D Gaussian, fit to the zero-angle experimental data, as the simulated data. The Gaussian fit was performed using a modified version of the program *gauss2dfit* in the software package IDL (ITT Visual Information Solutions, Boulder, CO) that forced the widths of the 2D Gaussian in the x and y directions to be equal.
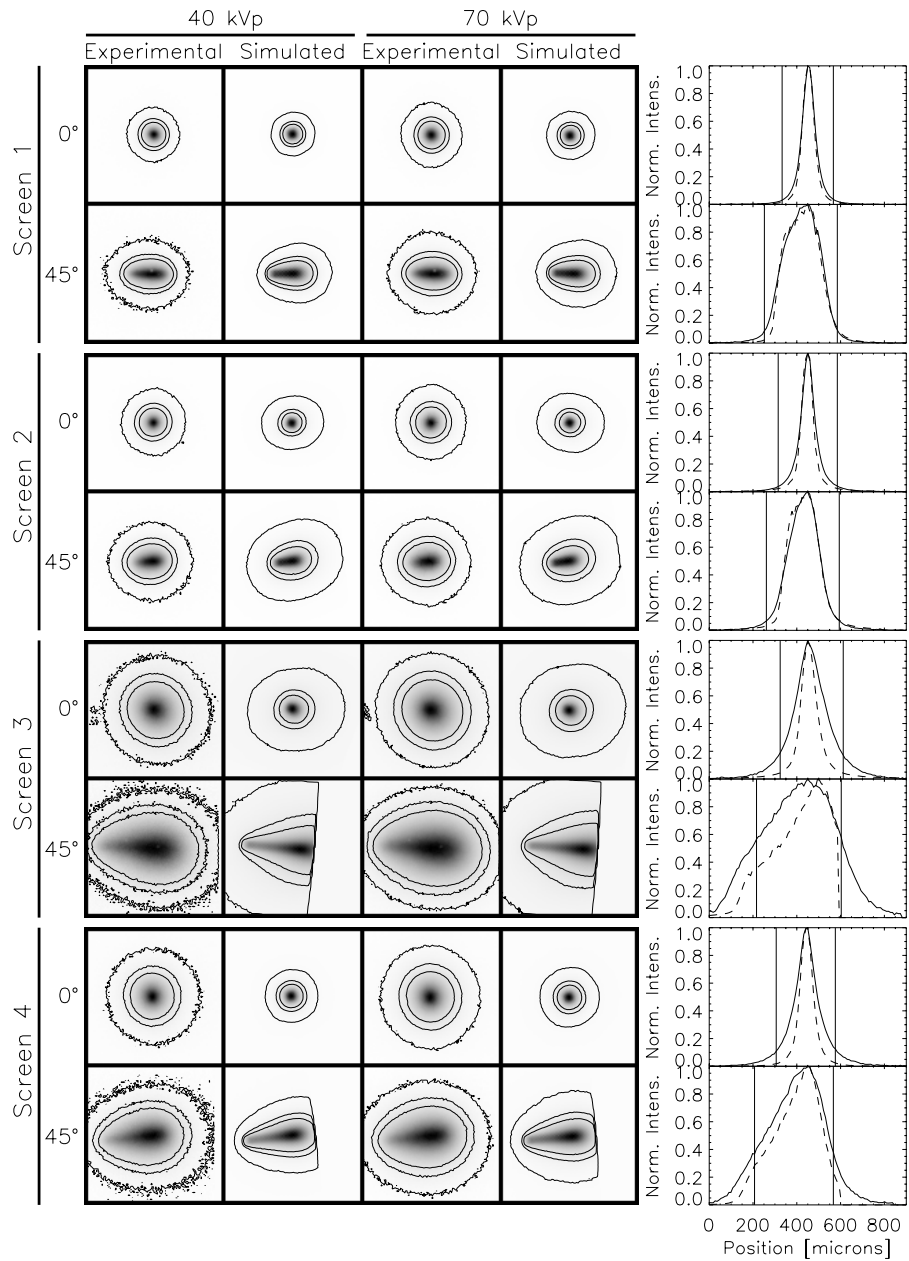
Figure 2.5: Experimental and Simulated PRFs for Screens 1-4. (1st column) 40 kVp, Experimental (2nd column) 40 kVp, Simulations from MANTIS (3rd column) 70 kVp, Experimental (4th column) 70 kVp, Simulations from MANTIS (5th column) 40 kVp, Horizontal cuts through the center of the PRFs, experimental data are shown with a solid line and MANTIS results are shown as a dashed line. The solid vertical lines indicate the size of the ROI. The different screens are labeled as well as the incidence angles. Only incidence angles of 0 and 45 degrees are shown. Contour lines shown on the plots are for levels of 0.01, 0.05, 0.1 (the maximum is always 1). All PRFs are 101×101 pixels with 9 μm/pixel.

2.3 Results

2.3.1 Relative light output

The experimental light output values were compared with light output values derived from MANTIS simulations with a variety of substrate reflectivities. The substrate reflectivities used in MANTIS for the PRF comparisons were 10% for the graphite substrates and 90% for the aluminum-coated substrates. We have investigated additional reflectivities (17% and 40% for graphite and 35% and 80% for aluminum) to observe their effect on the light output values. The measured and simulated relative light output values for graphite and aluminum-coated substrates are shown in Table 2.3. For the graphite substrates, we only have a single independent measurement of light output (for Screen 4). The results seem to indicate that a very large reflectivity (much greater than 40%) is necessary to match the experimental results. For the aluminum-coated substrates, we have two independent measurements of light output (Screens 2 and 3) and we see that no single reflectivity value can reproduce the experimental results of both of the screens. Results from Screen 2 seem to indicate an aluminum reflectivity of between 80% and 90%, while Screen 3 implies a reflectivity of much greater than 90%, however these results are less discordant since the simulated light output values at 80% and 90% are the same to within two error bars. This inconsistency is probably a result of one of two or both effects; the fact that reflectivity is only one of numerous parameters in MANTIS that affects the light output of a screen and the fact that different screens from different manufacturing batches can have highly variable light outputs depending on slight

differences in the manufacturing process that are not easily controlled or quantified. See Section 2.4.2 for a discussion of variability of screen performance with manufacturing process. In future studies it will be important to provide independent measurements of substrate reflectivity to reduce the number of variables needed to validate light output. However, these measurements must be carefully controlled since substrate reflectivity can vary depending on handling conditions and substrate production methods. For all other MANTIS-generated PRFs presented in this paper, we have used substrate reflectivities of 10% for graphite and 90% for aluminum-coated graphite because those values were used in previous validation efforts and have been crucial in matching Swank factors (see Ref. [98]). In the future, we plan to perform reflectivity measurements on the individual substrates themselves during the screen production process, so that these values can be included in MANTIS and the number of unknown parameters in the simulations can be reduced.

2.3.2 Point response functions

Figure 2.5 shows the experimental and simulated PRFs for the screens in Table 2.1 at 40 and 70 kVp x-ray source energies and 0 and 45 degree incidence angles. Here, the eleven individual experimental and simulated results have been combined to produce a single PRF for each spectrum/incidence angle combination. The PRFs have all been normalized by their maximum value and contours at 0.01, 0.05, and 0.1 times the maximum value are shown. Also shown are plots of horizontal cuts through the experimental and simulated PRFs for 40 kVp. The experimental

Table 2.3: Measured and simulated relative screen output for screens with graphite and aluminum coated substrates. All values are normalized to Screen 1 at 10% reflectivity.

Graphite Substrates

Screen No.	Measured Light Output	Simulated Light Output		
		Refl: 10	Refl: 17	Refl: 40
1	1.000±0.000	1.000±0.021	1.011±0.054	1.149±0.051
4	1.469±0.042	1.148±0.020	1.183±0.049	1.300±0.055

aluminum-Coated Substrates

Screen No.	Measured Light Output	Simulated Light Output		
		Refl: 35	Refl: 80	Refl: 90
2	1.456±0.043	1.046±0.060	1.393±0.068	1.504±0.031
3	1.650±0.050	1.214±0.050	1.465±0.047	1.522±0.027

data is shown with a solid line and the simulated data is shown with a dashed line. The sharp cutoffs seen in the simulated data of Screens 3 and 4 are because the simulations were not run past this spatial location. The most noticeable quality of the PRFs is their highly non-Gaussian shape at large incidence angles. This tear-drop shape, seen especially well in the thick screens, is due to the increasing spread of the secondary photons produced by x-rays deposited at shallow depths in the CsI crystal. There is also a large variation evident between the individual screens. These large differences make it clear that one PRF model does not fit all CsI scintillator screens and that each screen must be individually modeled according to its specific structure. In particular, we can see that MANTIS clearly does a better job of reproducing experimental data for the thinner screens (Screens 1 and 2).

Figures 2.6-2.9 show the results of quantitative comparisons between experimental and simulated data. Figure 2.6 shows a plot of all the FOMs for all the screens, energies, and angles investigated. We see that the FOMs comparing experimental data with MANTIS simulations are between about 0.1929 and 0.4775 for all cases. There does not seem to be a significant difference in the FOM values with energy. For the thicker screens (Screens 3 and 4), MANTIS tends to reproduce PRFs with larger incidence angles better than those with smaller incidence angles. In this case, the cause may be due to the principal determinant of the PRF shape. At large incidence angles, the PRF shape is largely determined by the geometry of the system (the angle of the x ray entering the crystal), whereas at small incidence angles the principal determinant of the PRF shape is the optical transport. Since geometry is much easier to model than optical transport, PRFs at large angles may be easier to

34
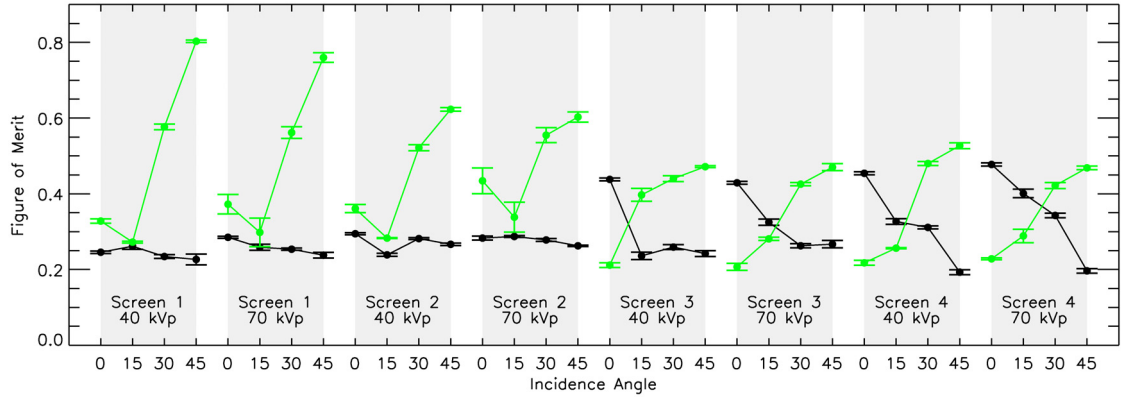
Figure 2.6: FOMs for all screens, energies, and incidence angles. Black indicates the results from the comparison of experimental data with MANTIS-generated PRFs and green indicates the results from the comparison with a 2D symmetric Gaussian fit to the zero-angle experimental data. The values displayed are means of FOMs calculated from 11 independent experimental and simulated images, while the error bars represent the standard deviation of those 11 different FOMs.

predict. For the same substrate type and energy, MANTIS tends to perform better for thin screens than for thick screens at small incidence angles.

For the comparison with Gaussian fits, we find that the FOM ranges between about 0.2068 and 0.8029. It is notable that the FOM for the Gaussian fits to the experimental data are, in general, worse than the MANTIS simulated PRFs. The exception is that the symmetric Gaussian fit tends to match the experimental data better for the thicker screens than for the thinner screens at small incidence angles, which suggests that as the screens get thicker their response becomes more Gaussian. Note that, for the thicker screens, MANTIS still outperforms the Gaussian fit for larger incidence angles. It's interesting to note that, for the thinner screens, even at an incidence angle of zero degrees, MANTIS outperforms the Gaussian fit. Figure 2.7 shows a closer examination of the experimental data, MANTIS simulations results, and Gaussian fits at zero degrees for 40 kVp. Horizontal, one-dimensional cuts

35
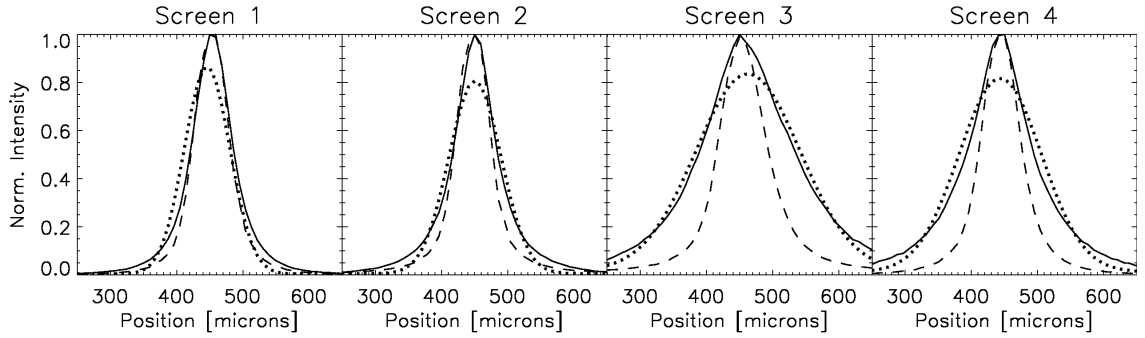
Figure 2.7: Comparison of experimental, MANTIS, and Gaussian fit PRFs at zero degrees for 40 kVp. One-dimensional, horizontal cuts through the center of the PRFs are shown for each screen. The experimental data are shown as a solid line, MANTIS as a dashed line, and the Gaussian fits as a dotted line. We can see in all cases that the Gaussian fit underestimates the peak of the PRF. For the thicker screens (Screens 3 and 4), MANTIS provides a much sharper PRF than the experimental data and, as a result, the FOM calculation indicates a better match to the experimental data for the Gaussian fit than MANTIS.

through the centers of the PRFs are shown for each of the four screens. We can see in all cases that the Gaussian fit underestimates the peak of the experimental data and MANTIS provides a better estimate of the PRF shape. Therefore, the better performance of the Gaussian fit for small incidence angles for the thicker screens seems to be due to the fact that MANTIS is underestimating the width of the PRF.

Figures 2.8-2.9 show a more detailed breakdown of the normalized differences (Δ_i as given in Equation 2.2). In Figure 2.8 the normalized difference is plotted on the y axis and the angle of incidence on the x axis for every screen and energy investigated. The objective of this plot is to show the distribution of normalized difference values that make up the single FOM values. The FOM is calculated by taking the RMS of the normalized difference values. The box plots show the median normalized difference (in the ROI) as the filled circle, the bottom and top of the box are the 1st and 3rd quartile, and the bottom and top error bars show the
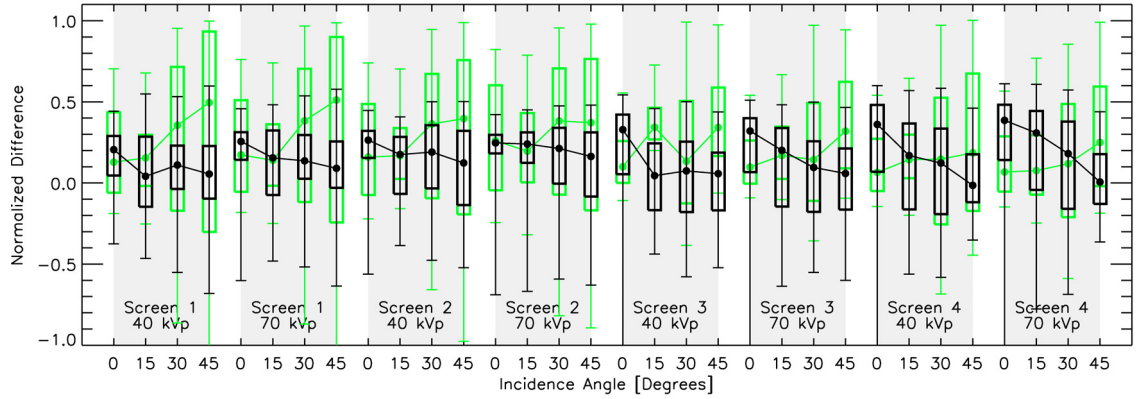
Figure 2.8: The normalized difference of the PRFs is plotted as a function of incidence angle for all screens, energies, and incidence angles. Normalized differences from the comparison with MANTIS are plotted in black, while normalized differences from the 2D Gaussian fit are plotted in green. The box plots show the median normalized difference (in the ROI) as the filled circle, the bottom and top of the box are the 1st and 3rd quartile, and the bottom and top error bars show the minimum and maximum normalized difference.

minimum and maximum normalized difference. Results for the MANTIS comparison are shown in black and for the Gaussian fit are shown in green. A selected set of the corresponding images are displayed in Figure 2.9 that show the spatial distribution and relative magnitude of the normalized differences for each incidence angle investigated. In these plots the normalized difference is shown in the ROI where a normalized difference of zero is mapped to black, negative differences are shown as shades of blue, and positive differences are shown as shades of red. The images are all scaled to the minimum and the maximum of the normalized differences for each particular PRF. Therefore, Figure 2.9 shows the spatial distribution of the normalized differences over the ROI, while Figure 2.8 shows the distribution of the actual numerical normalized difference values. These figures allow a more detailed analysis of the differences between the experimental and MANTIS model data.
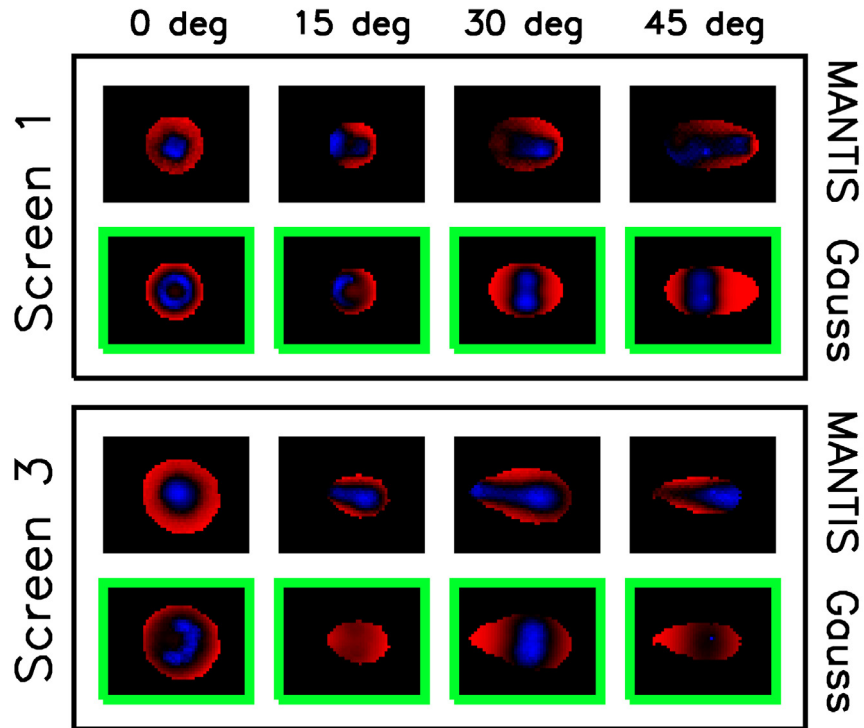
Figure 2.9: Images showing the spatial distribution of the normalized differences for all incidence angles of Screens 1 and 3 with the 40 kVp spectrum. Images from the comparison of experimental data with MANTIS are outlined in black and labeled "MANTIS", while images from the comparison with the 2D Gaussian fit are outlined in a green box and labeled "Gauss". Negative normalized differences are mapped to shades of blue, positive to shades of red, and zero to black. The images are all scaled to have red, blue, and black as corresponding to the most positive, most negative, and zero data values, respectively. As a result, these images simply indicate the spatial location and relative magnitude of differences and not the absolute magnitude of the difference which is indicated in Figure 2.8.

As an example of the type of information conveyed in Figure 2.8, we can compare Screen 1 at 70 kVp and 0 degrees with Screen 3 at 40 kVp and 45 degrees. From Figure 2.6 we can see that the FOMs of the comparison with the Gaussian is larger than the FOMs from the comparison with MANTIS results in both cases. Now, if we examine Figure 2.8 we can see that the reason for the disparity in FOMs of the two cases (Screen 1/70 kVp/0 degrees versus Screen 3/40 kVp/45 degrees) is very different. In the case of Screen 1 (70 kVp/0 degrees), the average normalized differences are very similar and the difference in FOM arises from the fact that the range of normalized difference values is much larger for the Gaussian comparison than for the MANTIS comparison. Conversely, for Screen 3 (40 kVp/45 degrees) the range of the normalized difference values are very similar for the Gaussian and MANTIS comparisons, but the difference in FOMs arises from the fact that the mean normalized difference values are very different. The data in Figures 2.8 and 2.9 also demonstrate that the main reason for the differences between the experimental and MANTIS PRFs is that MANTIS tends to produce PRFs that are too sharp compared to the experimental data. This can be seen particularly well in Figure 2.9 in the images with the black outline (labeled "MANTIS") since the central portion of the difference image tends to be blue (or negative) and the outer region tends to be red (or positive). In fact, this effect is also easily visualized in the individual PRF images in Figure 2.5. This trend is evident for all screens, energies, and incidence angles.

2.4 Discussion

Examination of the experimental and MANTIS-generated PRFs shows that MANTIS provides a good fit to the experimental data for all energies, incidence angles, and screens measured. The match between experimental and MANTIS PRFs is especially good for the thinner screens. However, we do see that a 2D Gaussian fit to the zero incidence angle data outperforms MANTIS for small incidence angles for the thicker screens. In addition, MANTIS consistently predicts sharper PRFs than those measured experimentally.

Another point that should be made is that, for this study, the parameters used in MANTIS were taken from previous studies where pulse-height spectra had been validated. The only parameters that were modified were related to geometry of the system components. In effect, this approach answers the question of how well MANTIS can predict detector performance with only basic geometrical information about the screen and no additional modification of the other model parameters. We anticipate that MANTIS can match experimental data more closely by optimizing various parameters of the code (e.g., reflectivities, bulk absorption, amorphous layer fraction), however, unless these parameters are obtained through physical measurements, this would not indicate the ability of the code to predict performance. Therefore, the results presented in this study represent a conservative estimate of accuracy for the estimation of the PRF of CsI screens.

To our knowledge, only two other models have been validated against experimental data from columnar CsI scintillators [97, 106]. In the model produced by

Blakesley and Speller [97], zero incidence angle simulation results were compared against experimental data from two systems with different columnar CsI screens. The validation was performed by overplotting the experimental MTF with simulated results, no quantitative FOM was used. For one of these systems, the screen had an unspecified thickness, so the model was adjusted to provide the best fit to the experimental data. For the other system, simulations were compared with two CsI screens that had the same thickness, but were deposited on different substrates. Their model predicted a MTF that was in between the experimental measurements of the two screens. The authors emphasize the inability of the model to include all the details of the screen properties and the fact that properties of screens with the same thickness and scintillator material can vary widely due to a variety of factors. In the first system they discuss, the experimental data itself was used to determine the model parameters and is, therefore, not a representation of the predictive abilities of the model. In the second case, the model parameters were determined independent of the experimental data, but the model was not detailed enough to distinguish between the two types of screens investigated. The authors acknowledge that there are many different parameters not included in the model that can affect screen performance. In our validation efforts, we have avoided using the experimental data to determine any model parameters so that the validation addresses the predictive abilities of the model. In addition, we have attempted to include more parameters that may affect screen performance, such as the detailed structure of the CsI crystal. However, our validation efforts are still subject to a number of uncertainties as will be discussed in the following subsections.

Mainprize *et al.*[106] developed an analytical model for the one-dimensional MTF of a scintillator as a function of angle of incidence of an incoming x-ray beam. This was compared with experimental MTFs measured on a structured CsI flat panel detector at four different incidence angles and two different x-ray spectra after dividing by the zero-angle MTF. In this case, since the thickness of the CsI was not known, it was determined by a fit with the experimental data itself. Again, the model was validated by qualitatively comparing the MTFs of the simulated and experimental data. In this study, the experimental data was also used to determine model parameters since the thickness of the CsI was not known. Therefore, as in the Blakesley and Speller [97] study, the validation is not of the predictive ability of the model. In addition, the model was only meant to simulate the effects of incidence angle and did not include optical transfer properties of the crystal.

Our study is a validation of the predictive abilities of the MANTIS software since the experimental results were not used to determine model parameters. In addition, MANTIS includes effects of both optical transfer as well as incidence angle and details of the columnar structure of the CsI crystal. In order to fully characterize the asymmetric detector blur that can be generated with MANTIS, we have chosen to validate the model against 2D experimental PRFs, which are not subject to the limitations of MTF analysis. In addition, we have developed a quantitative FOM to facilitate comparison of different screens and imaging systems. Examination of this FOM across the four investigated screens has shown that although MANTIS provides a good fit to the experimental data, there still exist some uncertainties that cause MANTIS to predict sharper PRFs than those seen experimentally. In the

42

following sections we discuss possible sources of error that may contribute to the differences seen in Section 2.3 between the experimental data and MANTIS model results. Details of the scintillator screen layers and their geometry, variation in screen properties due to the manufacturing process, geometry of the x-ray source and pinhole, blur due to the FOP, and orientation between the columnar tilt angle and the incoming x-ray beam are all considered.

2.4.1 Accurate knowledge of screen details

The ability of MANTIS to incorporate detailed structure of the CsI scintillator screens requires that the true structure be accurately quantified. For this purpose, SEM measurements were taken and analyzed. However, there are limitations in both the ability of MANTIS to incorporate high levels of detail, and for the SEMs to accurately quantify the CsI structure. In the case of MANTIS, the CsI crystal must be cleanly divided into two regions, a homogeneous region (in contact with the substrate) and a columnar region that extends beyond that. In reality there is a smooth transition between the solid and columnar structures in the CsI crystal. MANTIS also requires that the columns all have the same circular diameter and tilt angle and that all layers have a uniform planar thickness. However, inspection of the SEM images clearly shows that all of these characteristics are, at some level, inaccurate. In reality, the CsI columns have irregular, non-circular cross-sections that vary along the depth of the CsI layer, the thicknesses of layers can vary over the crystal width, some deposited layers form a non-planar surface that dips down into

the layers below, and tilt angles of the columns are non-uniform even over the small field of view of the SEM images. While these inaccuracies do exist, the reasonable approximation employed by MANTIS should allow for representative results.

With respect to the size and shape of the columnar bases, our previous work has shown that column base shape does not affect medium or long range blur ($>$ 10μm)[107] for a model that does not include columnar tilt. However, the effect of intra-columnar spacing, presence of cracks and dislocations in the columns, and presence of contact between the columns remains to be investigated.

We are currently working to improve the ability of MANTIS to simulate random columnar tilt and shape by developing a geometry definition that generates the columnar structure on-the-fly as it follows the interaction sites of x rays and electrons. It is possible that the artificial regularity of the Monte Carlo geometry used in this work is contributing to a bias in the resulting PRF images. One way that we have approached this limitation is by introducing variations in the columnar walls to represent the variability in the columnar shape seen in the SEMs. This is implemented with a roughness algorithm that was described in our previous papers [90, 108]. However, the introduction of this variation in the geometry is not based at the moment on any physical characterization performed on actual screens. To be consistent with results presented in previous papers, we have used the same amount of variability (a=0.2, where a is a user-adjustable parameter that defines the amount of mixing of the surface normal with an isotropic vector) as defined in Ref. [90].

The SEM measurements themselves have some additional sources of error that affect the thickness calculations of different layers. The approximate error in thick-

ness estimation from the SEM measurements is $\pm 10\%$. For most screens (Screens 2, 3, and 4), optical microscopy images were also taken (on a Leitz Laborlux 12 HL microscope) to provide more accurate thickness measurements (errors of approximately $\pm 3\%$). Calculation of tilt angles should be unaffected by these thickness inaccuracies since there is no measurable distortion in the images. Quantification of the tilt angles was, however, affected by the limited sampling of the CsI scintillator screens. For all screens, one or two corners were imaged in a single field to determine tilt angles and thicknesses. A limited number of samples were used to produce measurements from the same screens used to collect PRF data. Since the tilt angles are not necessarily aligned with the imaged plane, the tilt angles calculated from a single corner represent a minimum tilt angle. Tilt angles calculated from a second corner (approximately perpendicular to the first imaging plane) provided a more accurate quantification of the true tilt angle. Of course, these calculations assume that the tilt angle is uniform over the screen face, which is probably not true in reality.

The reflectivity of the screen substrate is also a potential source of error. In this paper, we chose reflectivities of 10% for graphite substrates and 90% for aluminum-coated substrates. However, experimental measurements of substrate reflectivity should provide more accurate estimates of this parameter and, in the future, we hope to arrange such measurements for incorporation into the simulations.

While these uncertainties mean that MANTIS can not exactly reproduce all of the complex details of the SEM structure, the level of complexity modeled in MANTIS represents the most complete modeling of CsI scintillator screens to date

and should provide representative results that properly simulate trends in the PRF structure.

2.4.2 Variation in screen properties

Variation in screen properties due to the manufacturing process may be a significant source of error when comparing experimental data with simulations. To quantify this variation, the MTF was measured for a total of 11 screens produced during four different deposition runs (2-3 screens per deposition run) with an average CsI thickness of 240 μm. All screens were deposited on a graphite substrate. The range of MTF values at 5.0 lp/mm for each of the four deposition runs were 0.130-0.134, 0.273-0.327, 0.228-0.321, and 0.316-0.337. Similarly, at 8.1 lp/mm the MTF values were 0.035-0.038, 0.109-0.148, 0.083-0.156, and 0.146-0.164. There are large variations both within a single deposition as well as between the different deposition runs. The factors responsible for these types of differences may not be included in the MANTIS models and, as a result, may be responsible for some of the discrepancies seen.

2.4.3 Accurate x-ray source and pinhole geometry

Accurately modeling the x-ray source and pinhole geometry is a critical step in the modeling process. Our previous validation work has shown that simplifying the x-ray source and pinhole structure combination to a perpendicular incoming beam produces results that are much sharper than those produced with the correct x-ray

source and pinhole geometries[109].

For these simulations, the x-ray focal spot was modeled as a circle with $100\mu m$ diameter and a parallel beam. The true focal spot has a similar shape, but with two bright lobes and does not emit parallel rays. Images of the experimentally measured focal spot of the x-ray tube used in this paper can be found in Figure 6a of Ref.[110].

In order to verify the pinhole structure, digital optical microscopy images (High-Magnification Digital Microscope System VHX-100, Keyence Corporation of America, Woodcliff Lake, NJ) were taken of the front and back surfaces of the pinhole disk. Measurements from the digital images give a diameter of 35.5 μm for the small end of the 30 μm pinhole and a diameter of 215 μm for the large end. These diameters are within approximately two times the pinhole manufacturer's errors.

Although the actual pinhole diameters were measured before the simulations were performed, the pinhole diameters used in the simulations were taken directly from the manufacturer's specifications. This decision was made because the optical microscopy measurements did not allow for measurement of the internal structure of the pinhole. However, the measured pinhole outer diameters did deviate slightly from the manufacturer's specifications (35.5 μm versus 30±5 μm for the smaller diameter and 215 μm versus 229±5 μm for the larger diameter).

In order to determine the error incurred by an incorrectly modeled pinhole diameter, we re-ran simulations similar to those described in Section 2.3.2 with a pinhole diameter of 36 μm for Screen 1 at 0 degrees and 70 kVp. The resultant FOM was 0.3528 ± 0.0089 as compared to 0.3552 ± 0.0133 for the original diameter

47

(30 μm). The difference between these two values is 0.0024 $\pm$ 0.0160, so the change in the FOM calculation is negligible. The small change in the FOM with pinhole diameter is due to the fact that the diameter of the pinhole is only determined by a very thin layer at the end of the pinhole, and the majority of the pinhole structure is a larger cone that is unaffected by the specified diameter.

Another potential source of error is the positional error incurred by the manner in which the pinhole is mounted in the cap screw head. This is done by applying super glue between the pinhole disk and the hole machined in the screw head and positioning them by hand. Although the machined hole in the screw head guides the pinhole, it is not an exact fit because the machined hole is somewhat over-sized. We anticipate the error in the pinhole disk position to be less than $\pm$0.5 mm horizontally and less than $\pm$1 degree in angle.

2.4.4 Blur due to FOP

The FOP is a potential source of image degradation, although its effect should be small given that the fibers are 4.5 μm in diameter. To quantify the image degradation imposed by the FOP, a resolution phantom (Edmund Optics 1951 USAF Resolution Target 2" Square Negative #NT38-256, Barrington, NJ) was placed in pressure contact with the FOP and a polychromatic, diffuse light source was placed in front of the resolution phantom. The light source was constructed by placing a set of light emitting diodes inside of a white Styrofoam box with a diffuser placed at the output. Note that the resolution phantom was made of glass and of a similar size to

48

the CsI scintillator screens, making the contact of the resolution phantom similar to that of the CsI scintillator screens. In this phantom, the pattern representing 45.3 line pairs per mm (lp/mm) (Group 5, Element 4) is resolvable in both axes of the detector. A resolution of 45.3 lp/mm corresponds to a resolution of 11.0 μm, only slightly greater than the pixel size of the detector (9.0 μm). Therefore, while the FOP may induce a slight blur on the image, its effect should be on the order of the size of a single CCD pixel.

2.4.5 Columnar tilt angle and incident x-ray beam

For the simulations presented in this paper, the tilt angle of the columns was always along the same direction as the oblique angle of x-ray incidence. Experimentally, however, the true orientation of the columns with respect to the incoming x-ray beam is unknown. This leads to a possible inconsistency between the experimental and simulated data that may affect the comparison between the two. To investigate the magnitude of this effect, we also simulated PRFs with a columnar tilt angle directly opposite the oblique angle of the incident x-ray beam (180 degrees rotated from the original data) to explore a range of possible orientations. This was done for Screen 2 with a 40 kVp spectrum and all of the incidence angles. For the original PRFs the FOMs were 0.3901 ± 0.0209, 0.4124 ± 0.0310, 0.3932 ± 0.0086, and 0.3685 ± 0.0208 for 0, 15, 30, and 45 degrees, respectively. For the new PRFs, with the modified tilt angle, the FOMs were 0.4015 ± 0.0091, 0.3830 ± 0.0038, 0.3997 ± 0.0079, and 0.4583 ± 0.0400 for 0, 15, 30, and 45 degrees. If we take the

49

difference of each of these values divided by the error in the difference we get 0.5001, 0.9413, 0.5566, and 1.9918 for 0, 15, 30, and 45 degrees, respectively. This means that changing the orientation of the columnar tilt angle will change the FOM by about the same order as the error in the measurements. Therefore, we do not expect this effect to significantly affect the results.

2.5 Conclusion

The results presented in this paper provide experimental validation of the MANTIS package for a variety of experimental conditions. Investigators applying MANTIS to various imaging systems now have a better understanding of both its strengths and limitations. Such detailed models of scintillator screen response have important implications in the optimization of x-ray imaging systems and reconstruction of three-dimensional images from planar data. Optimization that does not take into account accurate detector properties may produce misleading results and the inclusion of models like MANTIS can result in more accurate reconstructions since the forward problem is better characterized. Improvements in optimization and reconstructions of x-ray data have the potential to improve image quality and, as a result, detection of abnormalities and disease in these types of images. While the long timescales of MANTIS simulations make rigorous optimizations difficult at present, we are currently developing a fast, analytical model to approximate PRFs produced by MANTIS [111]. Such a model will allow for rapid generation of detector PRFs and make inclusion of these detailed detector simulations in complex opti-

mization or forward-problem models of 3D x-ray imaging systems possible and even straightforward.

Chapter 3

A fast, angle-dependent, analytical model of CsI detector response

for optimization of 3D x-ray breast imaging systems

3.1   Overview

Optimization[1] of three-dimensional (3D) breast x-ray imaging systems and 3D image reconstruction methods rely on assumptions about detector performance. The deterministic blur introduced by the detector can be quantified by the point response function (PRF), which is the resultant image of an infinitely thin x-ray pencil beam. The current approach to modeling detector performance assumes that the PRF has a symmetric shape that is invariant over the detector area [112, 113]. In some cases, detector blur is ignored altogether [114, 115]. However, recent studies [106, 117, 108] have demonstrated that there are large variations in the PRF across the detector face and that it can be highly asymmetric for large incidence angles. A recent study measured the MTF of an experimental bench-top tomosynthesis system with a flat panel indirect detector as used in a GE Senographe 2000D system [106]. The source-detector distance was 112 cm and the object-detector distance was 5 cm. X-ray incidence angles of 0, 10, 20, 30, 40, and 50 degrees were investigated for two different x-ray spectra (26 kVp Mo/Mo and 40 kVp Rh/Al with an additional 1 mm Al filter). A decreasing MTF with incidence angle demonstrated that the detector

---

[1]Work in this chapter published in Medical Physics [111].

performance deteriorates significantly as the incidence angle increases.

In addition, the recent development of a detailed Monte Carlo simulation code (MANTIS [90, 116])[2] for studying the imaging performance of modern CsI columnar phosphor screens has demonstrated similar variations in the PRF over the detector face for both breast tomosynthesis and CT-like geometries. Badano et al. [117] investigated a tomosynthesis geometry with a source-to-detector distance of 60 cm and an angle between the chest wall and the edge of the x-ray beam of 11.3 degrees. The detector was a small mammography detector with a size of 24×12 cm and a phosphor screen thickness of 150 μm. The x-ray tube was allowed to rotate on an arc centered about the detector plane with an angular range of ±20 degrees. Three different x-ray spectra were considered (Mo/Mo at 28 kVp, Rh/Rh at 28 kVp, and W/Al at 42 kVp) as well as three different breast thicknesses (3, 4, and 6 cm). This geometry resulted in x rays entering the phosphor screen at angles of up to 45 degrees. The PRFs showed significant anisotropy and increased blurring as compared to normal x-ray incidence. In another paper, simulations were carried out for a breast CT system [108]. This system had a source-to-isocenter distance of 44 cm, a source-to-detector distance of 88 cm, and a 30 × 40 cm detector with a 600 μm thick phosphor screen, with x-ray energies of 30 to 70 keV. Increases in blur with respect to normal x-ray incidence were measured by performing a two-dimensional (2D) Gaussian fit to the PRFs and dividing the major axis of the fitted Gaussian with the major axis of the fitted Gaussian at zero degrees incidence. For

---

[2]A current version of the code, tutorials, and examples are available from `ftp://150.148.3.14/mantis`

the investigated x-ray energies and incidence angles, the measured blur values were as high as 1.86. Also, the maximum aspect ratios of the PRFs ranged from 1.14 to 2.53 depending on the contour level for the height of the PRF chosen for the analysis.

Unfortunately, because of the long simulation times required for the detailed MANTIS code (approximately 200 hours on a single 3 GHz CPU for a PRF with 500,000 primary x rays), accurate PRFs have yet to be incorporated into optimization and reconstruction schemes. In this work, we have developed a closed-form, deterministic, analytical model that approximates the detailed Monte Carlo simulations in less than one millionth of the computation time (about 0.1 s). The model describes the depth-dependent deterministic response of the detector. In addition, our model could be used to simulate the noise component present in indirect detectors due to variations in the optical processes. The analytical model has been developed for a single CsI phosphor thickness (150 μm), x-ray energy (25 keV), and four incidence angles (0, 15, 30, and 45 degrees). Future expansion of the model to a larger range of parameters will allow for rapid, on-the-fly generation of PRFs that will enable the inclusion of realistic detector performances in system optimization and reconstruction.

In Section 3.2 the detailed derivation of the PRF model is presented. Calculation of the best fit coefficient values as well as a quantitative comparison with MANTIS-generated PRFs is discussed in Section 3.3. Section 3.4 gives the results of a comparison of the analytical model with experimental data. Finally, conclusions are provided in Section 3.5.

54

3.2 The model

The objective of this analytical model is to produce a deterministic PRF for a given set of system parameters. Therefore, all incident x rays are specified to arrive at the same location, $(x, y, z) = (0, 0, 0)$, and with the same incidence angle, (θ, ϕ). Additionally, we assume a monochromatic incident beam with energy, E. The general approach used in this model can be broken down into two major steps. In the first step (discussed in the remainder of this section), we model the physics of the interaction between the incoming x-ray beam and the CsI crystal. This analysis produces an analytical expression that describes the shape of a PRF for a given set of input parameters. In the second step (see Section 3.3), the free parameters in the analytical expression are adjusted by fitting that expression to PRFs produced using MANTIS.

In the first step, we have ignored the columnar structure of the CsI crystal in the mathematical formulation and made the assumption that it is a homogeneous, solid slab. Although the effects of columnar structure are not explicitly included in the mathematics, they are indirectly included by using MANTIS data as a guide to choosing the functional forms of the relevant physical properties. In addition, the second step incorporates the columnar structure and other secondary effects by adjusting the free parameters in the model based on MANTIS data. Figure 3.1 shows a schematic of the model geometry and coordinate system, while Table 3.1 gives definitions for variables used in the derivation of the model.

Four separate effects in the x-ray detection process are modeled in the first
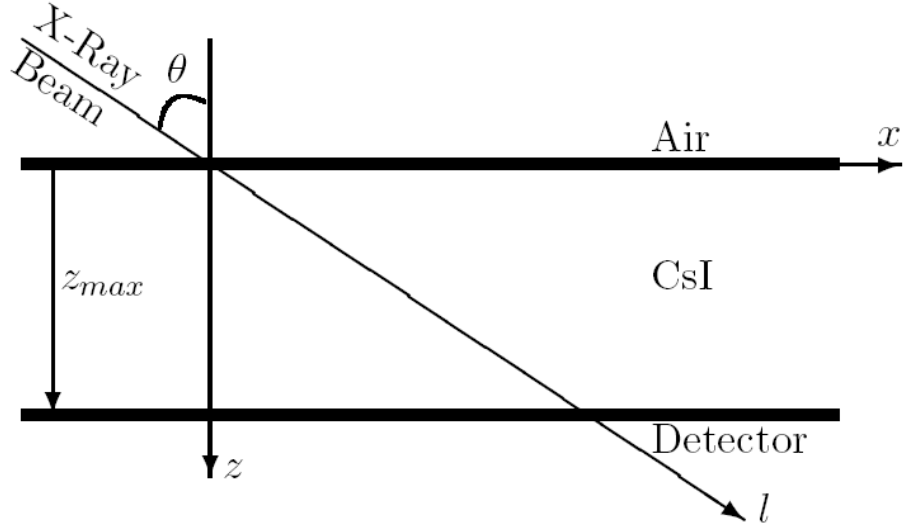
Figure 3.1: Schematic of model geometry and coordinate system. The view is a vertical cut through the CsI crystal looking from the side with the air interface on the top and the detector layer at the bottom of the schematic. The infinitely thin incident x-ray beam enters at an angle 90 degrees minus θ from the x axis (ϕ, 90 degrees minus the angle between the x-ray beam and the y axis, is assumed to be zero in this diagram). The y axis is going out of the page in this view.

Table 3.1: Definition of model variables.

Symbol		Definition
(x, y, z)	$\equiv$	x ray interaction location
		(z = depth in crystal)
		$(0, 0, 0)$ = x-ray crystal entrance
l	$\equiv$	Position along x ray travel direction
		(=0 at x-ray crystal entrance)
		$= \sqrt{x^2 + y^2 + z^2}$
θ	$\equiv$	90 deg minus the angle between the l and x axes
		($\sin\theta = x/l$)
ϕ	$\equiv$	90 deg minus the angle between the l and y axes
		($\sin\phi = y/l$)
z_{max}	$\equiv$	Thickness of crystal
$\mu_{pe}(E)$	$\equiv$	Photoelectric attenuation coefficient of CsI [cm^{-1}]
$\mu_{tot}(E)$	$\equiv$	Total attenuation coefficient of CsI [cm^{-1}]
E	$\equiv$	Energy of incident x rays [keV]
N_o	$\equiv$	Number of incident x ray photons
γ	$\equiv$	X ray to optical photon gain factor [keV^{-1}]

step of our approach. The first is the depth-dependent absorption of the incident x rays. The second is the conversion of absorbed x rays into emitted optical photons by the CsI crystal. The third is the self-absorption of the emitted optical photons in the CsI crystal and the absorption of the photodiode layer. Finally, the fourth is the depth-dependent spread of the optical photons collected at the exit plane of the crystal. The following subsections describe each of these effects in detail and then integrate the final depth-dependent model over the crystal thickness to get an analytical expression for the overall PRF.

3.2.1 Depth-dependent absorption of incident x rays

Gallas et al. [118] derived a model for image formation with indirect x-ray powder-phosphor based detectors. Following their analysis, the rate at which x-ray photons interact with the crystal as a function of crystal depth is given by

$$N_i(z, \theta, \phi, E) = N_o \, \eta_{xray}(z, \theta, \phi, E), \tag{3.1}$$

where $\eta_{xray}(z, \theta, \phi, E)$ is the x-ray interaction probability for a given depth.

Here we restrict our analysis to consider only x rays that interact with the crystal via the photoelectric effect to produce an optical-photon shower that can subsequently be detected with a photodiode array. Therefore, we can further write

$$N_{pe}(z, \theta, \phi, E) = \frac{\mu_{pe}(E)}{\mu_{tot}(E)} \, N_i(z, \theta, \phi, E) \tag{3.2}$$

as the number of photons that interact with the CsI crystal to produce an optical-

57

photon shower, where $\mu_{pe}(E)$ is the photoelectric attenuation coefficient of the crystal. Figure 3.2 shows the importance of different interaction types at energies applicable to breast imaging. The total mass attenuation coefficient as well as the contributions to the total mass attenuation coefficient due to the photoelectric, Rayleigh, and Compton effects are shown as a function of energy in the range of 5-100 keV. These values were calculated using pure CsI in the Monte Carlo simulation package PENELOPE [104, 119]. The photoelectric effect is the dominant interaction type for this energy range and constitutes 89.3 - 99.4% of the total mass attenuation coefficient. Note that the fitting algorithm discussed in Section 3.3 should help compensate for the Compton and Rayleigh contributions to the detected signal that are not included in the model.

To calculate $\eta_{xray}(z, \theta, \phi, E)$ as a function of depth, we can start by writing from first principles the same expression as a function of position along the travel direction

$$\eta_{xray}(l, \theta, \phi, E) = \mu_{tot}(E) \exp\left(-\mu_{tot}(E)l\right). \tag{3.3}$$

In order to write this as a function of crystal depth (z) we can relate l and z with the following equation

$$l = \frac{z}{\sqrt{\cos^2 \theta - \sin^2 \phi}} \tag{3.4}$$

and replace l by z in Equation 3.3 to get
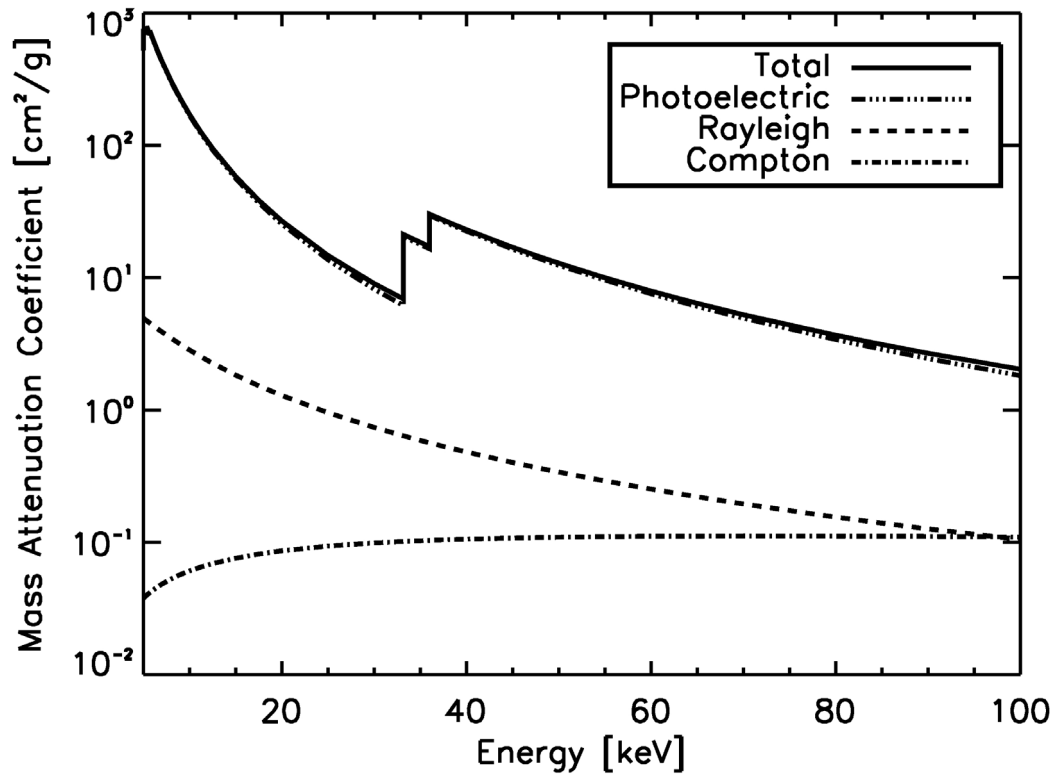
Figure 3.2: Mass attenuation coefficient as a function of energy for CsI as simulated in PENELOPE. The photoelectric, Rayleigh, Compton, and total mass attenuation coefficients are shown. The photoelectric effect is the dominant interaction over the energy range of 5-100 keV.

$$\eta_{xray}(z, \theta, \phi, E) = \mu_{tot}(E) \exp\left(-\frac{\mu_{tot}(E)\, z}{\sqrt{\cos^2\theta - \sin^2\phi}}\right). \tag{3.5}$$

This equation describes the expected behavior of the crystal. However, inclusion of this full form in the analytical model makes the solution intractable. As a result, we approximate the exponential behavior with a linear function given by

$$\eta_{xray}(z, \theta, \phi, E) \approx a_0(E)\, z + a_1(E) \tag{3.6}$$

so that

$$N_{pe}(z, \theta, \phi, E) \approx N_o\, \mu_{pe}(E)\left[a_0(E)\, z + a_1(E)\right]. \tag{3.7}$$

Figure 3.3 shows a comparison of a least-squares linear approximation with the full exponential form for an energy of 25 keV corresponding to that typically used in mammography and breast tomosynthesis. Final values for a_0 and a_1 will be determined by the 2D fit as described in Section 3.3. For lower energies Equation 3.6 may be extended to include a z^2 term, however due to the increased complexity of the solution, we maintain the linear solution for this study.

3.2.2 Conversion of absorbed x rays into emitted optical photons

We assume that, on average, the number of optical photons produced per x ray is given by a function of x-ray energy, $K(E)$, so that the average number of optical photons produced at a given z is written as
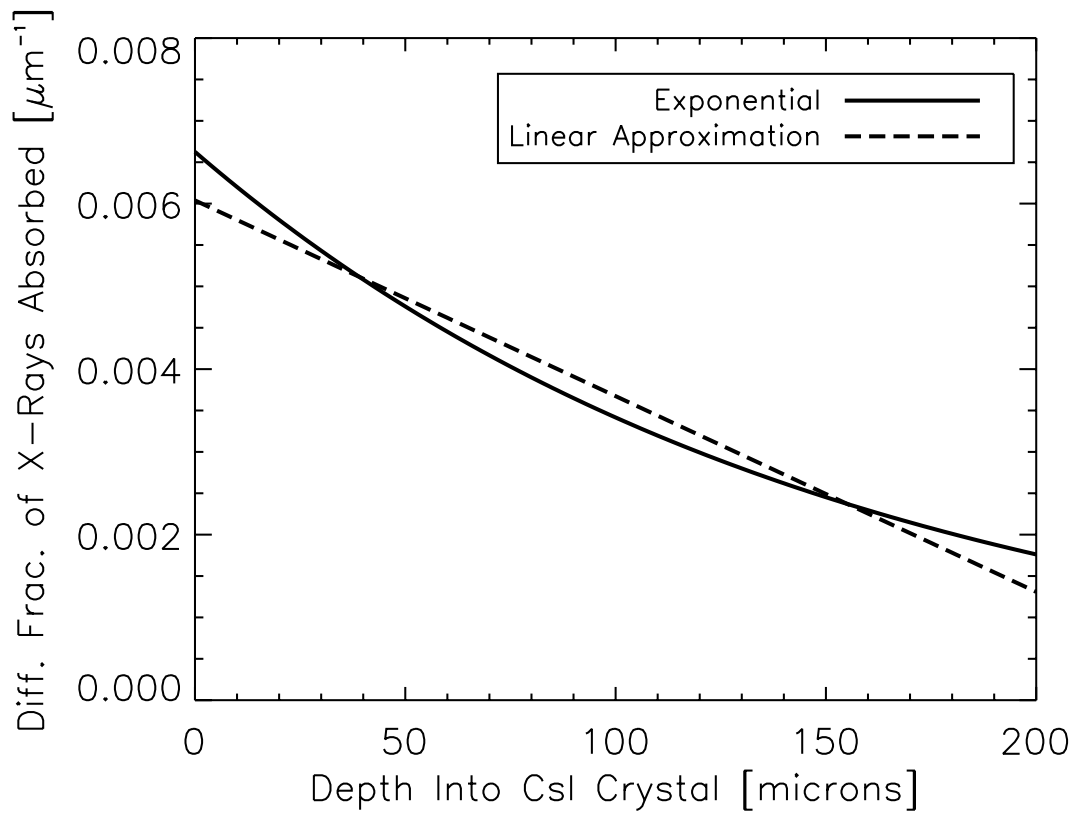
Figure 3.3: Comparison of exponential x-ray absorption profile with a least-squares linear approximation for 25 keV. The exponential profile is indicated with a solid line and the linear approximation with a dashed line.

$$N_{opt}(z, \theta, \phi, E) = K(E)\, N_{pe}(z, \theta, \phi, E). \tag{3.8}$$

Following Gallas et al. [118], $K(E) = \gamma E$, where γ is a material dependent gain factor and has units of keV^{-1}. For CsI $\gamma \approx 60$ photons/keV [120, 121].

3.2.3 Self-absorption and photo-detector absorption of the emitted optical photons

Some of the optical photons that are produced do not reach the photo-detector because of crystal self-absorption, absorption efficiency of the photodiode layer, scatter, or other effects. We can express the number of collected optical photons that reach the base of the CsI crystal as

$$N_{collect}(z, \theta, \phi, E) \;=\; N_{opt}(z, \theta, \phi, E)\, \zeta(z), \tag{3.9}$$

where $\zeta(z)$ is the optical collection efficiency or the percent of emitted optical photons that are detected. The notation $\zeta(z)$ is taken from Gallas et al. [118]. To determine the functional form of $\zeta(z)$ we can use MANTIS as a guide. Figure 3.4 shows the results of simulations in MANTIS[3] where optical photons are generated at different depths in the CsI crystal and the optical collection efficiency is recorded. MANTIS takes into account the reflectivity of the photodiode layer as well as the photodiode absorption efficiency as a function of wavelength. The MANTIS results are shown as black dots and a linear least-squares fit is shown as a solid line. Given

---

[3]by Aldo Badano
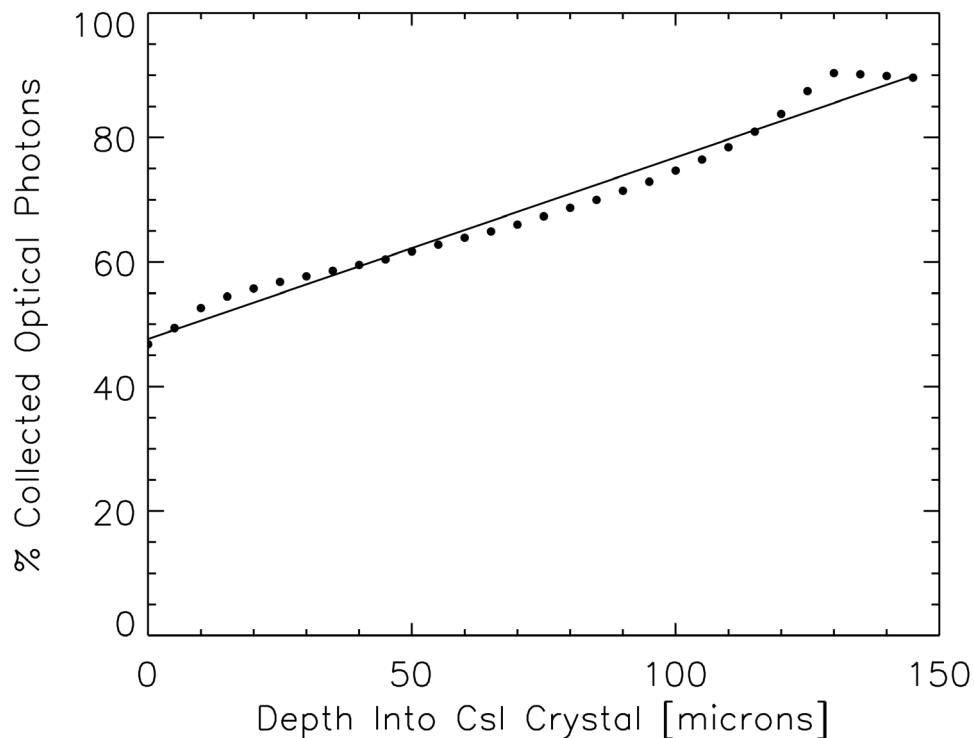
Figure 3.4: Percent of emitted optical photons at a specific depth that reach the photo-detector. Results from MANTIS simulations are shown as black dots, and a linear fit to that data is also shown. This information resulted in the use of a linear model for the crystal self-absorption.

this data we assume that the functional form of the optical collection efficiency is

linear and given by

$$\zeta(z) = b_0\, z + b_1. \tag{3.10}$$

3.2.4 Depth-dependent spread of optical photons

Once an optical-photon shower is produced, those photons are detected by the

photodiode with a specific spread that depends on the depth at which the optical

photon shower was initiated. To determine the functional form of this spread, a series of MANTIS simulations were run[4] in which optical-photon showers, with 10,000 optical photons each, were initiated at different depths in a 150 μm thick CsI crystal and the resulting photon spreads were recorded. The depths probed were from 0 to 145 μm at intervals of 5 μm.

For the CsI crystal simulated in MANTIS, depths of 0 to 120 μm had a columnar structure and depths of 120 to 150 μm corresponded to homogeneous CsI. This choice for the transition between the columnar and homogeneous layers was motivated by previous work where scanning electron microscope images were taken of a variety of screens to characterize the screen layers (see Chapter 2). Three different functional forms of the photon spread were considered; Gaussian, exponential, and Lorentzian. Each of these was fit to the normalized, radially-averaged MANTIS-generated optical-photon spread at each probed depth. The normalization was performed by dividing by the maximum of the radially-averaged profile. Figure 3.5 shows examples of these fits for two different depths (5 μm and 145 μm). The radially-averaged MANTIS spread is shown as a solid line while the Gaussian, Lorentzian, and exponential fits are shown as dotted, dashed, and dashed-dotted lines respectively. The difference in width of the spreads at the two different depths is clearly demonstrated in this figure and qualitatively we can see that the Lorentzian appears to fit the MANTIS data better than either the Gaussian or exponential. In particular, the Lorentzian curve is much better than either the exponential or the Gaussian at matching the MANTIS results in the tails of the curves. The root mean squared (RMS) deviations

---

[4]by Aldo Badano

from the MANTIS simulation results for each of these three functional forms are shown in Figure 3.6. This figure verifies that the Lorentzian gives a better fit, in terms of RMS deviation on the radially-averaged data, than either the Gaussian or exponential functional forms for every depth investigated. Therefore, we chose to model the optical photon spread as a Lorentzian function. If we look at the fits in more detail (see Figures 3.5 and 3.6), we can see that the Lorentzian performs somewhat better for optical photons that are absorbed deep in the crystal, but still located in the columnar zone. When the optical photons are produced closer to the crystal exit plane, the Lorentzian tends to overestimate both the tails and the peak of the spread, while for optical photons produced further from the optical detector, the Lorentzian tends to underestimate both the tails and the peak.

The two dimensional, symmetrical version of a Lorentzian function can be written as

$$L(x, y) = \frac{c_0}{1 + c_1^2 \left[(x - c_2)^2 + (y - c_3)^2\right]}, \tag{3.11}$$

where c_0 is the amplitude of the Lorentzian, c_1 is $\frac{2}{\Gamma}$, Γ is the FWHM of the Lorentzian, c_2 is the shift of the Lorentzian in the x direction, and c_3 is the shift of the Lorentzian in the y direction. Comparing with our PRF model, we find that

$$c_0 = N_{collect}(z, \theta, \phi, E), \tag{3.12}$$

65
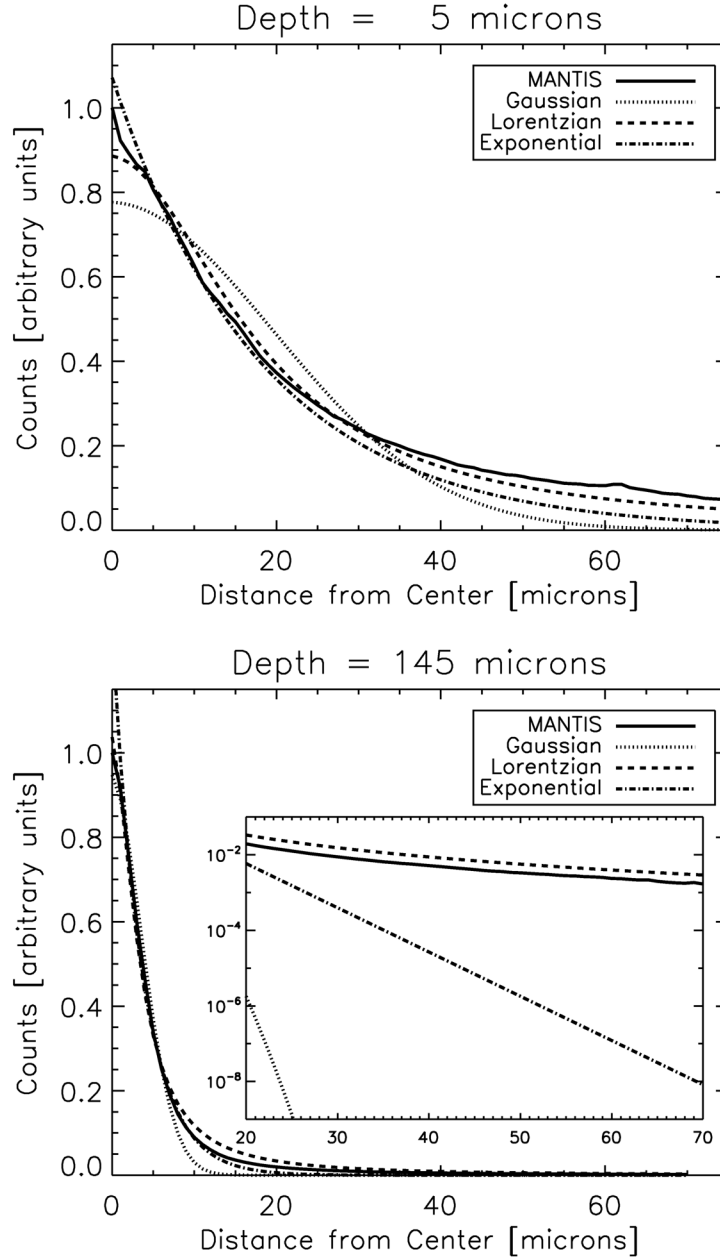
Figure 3.5: Plots showing the normalized, radially-averaged simulated optical photon spread from MANTIS for two different depths; (top) 5 μm and (bottom) 145 μm with a zoom of the tails in the inset plot. The depth refers to the distance in the z direction between where the x-ray beam enters the CsI crystal and where the x ray is absorbed and produces the optical shower. The black lines show the radially averaged MANTIS results normalized to the maximum of the radially averaged profile. Fits of Gaussian, exponential, and Lorentzian functions are also shown. The Lorentzian shows the best overall fit to the data. In general, for optical photons produced deeper in the crystal, the Lorentzian tends to overestimate both the tails and the peak, while for shallower depths, it tends to underestimate both the tails and the peak.
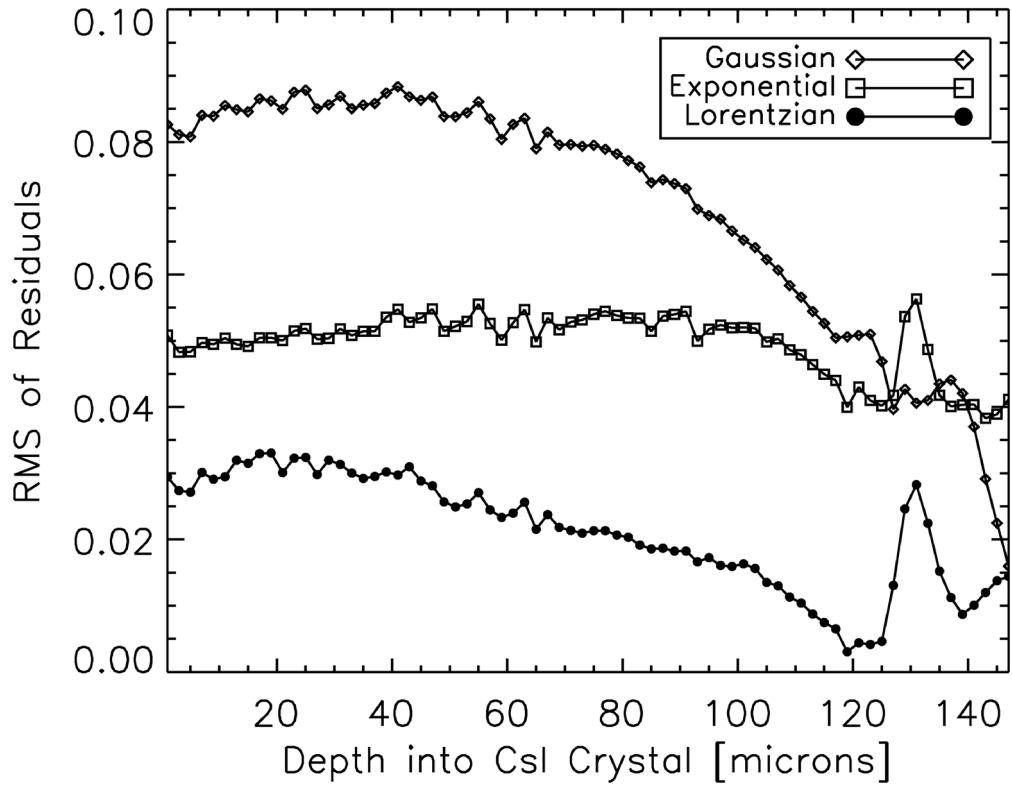
Figure 3.6: Analysis to determine the functional form of the spread of optical photons that reach the detector after being generated at a specific depth. MANTIS simulated data were generated for depths in the crystal between 0 and 145 μm and Gaussian, exponential, and Lorentzian fits were performed to the radial average of the MANTIS results to determine the functional form of the spread. The RMS of the residuals of these fits are shown as a function of the depth at which the optical photon shower was generated. The Lorentzian function gives the smallest RMS residuals for all depths.

$$c_2 = z \tan \theta, \tag{3.13}$$

and

$$c_3 = z \tan \phi. \tag{3.14}$$

In order to determine the functional form of Γ as a function of depth, we plotted the FWHM of the Lorentzian fits as a function of depth (see Figure 3.7). The reader can see that this is a complicated relationship that is poorly described by a simple analytical form. Nonetheless, in order to allow for a fully analytical solution, we approximate this relationship by a linear functional form given by

$$\Gamma = g_0 z + g_1. \tag{3.15}$$

Note that this approximation matches the MANTIS data well over the bulk of the crystal, but poorly at both very small and large depths in the crystal. Further research is needed to understand the physical origin of the downturn of Figure 3.7 at small depths, however, it is likely related to the transport of photons near the interface of the organic polymer layer (a protective top coat) with the layer of columnar CsI. At very large depths, there is a sharp spike in the width because of the fact that the columnar to homogeneous CsI transition is modeled as a discontinuous change in MANTIS. Since this transition is more gradual in reality, we expect the
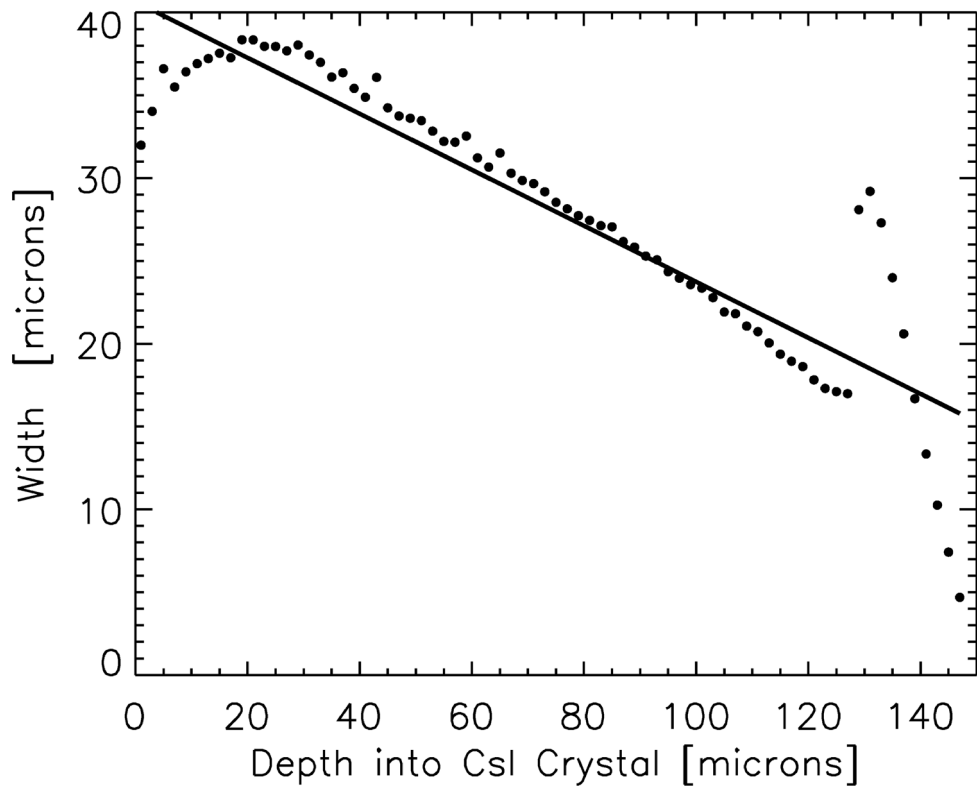
Figure 3.7: FWHM of Lorentzian fits to MANTIS data as a function of depth where the optical photons were generated. The MANTIS data are shown as dots, while a linear fit is shown as a solid line. A linear relationship was used to model the width of the spread as a function of depth in the mathematical model.

linear approximation to apply better to experimental data. Also, note that the majority of x rays are absorbed at shallow depths in the crystal because of the exponential x-ray absorption, and optical photons generated at very shallow depths in the crystal are more likely to be re-absorbed before they can reach the photodiode layer. As a result, we expect the majority of signal that makes up the PRF to arise from interactions in the middle of the crystal depth, where our linear approximation most accurately reproduces the MANTIS data.

3.2.5   Integrate model

The final analytical expression for the depth-dependent PRF, PRF_z, can be derived by combining Equations 3.7-3.15 to get

$$
\begin{aligned}
PRF_z&(x, y, z, \theta, \phi, E) = \\
&\frac{\gamma E N_o\, \mu_{pe}(E)\, [a_0\,(E)\, z + a_1\,(E)]\, (b_0\, z + b_1)}{1 + \left(\frac{2}{g_0 z + g_1}\right)^2 [(x - z \tan\theta)^2 + (y - z \tan\phi)^2]}.
\end{aligned}
\tag{3.16}
$$

In order to obtain the overall PRF we must integrate this equation over depth,

$$
PRF(x, y, \theta, \phi, E) = \int_0^{z_{max}} PRF_z(x, y, z, \theta, \phi, E)\, \mathrm{d}z.
\tag{3.17}
$$

The solution to this integral is given in Appendix A. Because of the length of the solution it is not reproduced here. Note that the contribution to the PRF from any given depth is symmetric. The asymmetry in the overall PRF comes from the depth-dependent shift of each of these contributions due to the incidence angle of the incoming x-ray beam.

70

3.3 Calculating best fit coefficient values and comparison with MAN-

TIS

The analytical solution for the PRF (derived in Appendix A) requires the following variables to be specified by the user; incident angles of x-ray beam (θ, ϕ), energy of incident x-ray beam (E), and the thickness of the CsI screen (z_{max}). The remaining variables are p ($\equiv \gamma E N_o \mu_{pe}(E)$) from Eqn. A.3, $a_0 (E)$ and $a_1 (E)$ from Eqn. 3.6, b_0 and b_1 from Eqn. 3.10, and g_0 and g_1 from Eqn. 3.15. Recall that p controls the maximum value of the overall PRF, a_0 and a_1 are the slope and intercept of the function that describes the absorption of x rays in the CsI crystal as a function of depth, b_0 and b_1 are the slope and intercept of the function that describes the optical collection efficiency, and g_0 and g_1 are the slope and intercept of the function that describes the width of the depth-dependent optical photon spreads at the exit plane.

While approximate values for each of these variables could be taken from the analysis in Sections 3.2.1, 3.2.3, and 3.2.4, the analysis of those Sections was intended solely to determine an appropriate functional form for the physical process being analyzed. As a result, to determine the optimal values of these variables we have performed a fit of the full two-dimensional PRF solution to two-dimensional MANTIS generated PRFs. The results of Sections 3.2.1, 3.2.3, and 3.2.4 are used as initial guesses to this fit. The 2D fitting process allows factors that have not been explicitly included in the analytical model (*i.e.*, columnar crystal structure, reflective substrates, k-fluorescent x rays) to be indirectly accounted for. For example, we

expect columnar structure in the CsI crystal to decrease the width of the optical spread functions as compared with a homogeneous crystal slab. By allowing the width of the spread to vary as a free parameter, this property of the crystal can be taken into account albeit without explicit inclusion in the derivation of the analytical form of the PRF.

Two dimensional fits of the analytical model to the MANTIS-generated PRFs were performed using a figure-of-merit (FOM) equal to the the RMS normalized difference of the two PRFs within a region-of-interest (ROI). A smaller FOM indicates a better fit. A mathematical definition of the FOM was given in a previous study (see Chapter 2), were it was used to compare MANTIS PRFs to experimental data. Here, the ROI was chosen by selecting all pixels with a signal of at least a fortieth of the maximum of the MANTIS PRF. This ROI was chosen to include some of the tails of the PRFs without including regions that were noisy in the MANTIS simulations due to the number of simulated primary x rays. A sparse sampling method was used to perform the fit and was calculated as follows:

1. For each of the 7 coefficients to be fit (p, $a_0(E)$, $a_1(E)$, b_0, b_1, g_0, g_1), choose 5 evenly spaced initial guesses. For p the initial guess was chosen as the maximum value of the MANTIS-generated PRF, while initial guesses for the other 6 coefficients were taken from the analysis in Sections 3.2.1, 3.2.3, and 3.2.4. The range of the 5 initial guesses was chosen to reasonably cover the likely possible values.

2. Generate analytical PRFs at each angle of interest (0, 15, 30, and 45 degrees

72

in this study) for every possible coefficient combination and calculate the corresponding FOMs for each angle. Calculate an overall FOM equal to the sum of the FOMs for each angle. Note: In this fitting scheme all 7 coefficients are forced to be the same for all angles.

3. Identify the coefficient combination with the lowest calculated overall FOM.

4. Select a new set of 5 evenly spaced trial coefficient values, where three of those new trial coefficient values are the coefficient value with the lowest overall FOM and its two nearest neighbors. The final two trial coefficient values are directly in between the other three values. If the coefficient with the lowest overall FOM is on the edge of the grid, the grid is expanded to include a larger range of coefficient values.

5. Return to Step 2 unless the difference between the trial coefficient values is less than 10^{-6} for p, 10^{-8} for $a_0\,(E)$, and 10^{-5} for $a_1\,(E)$, 10^{-2} for b_0, 10^{-2} for b_1, 10^{-4} for g_0, 10^{-2} for g_1. These thresholds were chosen to achieve a specific accuracy of the fitted parameter that seemed reasonable for its physical meaning. It was confirmed that the choice of these thresholds resulted in an overall FOM that stabilized during the fitting process (see text below). Once a single coefficient value has dropped below the threshold, it's value is fixed at that value and the other coefficients continue to be varied.

In this study, we have performed fits to a limited number of input parameters to demonstrate the ability of the analytical model to fit MANTIS-generated PRFs.

Specifically, we have focused on a CsI scintillator thickness of 150 μm, an x-ray energy of 25 keV, and incidence angles of 0, 15, 30, and 45 degrees. The remainder of the CsI screen model parameters are identical to those presented in Badano *et al.*[117] except for the reflective backing, where a reflectivity value of 95% was used in the current study. These input parameters are similar to system parameters found in mammography and tomosynthesis measurements. In a future study, we will perform fits over a larger range of different angles, energies, and CsI thicknesses and provide relationships to determine the optimal coefficient values for the entire range of explored input parameters. Figure 3.8 shows how the overall FOM changed over the course of the fitting process. Fractional change in the FOM is plotted as a function of iteration number of the 2D fitting program for the combination of 0, 15, 30, and 45 degrees incidence angles. The overall FOM decreases monotonically and reaches a stabilized value well before the end of the fitting process. The pre- and post-fit coefficient values for the investigated set of parameters and choice of CsI screen are given in Table 3.2. Please note that these coefficients are not appropriate descriptors for a general imaging CsI screen and should not be used as representative values. The coefficients are valid only for a monoenergetic x-ray beam of 25 keV, a CsI scintillator screen with a thickness of 150 μm and similar properties to those mentioned in Badano *et al.*[117], and incidence angles ranging from 0 up to 45 degrees. Also, note that we have performed a comparison here for incidence angles in the direction of ϕ=0. We expect the analytical model to perform equally well for incidence angles in the ϕ and θ directions. The only physical effect modeled in MANTIS that changes between the θ and ϕ directions is the columnar tilt and this
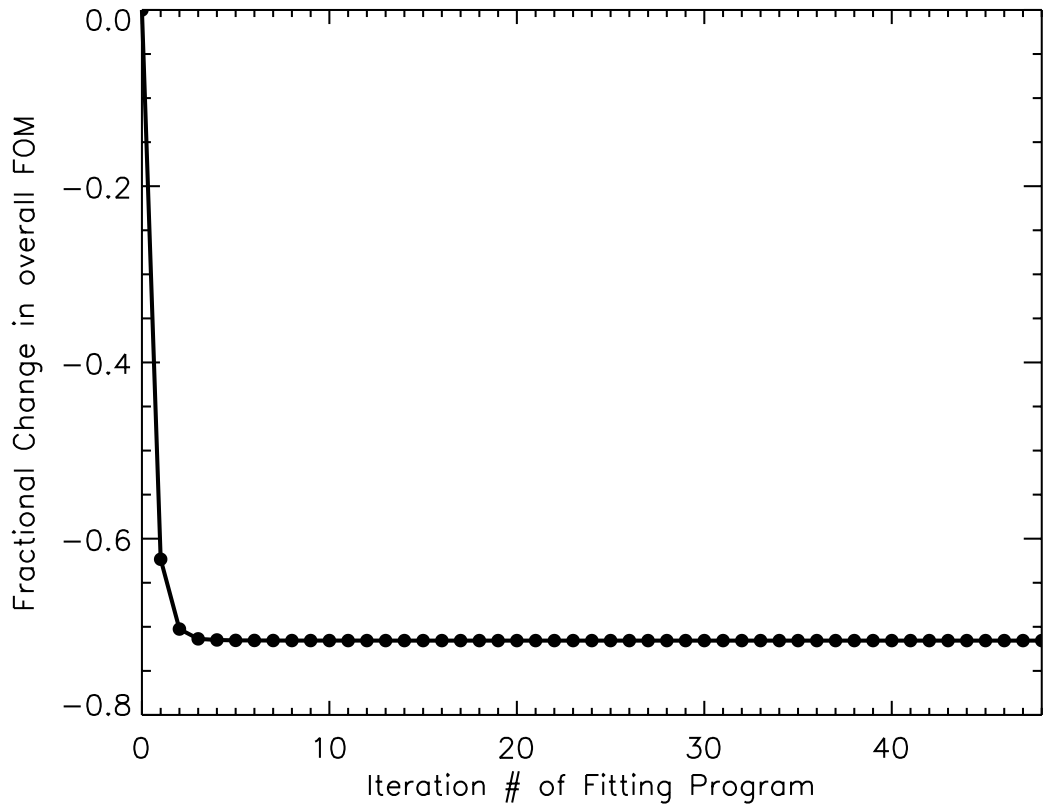
Figure 3.8: Fractional change in the overall FOM during the 2D fitting process as a function of the iteration number of the fitting program. Data are shown for a 25 keV monochromatic incoming beam, 150 μm thick CsI screen, and the combination of 0, 15, 30, and 45 degree incidence angles. The overall FOM stabilizes well before the end of the fitting procedure.

has been shown previously to have a small effect when integrating over large pixels

(100 μm or more) (see Chapter 2). The model should also be valid for all detector

locations assuming that the structure of the detector is independent of location.

Figure 3.9 shows a comparison between the MANTIS-generated PRFs and the

analytical model PRFs after performing the 2D fitting process. All of the PRFs

shown have been generated with a CsI scintillator thickness of 150 μm, an incident

x-ray energy of 25 keV, and 500,000 primary x rays. The left-most column indicates

Table 3.2: Best-fit coefficient values for a 25 keV monochromatic beam, 150 μm thick CsI screen, and angles in the range of 0 to 45 degrees. These coefficients should be valid for any detector location as long as the same screen model applies. The results reported here correspond to the PRFs shown in Figures 3.9 and 3.10.

Coefficient	Pre-fit Value	Best-fit Value (25 keV, 150 μm CsI)
p	0.00878561	0.000878561
$a_0(E)$	-2.3649709e-5	1.1078126e-5
$a_1(E)$	0.0060386894	0.014294919
b_0	0.291616	0.0302214
b_1	47.6439	37.843750
g_0	-0.169079	0.033398382
g_1	40.6468	13.320312

the incidence angle of the incoming x-ray beam. The corresponding PRFs from MANTIS and the analytical model are shown in the following columns as well as the FOMs comparing those PRFs. FOM values and their errors were calculated as the mean and standard deviation of comparisons of the analytical model results with 11 independent MANTIS-generated PRFs. The right-most column shows the FOMs from a comparison between MANTIS and a 2D symmetric Gaussian fit to the zero angle MANTIS PRF. These numbers are provided to give a reference for the FOMs comparing MANTIS and the analytical model. A 2D symmetrical Gaussian fit to the zero degree data was chosen as a comparison since the use of symmetric Gaussian functions to simulate detector blur is one type of approach that is currently used in the literature [113]. The Gaussian fit was performed using a modified version of the program *gauss2dfit* in the software package IDL (ITT Visual Information Solutions, Boulder, CO) that forced the widths of the 2D Gaussian in the x and y directions

to be equal.

Qualitatively, from the PRF images in Figure 3.9, we see that the analytical model does a good job of reproducing the MANTIS-generated PRFs at all angles investigated in this study. The analytical PRFs appear to be slightly narrower than the MANTIS PRFs and fail to reproduce a sharp peak (near the top of the PRFs) evident in the MANTIS PRFs. The tendency of the analytical model to appear slightly narrower is most likely due to the fact that the Lorentzian function underestimates the tails of the spread of the optical photons at the exit plane of the scintillator (see Section 3.2.4) for the majority of x-ray absorption depths. This is the case for absorption depths from 0 to about 115 μm, where approximately 86% of 25 keV x rays that contribute to the overall PRF would be absorbed for a 150 μm thick crystal. We would expect this effect to be more dramatic for both the Gaussian and exponential models since they underestimate the tails of the optical photon spread even more than the Lorentzian model. The analytical model fails to reproduce a bright peak evident in the MANTIS PRFs due to the linear approximation made in Section 3.2.4 and shown in Figure 3.7. In that figure, a sharp increase in the width of the Lorentzian distribution is seen between 120 and 140 μm and clearly poorly fit by the linear approximation. As described earlier, the reason for this sharp increase in the MANTIS model is because of the discontinuous transition between the homogeneous layer and the columnar layer. Since the transition is much more gradual in reality, we do not expect this sort of behavior in experimental data (see Section 3.4 as a demonstration).
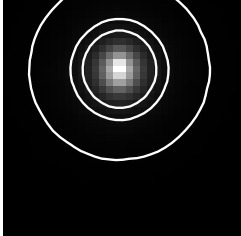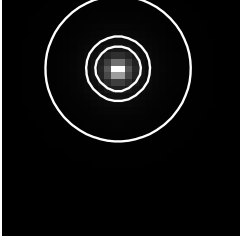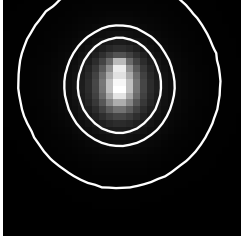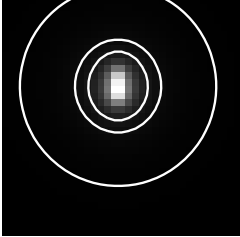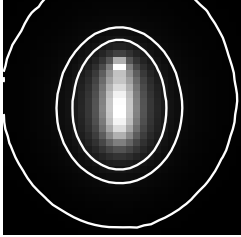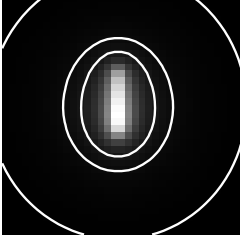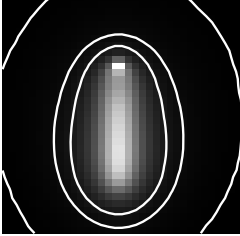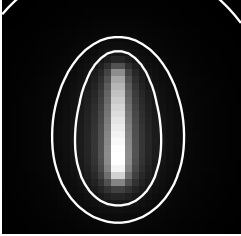
Incidence Angle	MANTIS PRF	Analytical PRF	FOM (MANTIS–Analytical)	FOM (MANTIS–Gauss)
0 degrees			0.1951 ±0.0011	0.6234 ±0.0020
15 degrees			0.1915 ±0.0014	0.9058 ±0.0029
30 degrees			0.2226 ±0.0021	1.491 ±0.012
45 degrees			0.2416 ±0.0074	2.757 ±0.039

Figure 3.9: Comparison of MANTIS-generated PRFs with PRFs from the analytical model after the 2D fit. All PRFs have been generated with a CsI thickness of 150 μm and an x-ray energy of 25 keV. The incident x-ray beam is modeled in MANTIS as an infinitesimal pencil beam. The incidence angle of the x-ray beam is indicated in the left-most column followed by the corresponding MANTIS-generated PRFs, analytical model PRFs, FOMs from the comparison between the MANTIS and analytical PRFs, and, finally, the FOM from the comparison between MANTIS and 2D symmetric Gaussian fits to the normal incidence MANTIS PRF. All PRFs are 0.315 × 0.315 mm with 9 μm pixels. Contours are shown for levels of 0.01, 0.05, and 0.1 times the maximum of the PRF.

For a more quantitative comparison, we can examine the FOM values comparing the MANTIS and analytical PRFs (shown in Figure 3.9). These FOM values range from 0.1951 to 0.2416 for all of the incidence angles investigated. Notably, these FOM values are relatively constant over the different incidence angles, meaning that the analytical model does a good job of reproducing the MANTIS results for all incidence angles. As a comparison, we can examine the FOMs comparing MANTIS and a 2D symmetrical Gaussian fit to the MANTIS PRF at zero degrees. This analysis gives FOMs of 0.6234 ± 0.0020, 0.9058 ± 0.0029, 1.491 ± 0.012, and 2.757 ± 0.039 for 0, 15, 30, and 45 degrees respectively. Comparing with the FOMs for the analytical model, the analytical model outperforms the Gaussian fit for all incidence angles. Interestingly, the analytical model even outperforms the 2D Gaussian fit at an incidence angle of 0 degrees. This is likely due to the fact that a Gaussian function severely underestimates the tails of the PRF at all depths as illustrated in Figure 3.5.

Figure 3.10 is identical to Figure 3.10 except the pre-fit coefficient values are used instead of the post-fit coefficient values. Although the pre-fit coefficient values make more sense in a physical context, they do not fit the MANTIS data as well as the post-fit coefficients. The pre-fit analytical PRFs have FOMs ranging from 0.3026 to 0.4538, whereas the post-fit analytical PRF FOMs range from 0.1951 to 0.2416. This is expected since the fit allows the analytical model to take into account information provided by the more detailed MANTIS simulations.
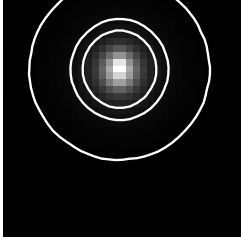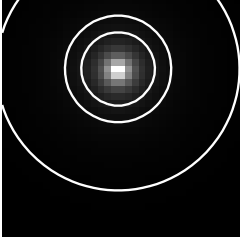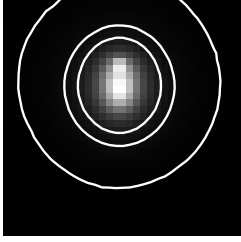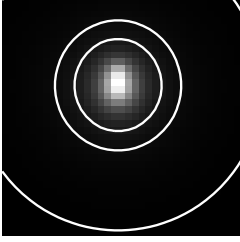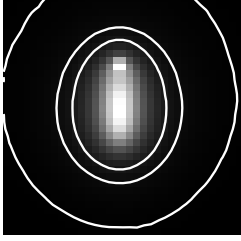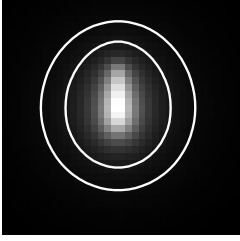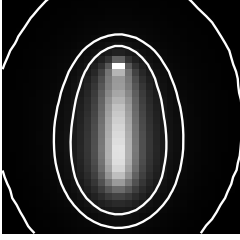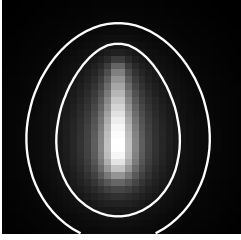
Incidence Angle	MANTIS PRF	Analytical PRF	FOM (MANTIS−Analytical)	FOM (MANTIS−Gauss)
0 degrees			0.3026 ±0.0038	0.6234 ±0.0020
15 degrees			0.3512 ±0.0032	0.9058 ±0.0029
30 degrees			0.4202 ±0.0041	1.491 ±0.012
45 degrees			0.4538 ±0.0108	2.757 ±0.039

Figure 3.10: Comparison of MANTIS-generated PRFs with PRFs from the analytical model before the 2D fit. All PRFs have been generated with a CsI thickness of 150 μm and an x-ray energy of 25 keV. The incident x-ray beam is modeled in MANTIS as an infinitesimal pencil beam. The incidence angle of the x-ray beam is indicated in the left-most column followed by the corresponding MANTIS-generated PRFs, analytical model PRFs, FOMs from the comparison between the MANTIS and analytical PRFs, and, finally, the FOM from the comparison between MANTIS and 2D symmetric Gaussian fits to the normal incidence MANTIS PRF. All PRFs are 0.315 × 0.315 mm with 9 μm pixels. Contours are shown for levels of 0.01, 0.05, and 0.1 times the maximum of the PRF.

3.4 Comparison against experimental results

In a previous study (see Chapter 2), we compared the MANTIS code against experimental PRFs acquired with 40 and 70 kVp x-ray spectra (mean photon energies of 25.6 and 36.5 keV respectively) at 0, 15, 30, and 45 degree incidence angles for four different CsI phosphor screens. In that study, PRFs were generated in MANTIS by including details of the experimental setup in the Monte Carlo simulations. The x-ray focal spot was modeled as a 200 μm diameter circle, the pinhole and a beryllium window were modeled according to the manufacturer's specifications, details of the CsI screen layers and columnar structure were modeled based on scanning electron microscope measurements and manufacturer's specifications, and a fiber optic plate connecting the CsI screen to the optical detector was modeled as a solid plate of glass.

Here, we perform 2D fits of the analytical model to that same MANTIS data and then compare the resultant analytical model to the corresponding experimental data. The objective of this analysis is to evaluate the ability of the analytical model to reproduce experimental results when fit to MANTIS. We did not fit the analytical model directly to the experimental data since this will, in general, not be available. In addition, acquisition of the experimental data is achieved with a pinhole, not an infinitely small incident x-ray beam, which means it is not technically a PRF. We have completed this analysis for one of the screens (denoted Screen 2 in that paper) with a CsI thickness of 170 μm and an aluminum-coated graphite substrate (manufactured by Radiation Monitoring Devices, Inc.). Only the data taken at

40 kVp (25.6 keV mean photon energy) is considered here. For the analytical model, the CsI thickness and x-ray energy values in the final analytical model solution were updated to 170 μm and 25.6 keV respectively. Because of the small change in thickness between 150 and 170 μm, the assumption was made that the functional forms of the individual components of the analytical model were the same as for the 150 μm case. However, the reader is cautioned against using the analytical model for thicknesses other than 150 μm since further research is required to ensure that the functional forms derived in Sections 3.2.1 to 3.2.4 hold for other thicknesses. The results of the comparison between the analytical model and experimental data are shown in Figure 3.11. Note that, as described in Chapter 2, the experimental data was taken with a 30 μm pinhole and a 40 kVp x-ray spectrum, so there is additional blurring as compared with the analytical model which assumes that all the x rays are incident on the CsI crystal at the exact same position and that the incoming x-ray beam is monochromatic. The effect of the finite pinhole was partially compensated for by convolving the analytical model with a 30 μm diameter incident beam before fitting to MANTIS. The MANTIS data did take both the 30 μm pinhole and the 40 kVp x-ray spectrum into account, so this should partially mitigate the limitations of the analytical model.

The FOM values were calculated in the same way described in Section 3.3, but with an ROI that included all the points where the experimental data had a pixel signal-to-noise ratio of 50 or greater. It is important to note that because of the change in the definition of the ROI, which was necessary because of the change
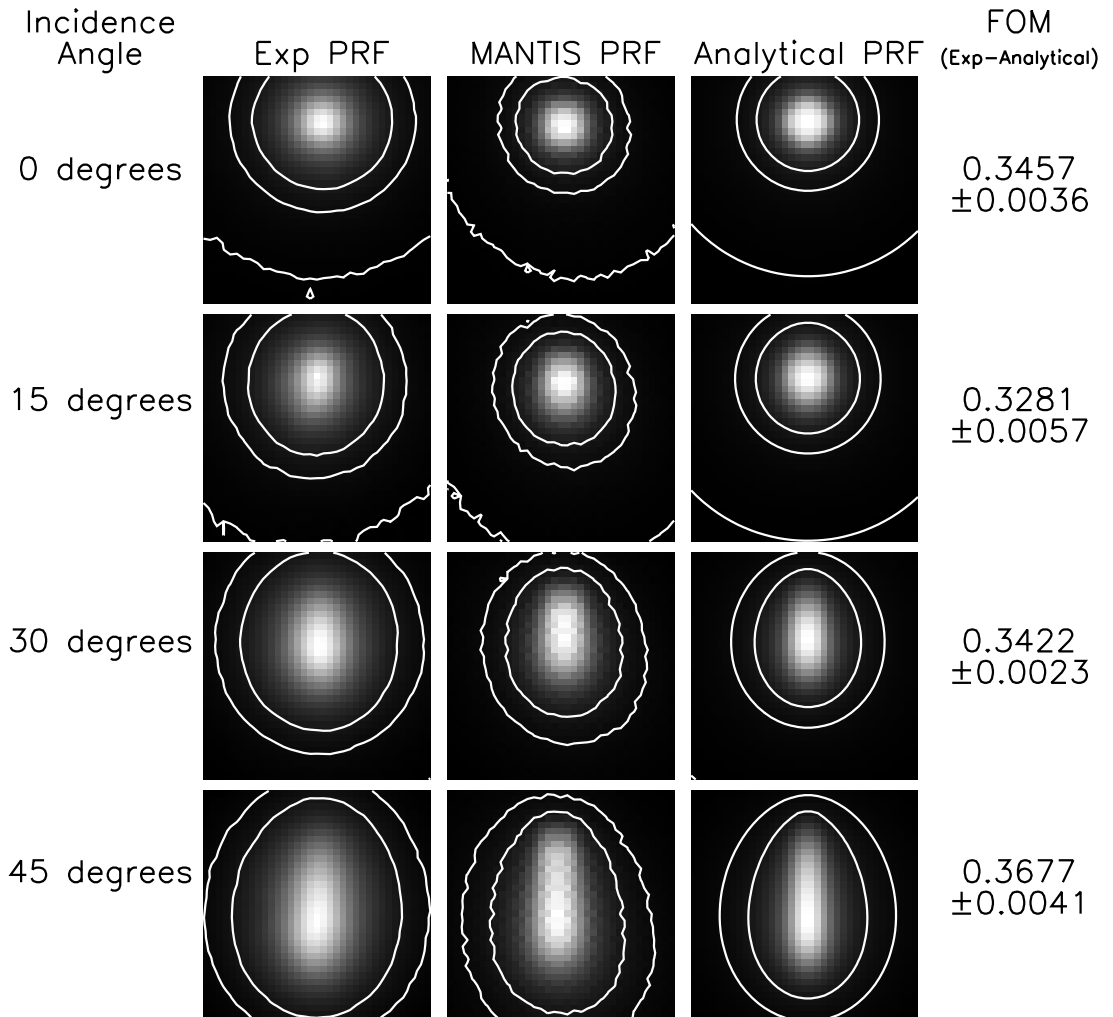
Figure 3.11: Comparison of the analytical model with experimental PRFs. The experimental data were taken at 40 kVp (25.6 keV mean photon energy) with a 170 μm thick CsI scintillator and a 30 μm pinhole. The analytical model was convolved with a 30 μm incident beam profile and then fit to MANTIS data that was generated by taking into account all the details of the actual CsI screen geometry. The MANTIS data was generated with a 100 μm diameter pencil beam incident on a 30 μm pinhole. The incidence angle of the incoming x-ray beam is indicated in the left-most column followed by the corresponding experimental PRFs, MANTIS-generated PRFs, analytical model PRFs, and FOMs from the comparison between the experimental and analytical data. The analytical model was fit to the MANTIS results then a comparison was performed between the analytical model and the experimental data. This procedure was followed as opposed to fitting the analytical model to the experimental data since experimental PRFs will not be available for typical applications. All PRFs are 0.315 × 0.315 mm with 9 μm pixels. Contours are shown for levels of 0.01, 0.05, and 0.1 times the maximum of the PRF.

in the type of data involved, the FOM values in this Section and Section 3.3 are not comparable. In future work, we plan to investigate alternative ways of defining the FOM such that data sets with different noise characteristics can be directly compared. Mean FOM values and their errors were calculated as the mean and standard deviation of FOM values calculated for 11 independent experimental data sets and 11 independent MANTIS-generated PRFs. The FOM values comparing the analytical PRFs with the experimental data are 0.3457 ± 0.0036, 0.3281 ± 0.0057, 0.3422 ± 0.0023, and 0.3677 ± 0.0041 for 0, 15, 30, and 45 degrees respectively. FOMs comparing MANTIS-generated PRFs with experimental PRFs for the exact same screen investigated here were presented in Chapter 2 and are: 0.2944 ± 0.0027, 0.2387 ± 0.0039, 0.2816 ± 0.0025, and 0.2665 ± 0.0032 for 0, 15, 30, and 45 degrees respectively. These FOMs are about the same magnitude as the FOMs comparing the analytical model with the experimental data. Therefore, the analytical model is able to reproduce the experimental data about as good as MANTIS is able to reproduce the experimental data. This is not surprising since the analytical model was able to reproduce MANTIS-generated PRFs well. Figure 3.12 shows the same data from Figure 3.11, but presented in terms of the line spread function (LSF) rather than the full PRF. These LSFs were calculated by summing the PRFs along the direction perpendicular to the incoming x-ray beam and normalizing by the maximum of the summed vector. This direction is shown because it captures the anisotropy of the PRF. From these images we can see that MANTIS tends to produce a width that is too narrow at the peak and too wide at the tails. In addition, the analytical model seems to match MANTIS better than MANTIS matches the experimental

84
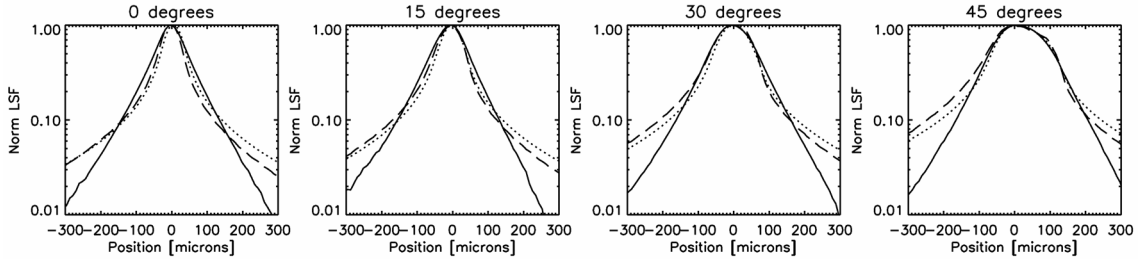
Figure 3.12: Line spread functions calculated from the PRFs presented in Figure 3.11 (25.6 keV, 170 μm thick CsI). The PRFs were summed along the direction perpendicular to the incoming x-ray beam and then normalized by the maximum. Experimental data, MANTIS-generated PRFs, and analytical PRFs are plotted with solid, dashed, and dotted lines respectively. Incidence angles of 0, 15, 30, and 45 degrees are presented from left to right. MANTIS tends to underestimate the width of the peak and overestimate the width of the tails. The analytical model matches MANTIS better than MANTIS matches the experimental data. The slight shift between the analytical model and experimental data in the plot for 45 degrees is due to the cross-correlation algorithm used to match the data. This provides the best match between the analytical and experimental PRFs when the entire PRF is taken into account.

data. The slight shift between the analytical model and experimental data in the plot for 45 degrees is due to the cross-correlation algorithm used to match the data. This provides the best match between the analytical and experimental PRFs when the entire PRF is taken into account and shifts the experimental data to the right because of the asymmetric nature of the analytical PRF. In addition, the difference in width between the analytical and experimental PRFs, shown in Figure 3.11, is deemphasized in the LSFs, shown in Figure 3.12, because the LSF inherently mixes signal from the tails with signal from the peak. In order to improve the match between the experimental data and the analytical model, we plan to extend the analytical model to incorporate polychromatic incoming beams in future versions. Modification of the MANTIS input parameters to improve its match to experimental data may also help the analytical model to better match experimental data.

85

Finally, to demonstrate if the analytical model may be useful for describing the response of thicker screens, we performed the same analysis as above on Screen 3 (450 μm and an aluminum-coated graphite substrate) from Chapter 2. The FOMs comparing the analytical model and experimental data were 0.5847 ± 0.0079, 0.2220 ± 0.0190, 0.3144 ± 0.0363, and 0.2840 ± 0.00625 for angles 0, 15, 30, and 45, respectively. The validation FOM values between MANTIS-generated PRFs and the same experimental data were 0.4380 ± 0.0039, 0.2360 ± 0.0098, 0.2592 ± 0.0064, and 0.2421 ± 0.0079. These initial results suggest that the analytical model described in this paper could provide reasonably accurate predictions of the response of CsI screens with thicknesses comparable to those encountered in other x-ray imaging systems, such as CT. A study is currently underway to investigate in detail the application of the model to thicker screens.

3.5   Conclusion

In this study, we have developed a detailed, deterministic analytical model to approximate MANTIS (Monte Carlo) generated PRFs of CsI scintillator screens for indirect x-ray detectors of 3D breast imaging systems. We have demonstrated, using quantitative FOMs, that the analytical model is able to reproduce MANTIS-generated PRFs well for a range of incidence angles and much better than a simple 2D symmetric Gaussian fit to the zero-angle MANTIS data. In addition, comparisons of the analytical model against experimental data show that the analytical model is able to reproduce experimental data about as well as MANTIS. Therefore, the ana-

lytical model produces PRFs that are comparable to those generated by MANTIS and that capture the anisotropy effects seen at large incidence angles. Most importantly, because the analytical model is a (relatively) simple mathematical expression, it can generate a PRF in only 0.1 sec on a single CPU, which is less than one millionth the computational time required by MANTIS to produce a comparable (but still noisy) PRF (200 hours on a single CPU). The ability of the analytical model to generate PRFs in such a short time will allow for inclusion of the detailed PRF structure that has been demonstrated with MANTIS in rigorous optimization algorithms and rapid 3D image reconstructions. This has the potential to improve lesion detection in future 3D breast imaging systems by including accurate detector blur functions in optimization of the system geometry. In addition, more detailed knowledge of the forward problem with respect to detector performance will allow for reconstructed images that are a more faithful representation of the true object.

The current work has investigated a limited set of parameters (25 keV x rays, 150 μm thick CsI, and incidence angles of 0, 15, 30, and 45 degrees) and has demonstrated generation of only four individual PRFs. In future studies, we will extend this work by performing fits of the analytical model to MANTIS-generated PRFs for a larger, but still discrete, set of parameters (x-ray energies, CsI crystal thicknesses, and incidence angles). In addition, we will develop relationships that allow for generation of the appropriate analytical model coefficient values over the entire range of investigated values so that model PRFs can be easily generated for optimization and reconstruction algorithms. The current model can also be used to derive noise transfer properties of indirect imaging detectors.

87

Chapter 4

MRI properties of the anthropomorphic, dual-modality phantom

4.1 Overview

Dynamic[1] contrast-enhanced (DCE) MRI with Gd-DTPA has been shown to be useful in screening women at high-risk of breast cancer as well as in evaluating the extent of disease [13, 39]. In 2007, the American Cancer Society released guidelines recommending screening MRI as an adjunct to x-ray mammography for women with a 20-25% lifetime risk of developing breast cancer [11] and DCE-MRI has been used increasingly in the clinic [40, 41]. Despite recent advances, many issues remain to be fully addressed in DCE-MRI. Although DCE-MRI demonstrates high sensitivity, it has a well-documented low and variable specificity (26-97%) [17, 23, 24]. In addition, there has been debate over a possible link between increased MR use in breast cancer imaging and an increase in the number of more extensive surgeries and mastectomies being performed at some institutions [25, 26, 27, 28, 29, 30, 31, 42, 43, 44].

In response to these issues, recent standardization efforts in the breast MR community have resulted in a breast MR lexicon [45, 46] and a set of standardized quantities and symbols for kinetic analysis of Gd-DTPA tracer washout [47]. Review papers have discussed the variety of protocols used and given general recommendations regarding which protocol to use for a given clinical scenario [39, 48].

---

[1]Work in this chapter tentatively accepted to Medical Physics [38].

However, standards for specific breast MRI acquisition protocols are still needed. In particular, quantitative assessment of MR protocols and their efficacy for different clinical situations has not yet been adequately addressed.

To perform quantitative comparisons of imaging protocols in terms of lesion detection and characterization, a phantom that mimics anatomical tissue structure in addition to contrast properties is required. The importance of realistic phantom structure in the evaluation of imaging systems for the purpose of abnormality detection was demonstrated in a study by He *et al.*[49], in which both phantom and patient data were used to perform reader studies evaluating compensation methods for myocardial SPECT image reconstruction algorithms. They found that phantoms with more complicated, realistic image structures resulted in performance measures for defect detection that more closely matched results derived from patient data than studies with more simplistic phantoms. The optimal reconstruction parameters derived from the more realistic phantoms were significantly different than those derived from more simplistic phantoms.

In the context of breast imaging, the importance of realistic phantoms was demonstrated in a study investigating the utility of different imaging modalities to evaluate silicone breast implants [50]. The authors reported how only a more realistic and complex phantom revealed important differences between the evaluated imaging modalities.

A small number of breast MR phantoms have already been described in the literature [51, 52]. Mazzara *et al.*[51] and Liney, Tozer, and Turnbull [52] both describe phantoms where a homogeneous layer of adipose-mimicking material (Crisco

or lard) surrounds an interior homogeneous region of glandular-mimicking material (polysaccharide material TX-151 or a commercial jelly product) in a cylindrical container. In the Mazzara *et al.*[51] phantom a version with an implant was also created. A lesion was included in the Liney, Tozer, and Turnbull [52] phantom as a capsule filled with Gd-DTPA-doped water. In both cases the T_1 and T_2 relaxation times of the materials were measured and found to be in good agreement with breast tissue values. In addition, the American College of Radiology (ACR) phantom for accreditation (http://www.acr.org/accreditation/mri.aspx) is available for the quantitative evaluation of image quality parameters such as resolution, signal to noise ratio, and the presence of artifacts.

While existing phantoms do address some needs of the imaging community, there are currently no phantoms available that reproduce the appearance of and variability in the anatomical structure seen in human images. Similarly, no phantoms are available with well-characterized lesions and variable tissue structure. Such a phantom would allow researchers to investigate how imaging technique parameters interact with anatomically relevant structure to affect the clinicians end goal, which, in the case of breast cancer imaging, is lesion detection and characterization. Therefore, for the quantitative comparison of diagnostic efficacy and for protocol selection, the appearance and variability of structures in the phantom and its similarity with patient data become critical aspects of the phantom.

In this study, we describe a physical, tissue-mimicking phantom for the quantitative assessment of breast MRI protocols in terms of lesion detection and characterization in the presence of complex, human-like, anatomical structures. Important

requirements for such a phantom include T_1 and T_2 relaxation parameters similar to those in adipose and glandular human breast tissues, a random phantom structure that mimics anatomical structures in patients, the ability to actively suppress the signal from the adipose-simulating component in the phantom, and a realistic enhancing lesion. In this study, we present a phantom that addresses all of the above properties.

4.2 Materials and methods

4.2.1 Phantom construction

The phantom was constructed using refined lard to simulate adipose tissue and coagulated, fresh egg whites to simulate fibroglandular tissue. The lard (Goya Foods, Secaucus, New Jersey or Marquez Brothers International, Inc., San Jose, California) and fresh eggs (Davidsons Safest Choice Pasteurized Shell Eggs, National Pasteurized Eggs, Inc., Lansing, Illinois) were both purchased from local supermarkets.

Lard was chosen to simulate adipose tissue since it has a similar composition, is very stable, and is readily available. Human white adipose tissue consists mostly of lipids in the form of triglycerides [53]. Myristic, palmitic, palmitoleic, stearic, oleic, and linoleic fatty acids make up more than 90% of the triglyceride component [53]. Lard is composed entirely of lipids, 97.9% of which are in the form of triglycerides [54], where the same six fatty acids make up over 90% of the total lipid content [55]. The shelf-life for lard is indicated by the manufacturer to be at least a year and a

91

half with no refrigeration necessary.

Egg whites were chosen to simulate glandular tissue since they have a similar composition, unique functional properties that aid in structure formation, and are also readily available. In addition to adipose tissue, the human female breast is also made up of ducts, lobules, and the associated fibrous stromal compartment [56, 57] that make up the so-called glandular portion of the breast. Both ducts and lobules consist of epithelial and myoepithelial cells surrounded by a basement membrane that is made up of primarily laminin and type IV collagen proteins [58, 59]. The main extracellular matrix component of the interstitial stromal compartment is type I collagen protein [59, 60]. Therefore, a large part of the glandular tissue is made up of proteins.

In addition, we know that a significant fraction of glandular breast tissue is made up of water. One study showed that normal patient glandular breast tissue has a water content of 41-76% by weight [61]. Therefore, a glandular-mimicking phantom material should be high in both water and protein content. The inclusion of cells would be not only expensive, but also unrealistically unstable. Egg whites provide a good first order match to human glandular tissue makeup. Egg whites are made up of mostly water (87.6%) and proteins (10.9%) [55]. The major proteins are ovalbumin, ovotransferrin, ovomucoid, ovoglobulin G2, ovoglobulin G3, and lysozyme, which make up about 91.9% of the total protein content of egg whites [62]. While the types of protein in egg whites and human breast tissue differ, the elemental composition of different proteins is almost indistinguishable [63]. In addition, all proteins are made up of amino acids, which all bind H in similar

ways. Therefore, we expect that the MRI signal of the proteins in egg whites would be similar to those in human breast tissue. In addition to being readily available, egg whites also have several functional properties that make them ideal for forming structures with no intervening septum. They coagulate irreversibly after heating [64] and do not dissolve into the surrounding material. While the shelf-life of egg whites is markedly less than refined lard, we will heat the egg whites, store them in an air-tight container, and mix them with a preservative to improve the shelf-life as much as possible. The true shelf-life of both phantom components will be measured as described in the next subsection.

A custom, air-tight plastic jar was developed to contain the phantom materials and simulate the shape of the human breast. The jar shape was defined by a half-sphere combined with a cylindrical portion, where the total internal volume was fixed to a typical breast volume of 425 ml [65]. The lid attaches to the jar body via a ring of 24 screws through a gasketed connection and has two fill ports that are sealed with teflon tape-coated screw plugs. The half-sphere jar shape was chosen to approximate the shape of the majority of breast patients based on visual inspection of clinical breast MRI images and ease of fabrication. Although this approximation roughly simulates the shape of many patients, there is certainly a large variation in patient breast shape including conical shapes and shapes distorted due to the contact of the breast with the coil. Such differences can have important implications on effective breast shimming [66]. It would be possible to modify the jar shape of the phantom to mimic some of these other shapes or even to use segmented patient images to produce irregular jar shapes, but this would not affect the T1 and T_2 of

the phantom material and is outside of the scope of the current study.

To fill the phantom jar, a preservative (0.2% w/v Dowicil 75, The Dow Chemical Company, Midland, Michigan) was added to raw egg whites prior to pouring into melted lard, and heating for 30 s while stirring at a constant rotational velocity. The lard was heated until it reached either 100^oC or 110^oC and stirred at a constant velocity of either 125 or 350 rpm. These different lard temperatures and stirring velocities were used to create a set of phantoms with different tissue structures in an attempt to mimic the type of variation seen in patient data. Air bubbles were removed by placing the phantom in a vacuum for 20 minutes. The mixture was then cooled at room temperature in the sealed jar and rotated once during cooling to help redistribute the egg whites in the lard. This rotation helps create a layer of lard around the edges of the jar. The phantoms were constructed with a density of approximately 24% glandular-mimicking material by volume. This breast density is similar to densities measured on patient populations using MRI. A study that estimated breast density using MRI in a high-risk cohort of 35 patients found breast densities ranging from 2 to 71.4% with a mean of 28% [67]. In the future, the density of the phantom could be varied to match the full range of densities seen in patient data by simply increasing the amount of egg whites.

4.2.2 T_1 and T_2 relaxation parameter measurements

For estimation of T1 and T_2 values, inversion recovery (IR) and spin-echo (SE) sequences were used respectively. All scans were performed in a Siemens Magnetom

1.5 T clinical scanner using an extremity coil[2]. The scan parameters were TR=25 s, resolution=2.5 mm x 2.5 mm x 2.5 mm, 5 slices separated by 7.5 mm each, TI=[22, 35, 45, 75, 100, 150, 200, 250, 400, 500, 600, 900, 1000, 1500, 2500, 4500] ms for the IR sequence, and TE=[15, 20, 25, 30, 35, 40, 50, 70, 75, 95, 100, 120, 150, 200, 300] ms for the SE sequence.

T_1 and T_2 relaxation times of the lard and egg compartments were estimated from reconstructed magnitude images using maximum-likelihood estimation (MLE) with a Rician data model. The maximization of the likelihood was implemented using a limited-memory Broyden-Fletcher-Goldfarb-Shanno (L-BFGS) method with bounds [68] in the R programming language. The Gaussian noise variance, σ^2, was estimated using the MLE equation for estimation from a background region in a magnitude data set [69]. For our data, two rectangular bands of 11 x 47 pixels on either side of the imaged sample, located at the edge of the image, were designated as background voxels and used in the above calculation. The large dimension of the background regions covered the full image field-of-view and the small dimension was chosen to select enough pixels to reasonably sample the noise probability distribution while staying as far away from the object as possible.

For lard, relaxation values were estimated using a lard-filled tube, assuming mono-exponential signal behavior. Formulas for MLE of mono-exponential T_1 and T_2 relaxation times have been presented in the literature [70, 71]. We used the T_2 equations as previously presented and expanded the mono-exponential T_1 signal equation to include an additional parameter to correct for imperfect inversion pulses

---

[2]With the help of Jacco A. de Zwart

since this is known to significantly affect T_1 measurements even on 1.5T systems [72, 73]. All coefficients for fits to lard data were forced to be positive. The mean and standard deviation of estimated relaxation values for all voxels within a hand-selected circular region-of-interest (ROI) were taken as the estimated relaxation value and its error. The number of voxels included in the ROI was typically 145, which represents the number of voxels included in the user-selected circular ROI across each of the 5 imaged slices. The circular ROIs were selected to include as much of the object as possible, while avoiding pixels on the edge of the object that had partial volume mixing with the surrounding air.

The relaxation values of the egg component were calculated on the phantom itself since the relaxation values of egg are known to vary with preparation technique [74]. A double-exponential signal equation was used to fit the data with the T_1 and T_2 values of lard fixed to those estimated above; the amounts of egg and lard, the inversion pulse correction, and the T_1 and T_2 values of egg are free parameters for each voxel. All free parameters were forced to be positive during the fitting except for the T_1 value of egg, which was restricted to values between 500 and 5000 ms. The reported relaxation values and their errors were calculated as the mean and standard deviation weighted by the egg fraction for all voxels, within a hand-selected, circular ROI, with an egg fraction of at least 50% and a proton density of at least 50% of the maximum value in the sample (on average about 480). The circular ROIs were selected to include as much of the object as possible, while avoiding pixels on the edge of the object that had partial volume mixing with the surrounding air.

The above process was repeated for three different phantoms manufactured

using different construction parameters (lard heating temperatures and constant rotational velocities) to ensure that variations in the production method did not cause variations in the relaxation values outside of the human range.

The estimated phantom relaxation values were compared with published human data. All published studies found where both T_1 and T_2 values were calculated separately for both adipose and glandular breast tissues on a 1.5 T magnet were included in our analysis [75, 76, 77, 78]. Error bars were taken directly from the respective values reported in the publications.

The stability of the relaxation values over time was measured by repeating the above process approximately every other week over a period of 9 months. During this time the phantom was stored at room temperature.

4.2.3   Comparison of image structure

The phantoms structure was quantitatively compared with patient data using covariance matrices. The covariance matrix measures how each pixel in the image co-varies on average with every other pixel, given a population of such images (from either phantoms or patients) [79]. The full covariance matrix of a vector (or image) **g** with M elements (equal to N^2 for an image or ROI with $N \times N$ pixels) will be an $M \times M$ matrix with elements given by

$$K_{ij} = \left\langle \left(g_i - \bar{g}_i\right)\left(g_j - \bar{g}_j\right)^*\right\rangle, \qquad (4.1)$$

where the overbar indicates an average and the $*$ indicates complex conjugation. If

g_i and g_j are statistically independent and $i \neq j$, then $K_{ij} = 0$. If $i = j$, then K_{jj} is equal to the variance of g_j. Since **g** is a random vector, we must average over many instances of **g** in order to get a good estimate of K.

Since we have a limited number of images available relative to the number of elements that must be computed for a full covariance matrix, we have averaged the covariance matrix over all positions within an image ROI, therefore assuming wide-sense stationarity within that ROI [79] and reducing the variance of the estimate of K at the expense of position-dependent information. We will refer to this matrix as the stationary covariance matrix. It represents the average direction-dependent correlation strength over all positions in the ROI and is an estimate of the texture in the images to second order. The stationary covariance matrix has a size of $2N - 1 \times 2N - 1$ and is given by

$$K_{pq}^{stationary} = \left\langle K_{i(i+p+qN)} \right\rangle_{i \in [(m+nN) \in S]}, \tag{4.2}$$

where p and q are offset indices (both $\in [(N-1), ..., (N-1)]$) in the x and y directions, respectively. The physical meaning of p and q is that they are relative offset values. So, $K_{pq}^{stationary}$ is the element of $K^{stationary}$ that holds the average covariance over all pixel pairs in the ROI that are separated by p pixels in the x direction and q pixels in the y direction. Another way to state this is that the covariance element $K_{pq}^{stationary}$ describes the correlation between any pixel in the ROI and its neighbor p pixels to the right and q pixels up. The element $K_{00}^{stationary}$ is at the center of the matrix. The two-dimensional indices m and n both run from

0 to $N-1$ over the two-dimensional ROI in the x and y directions, respectively. The one-dimensional index i is simply a one-dimensional version of the indices m and n that runs over every pixel in the ROI ($\in [0, ..., N2-1]$) and is equal to m+nN. The average over the elements of the full covariance matrix only includes elements for which a (p,q) offset ROI pixel exists, denoted by the set S. Therefore, the number of samples that contribute to the calculation of the element $K_{pq}^{stationary}$ of the stationary covariance matrix varies with the exact p,q indices and is given by $(N-|p|)(N-|q|)$. We can see from this equation that stationary covariance elements describing correlations with more distant pixels pairs (large p and q values) have fewer samples. Also note that both the full and stationary covariance matrices are symmetric, so $K_{ij} = K_{ji}$ and $K_{ij}^{stationary} = K_{ji}^{stationary}$.

To illustrate the calculation of the stationary covariance matrix, let us take the example of a 3×3 ROI ($N = 3$). In this case, $m, n \in [0, 1, 2]$, $i \in [0, 1, 2, 3, 4, 5, 6, 7, 8]$, and $p, q \in [-2, -1, 0, 1, 2]$. For the $(p,q) = (1,2)$ element of the stationary covariance matrix, the average takes place only over $i \in [0, 1]$ because the other i index values correspond to ROI pixels that do not have counterparts that are 1 pixel to the right and 2 pixels up. The resultant stationary covariance matrix element is equal to

$$K_{12}^{stationary} = \frac{1}{2}\left(K_{07} + K_{18}\right) \tag{4.3}$$

and has 2 samples. Likewise, the $(p,q) = (1,-1)$ element of the stationary covariance matrix is equal to

99

$$K_{1-2}^{stationary} = \frac{1}{4}\left(K_{31} + K_{42} + K_{64} + K_{75}\right) \tag{4.4}$$

and has 4 samples.

For each phantom or patient data set, the largest square ROI was selected by-hand which still contained only breast tissue. The ROI size varied with breast size for patient data (between 35×35 and 150×150 voxels), but stayed constant for phantom data (70×70 voxels). This ROI was applied to a set of slices (between 26 and 92 slices per patient depending on breast size and 61 slices per phantom) of the left breast where enough breast tissue was present to fill the chosen ROI.

Multiple slices were included in the stationary covariance matrix calculation by concatenating all ROIs from all slices into a single **g** vector. This provided a single, in-plane, stationary covariance matrix for each patient or phantom, which we will refer to as a patient- or phantom-specific stationary covariance matrix. This matrix was also normalized by the average voxel variance (the central pixel of the stationary covariance matrix) to highlight the relative correlation fall-off with spatial position.

An overall stationary covariance matrix for the entire patient or phantom population was then calculated by first converting all patient-specific stationary covariance matrices to the same spatial scale (0.625 mm/voxel) using a cubic convolution interpolation with an interpolation parameter of -0.5 [80] if necessary. The difference between the original and interpolated covariance matrices was negligible. Finally, all of the resultant matrices were averaged. Error bars on the overall sta-

tionary covariance matrix were estimated by calculating the standard deviation of the patient-specific stationary covariance matrices values at each offset position.

To understand whether the difference among patient-specific stationary covariance matrices was due to instrumentation error or anatomical variations, simulated ROIs were created with only Rician noise. In all cases, the noise variance was set to one since the final covariance is normalized by its maximum value, which is equivalent to the average pixel variance. Simulated ROIs were chosen to have a conservative size of 35×35 voxels, which is equal to the smallest ROI used for the covariance calculations on the patient data. Sets of between 5 and 95 simulated ROIs were created to bracket the range of the number of slices selected in the patient data. The root mean squared (RMS) variation in the simulated, Rician-noise only, patient-specific stationary covariance estimate was then calculated for 5 different offsets (4-20 mm) by averaging over all offsets whose absolute values $\left(\sqrt{p^2 + q^2}\right)$ were within 4 mm of the specified offset. The RMS variation was calculated as a function of the number of ROIs used in the covariance estimation (corresponding to the number of patient slices). This process was repeated on eleven independent realizations to improve the RMS estimates and compare with the variation in the patient-specific stationary covariance matrices.

Coded patient data were taken from the National Cancer Institute's (NCI) Clinical Genetics Branch's Breast Imaging Study data archive[3]. Use of the data was authorized under appropriate IRB approval from both the NCI and FDA. In the study, a total of 194 high-risk patients were imaged using various MR imaging

---

[3]Provided by Jennifer Loud and Mark H. Greene

protocols and scanner types. Patients were enrolled between June 2002 and February 2007 and included in the study if they were between 25 and 56 years of age and considered at high genetic risk of developing breast cancer. See Loud *et al.*[81] for additional study details.

Seventy-seven patients with MRI data collected on a 1.5T Philips machine with a 7-channel, dedicated breast coil and with the same pre-contrast imaging sequence, were selected for additional analysis. Thirteen were excluded because of the presence of an implant or diagnosis of breast cancer before or during the course of the NCI breast imaging study. Sixty-four patients remained for the final analysis. Pre-contrast, T1-weighted, gradient-echo, fat-suppressed images were available for each patient with an in-plane resolution ranging from 0.586 to 0.664 mm and a slice thickness ranging from 1.9 to 2.3 mm. Twenty phantoms were fabricated and imaged using the same scanner type, breast coil, and imaging sequence for comparison with the patient data[4].

4.2.4 Enhancing lesion

An enhancing, mass-like lesion was designed to be included in the phantom. We have designed and manufactured two simulated lesions using stereolithography to simulate round and lobular morphologies. The simulated lesions consist of hollow plastic molds with 0.6 mm thick walls and can be filled with a Gadolinium-doped water solution. Neither of the plastic molds have any internal structure. The lesion with the round morphology is a 1 cm internal diameter sphere with an internal

---

[4]With the help of Riham H. El Khouli

volume of 523.6 mm^3. The lobular lesion is a 1 cm internal diameter sphere with three additional lobulations and has an internal volume of 563.2 mm^3. The stereolithography printer resolution was 0.0508 x 0.0508 x 0.1016 mm for these parts. An inner diameter of 1 cm was chosen for the lesions since it is small enough to be a challenge to detect, but large enough to be able to apply morphological descriptors during lesion characterization. The size of the lesion could easily be varied.

These lesions are suspended in the phantom via small tubes that attach to the lid of the phantom jar and are added into the phantom itself when the jar is sealed and allowed to cool. Once the phantom is completely cooled and the lard and egg whites have solidified, the lesion is filled with 4.5 mM GdCl$_3$ (anhydrous gadolinium chloride, 99.99%, Sigma-Aldrich, St. Louis, MO) in deionized water. This concentration of gadolinium was chosen to be similar to that of patients at the peak of a typical gadolinium contrast agent washout curve. Note that the concentration of gadolinium in the lesion is a fixed value in the current study. In future studies, we plan to extend this lesion model to include temporally dynamic behavior.

We obtained chemically-selective fat-suppressed, 3D gradient-echo MRI images of phantoms with each of the two lesion types using a Siemens Magnetom 1.5 T clinical scanner with an extremity coil. The scan parameters were: resolution = 0.75 mm×0.75 mm×0.75 mm, matrix size = 192×192×72, TR = 3.86 ms, TE = 1.36 ms, flip angle = 10 degrees.
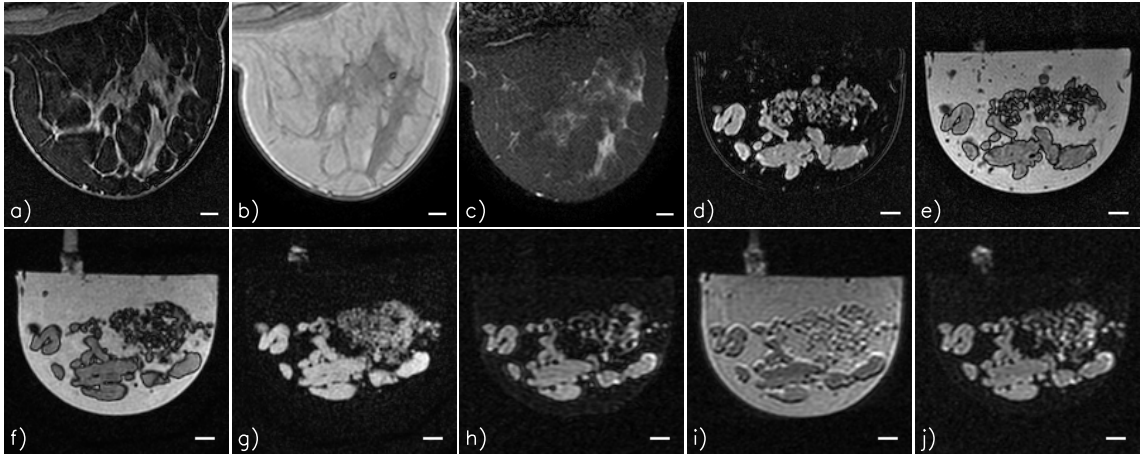
Figure 4.1: Example patient and phantom images. (top row) acquired with a 1.5 T Philips scanner and a dedicated breast coil (bottom row) acquired with a 1.5 T General Electric scanner and a dedicated breast coil. a) patient, T_1-weighted, fat suppressed, b) patient T_1-weighted, no fat suppression, c) patient, T_2 SPAIR (spectral adiabatic inversion recovery), fat suppressed, d) phantom, T_1-weighted, fat suppressed, e) phantom, T_1-weighted, no fat suppression, f) phantom, T_1-weighted, no fat suppression g) phantom, T_1-weighted, fat suppressed h) phantom, STIR (short T_1 inversion recovery), fat suppressed, i) phantom, T_2-weighted, no fat suppression j) phantom, T_2-weighted, fat suppressed. All scale bars are 10 mm.

4.3   Results

Figure 4.1 shows example patient and phantom images acquired with clinical systems. T_1- and T_2-weighted images of the phantom are shown, acquired using standard clinical breast protocols from two different institutions with two different clinical scanners (1.5 T Philips and 1.5 T General Electric both with dedicated breast coils).

T_1- and T_2-weighted images of the phantom are shown with and without fat suppression for two different clinical scanners (1.5 T Philips and 1.5 T General Electric) with dedicated breast coils. Our phantom provides a breast shape and internal tissue structure that is much improved over currently available phantoms.

104

Figure 4.2 shows the comparison of phantom T_1 and T_2 relaxation parameters with corresponding published human values. Values for three different phantoms with different construction parameters are shown. Phantom relaxation values fall within 2 times the standard error of the human data. The match between the human and phantom data is particularly good for T_1 values, which are more relevant when evaluating DCE-MRI since the images are T_1-weighted. Results of the stability analysis are shown in Figure 4.3. Over a 9 month period the T_1 and T_2 values are stable to within 8% and 15%, respectively, for both lard and egg whites. The data indicate that the phantom materials may be stable over an even longer time period since the values have not yet strongly deviated from their values at production time. We will continue to monitor the stability until the values change significantly. In Mazzara *et al.*[51], when their phantom was stored at room temperature for 6 months they stated that no noticeable degradation was seen and the T_1 and T_2 values had less than 10% random variations. For the phantom presented in Liney, Tozer, and Turnbull [52], data evaluating the shelf-life was not presented and the shelf-life was stated as being several months when refrigerated. Therefore, our phantom performs at least as well as currently available breast phantoms in terms of stability.

Figure 4.4 shows example phantom and patient ROIs. A visual comparison between these ROIs indicates that the phantom has a random structure that resembles the complicated patient data image structure. We observe that the patient data appear to have a directional preference in the anterior-posterior direction, whereas the phantom is more isotropic. Furthermore, the fat suppression in the phantom

105
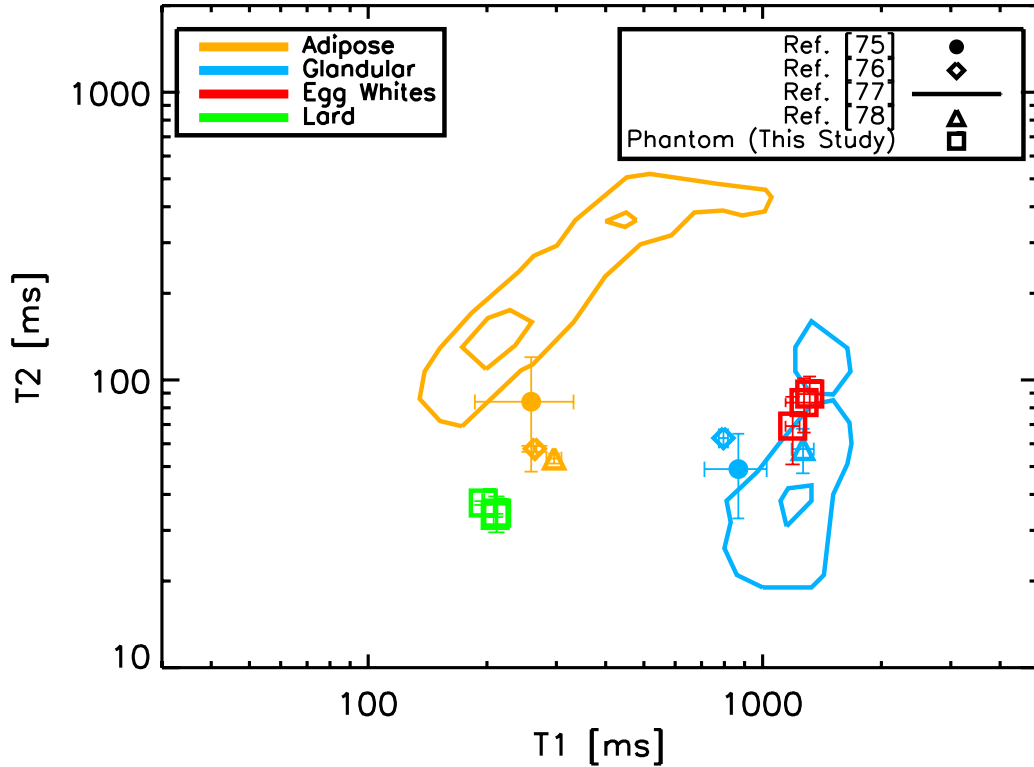
Figure 4.2: Comparison of phantom T1 and T_2 values with human data from the literature. Error bars are one standard error. The lines plotted for the Graham *et al.*[53] study indicate contours that include a calculated 12.5% and 87.5% probability of their measured tissues. The T_1 and T_2 values of the phantom materials fall within two standard errors of the human data for both the adipose- and fibroglandular-mimicking compartments. Data points for the phantom materials were measured on three different phantoms constructed using different lard temperatures and stirring velocities. The phantom T_1 values are a better match to human data than the T_2 values and are the primary determinants of image contrast for DCE-MRI studies.
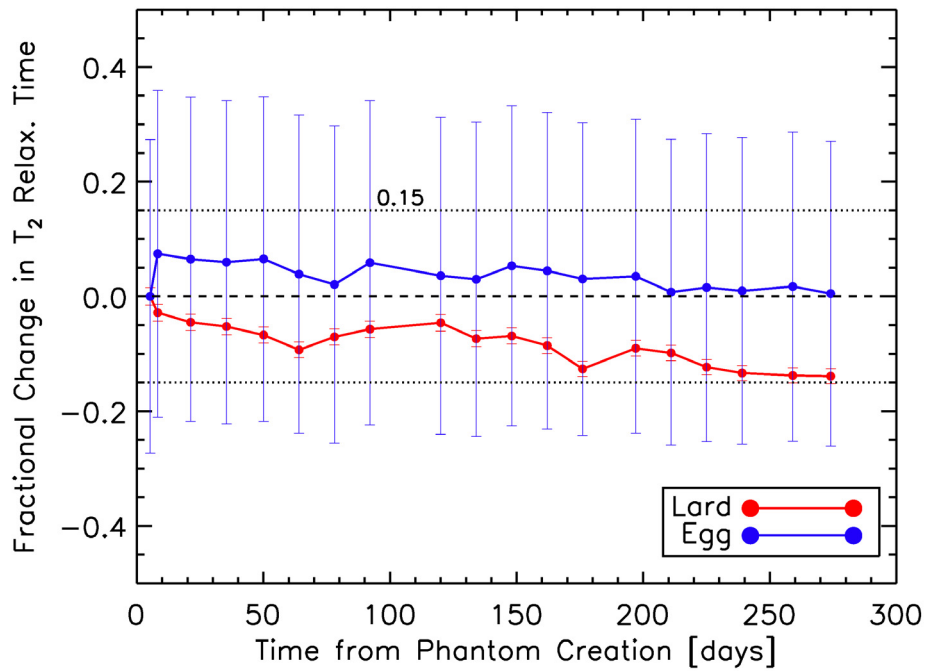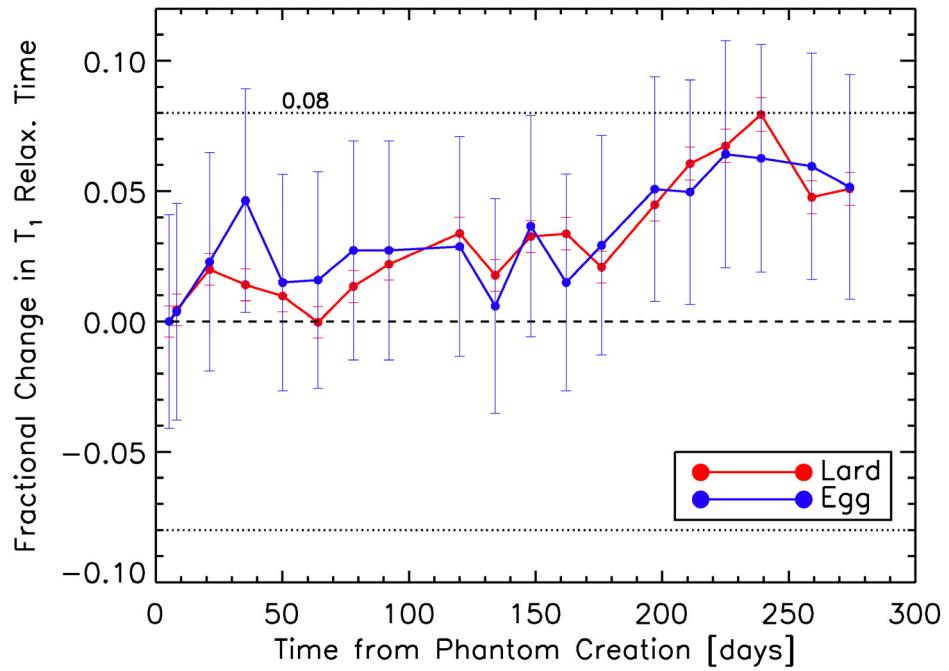
Figure 4.3: Fractional change in T_1 (top) and T_2 (bottom) relaxation times of lard and egg whites as a function of time since phantom production date. All data points have been normalized by the relaxation value on the phantom production date. T_1 and T_2 relaxation values of both lard and egg are stable to within 8% and 15%, respectively, over a period of 9 months. Errors bars are the standard deviation over all voxels included in the computation for a single data set.

107
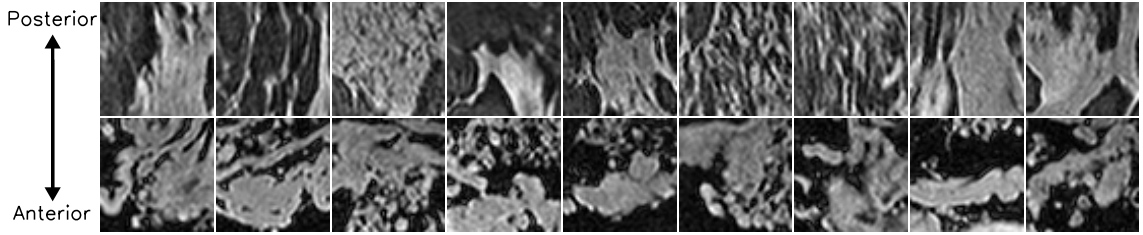
Figure 4.4: Example ROIs (cropped to 3.5 cm x 3.5 cm) selected from the patient (top row) and phantom (bottom row) fat-suppressed, T_1-weighted data. The phantom has a statistically random image texture that is similar to the patient data. Structures in the patient data appear to be more anisotropic than those in the phantom data and tend to elongate along the anterior-posterior direction. The phantom data also appears to have slightly better fat-suppression than the patient data.

images appears to be slightly improved as compared to that of patient data. This may be due to the fact that there is no torso attached to the phantoms, resulting in improved shimming of the phantom, or that the spectral shape of the fat signature in the phantom may be less complicated than that of patients. There may also be more homogeneity of the material types within a voxel in the phantom than in the patient data, resulting in the appearance of better fat suppression.

Figures 4.5 and 4.6 compare patient and phantom covariance matrices. Figure 4.5 shows images of the patient and phantom overall stationary covariance matrices, while Figure 4.6 shows horizontal and vertical cuts through those matrices. Our data suggest that the covariance length of the patient and phantom images is similar along the anterior-posterior direction. In the right-left direction, they differ by about two standard error bars, with the phantom images having a larger correlation length than the patient data. In general, the phantom data is more isotropic than that of the patient, which tends to have structures that elongate along the anterior-posterior direction. Interestingly, the error bars of the patient and phan-

108
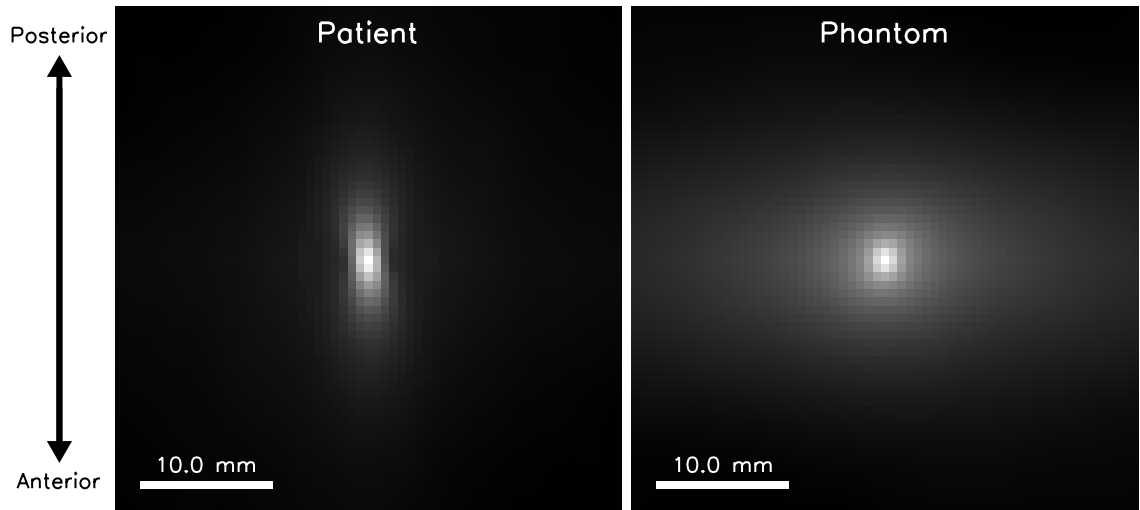
Figure 4.5: Overall stationary covariance matrices for the patient and phantom data sets. The matrices are scaled to have the same intensity at their peak. The phantom and patient overall stationary covariance matrices have a similar covariance length in the anterior-posterior direction. However, the phantom has a larger covariance length than the patient in the right-left direction.

tom data are similar, which indicates a similar range of variability among the two populations.

Figure 4.7 shows the results of simulations run to estimate the amount of instrumentation error included in the error bars in Figure 4.6. RMS variations in the stationary covariance matrix estimations are plotted as a function of the number of ROIs used in the estimate. The ROIs were simulated images created with only Rician noise. Results for five different offset distances are shown. For 26 to 92 ROIs, the magnitude of the RMS instrumentation error in the stationary covariance ranges from 0.003 to 0.020 depending on the offset distance and the number of ROIs. The corresponding error bars in Figure 4.6 range from 0.053 to 0.096 for the same set of offset distances. The fact that the RMS instrumentation errors are less than the size of the error bars in Figure 4.6 indicates that these error bars represent mostly

109
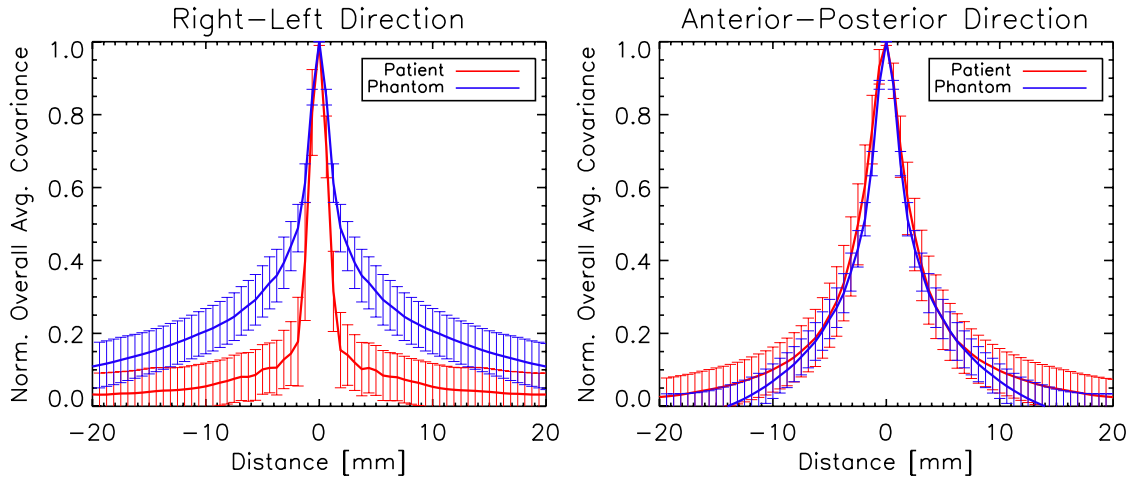
Figure 4.6: Cuts through the patient and phantom overall stationary covariance matrices (shown in Figure 4.6) in the right-left and anterior-posterior directions. The patient and phantom overall stationary covariance matrices are the same to within their error bars along the anterior-posterior direction, but differ in the right-left direction. Error bars are the standard deviation of the individual patient- (n=64) and phantom-specific (n=20) stationary covariance matrices at each distance.

anatomical variation.

Images of the lesions before inclusion in the phantom as well as fat-suppressed, T_1-weighted, gradient-echo MRI images of two phantoms with the two different simulated lesion types are shown in Figure 4.8. We are able to produce complex lesion morphologies and to fill those with a gadolinium-doped water solution whose concentration can be varied by the user to investigate different contrast agent doses. With the addition of the enhancing lesion, the phantom can be used to study the effect of image protocol parameters on lesion detection and characterization.

4.4 Discussion

We have described a breast MR phantom, developed for quantitative evaluation of breast MRI techniques, which mimics breast tissue properties including
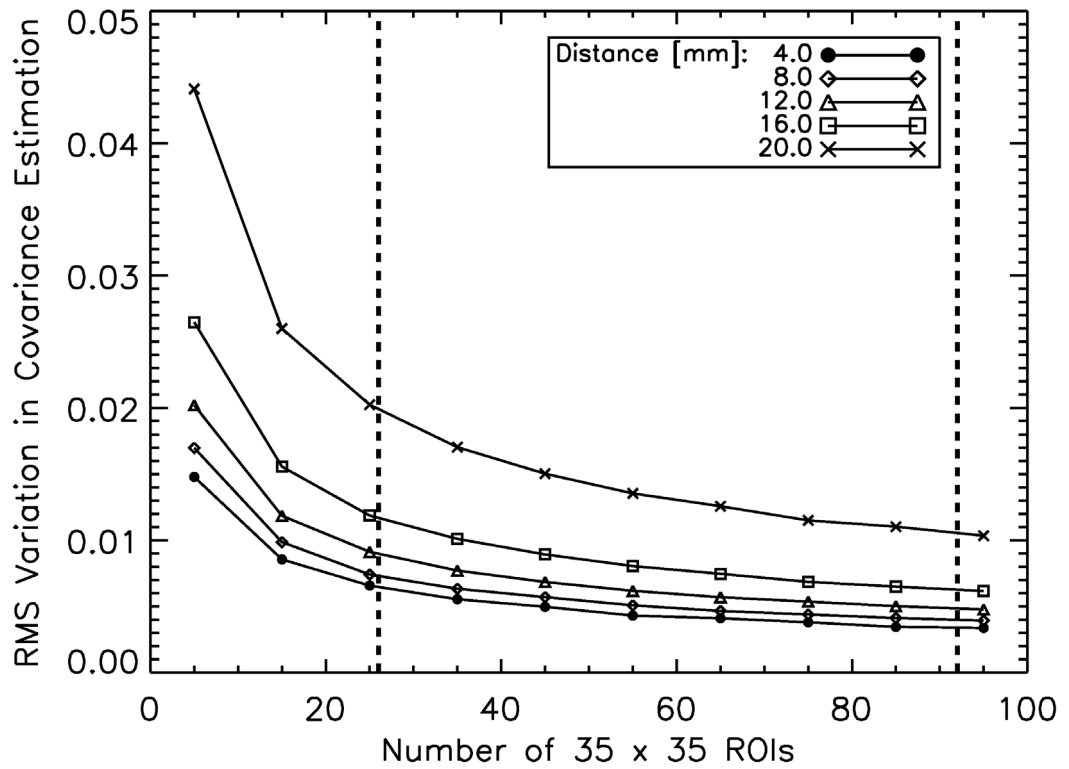
Figure 4.7: RMS variation in the stationary covariance estimate due to Rician instrumentation noise only as a function of the number of 35 x 35 voxel ROIs used in the estimation. Five different offset distances are shown. Comparing with the size of the error bars in Figure 4.6, which describe both anatomical and instrumentation errors, the instrumentation errors shown here are much less than the size of the error bars in the actual data in Figure 4.6. This indicates that the error bars in Figure 4.6 represent mostly anatomical variation.
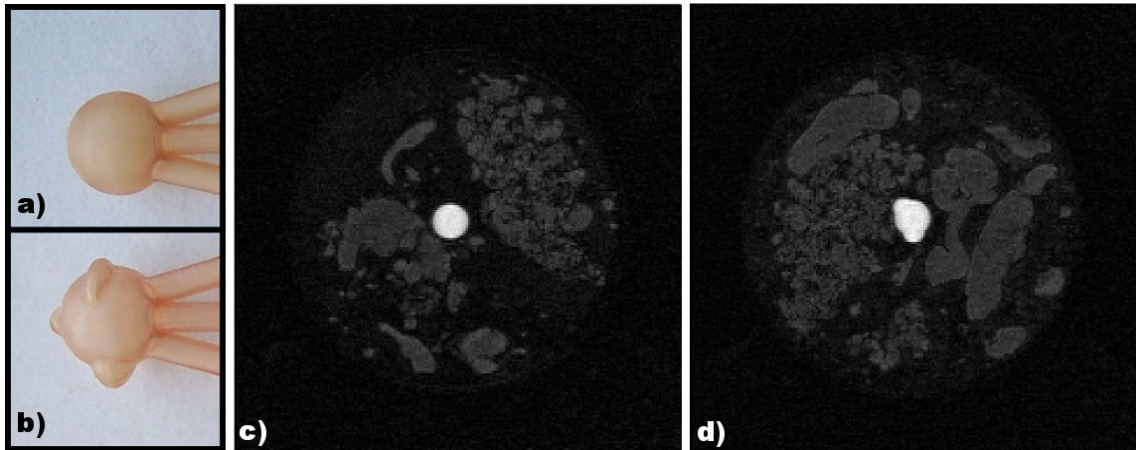
Figure 4.8: a) Photograph of round-shaped, mass-like simulating lesion (sphere internal diameter = 10 mm). The three tubes towards the right connect the lesion with the phantom jar lid and allow for filling of the lesion with contrast agent as well as future dynamic contrast agent experiments. b) Photograph of lobular-shaped, mass-like simulating lesion (3 lobulations plus 10 mm internal diameter sphere diameter). c) Fat-suppressed, T_1-weighted, gradient-echo image (0.75 mm isotropic resolution, coronal slice) of a complete phantom with the round-shaped simulating lesion inserted and filled with gadolinium-doped water. d) Same as c) with the lobular-shaped simulating lesion.

T1 and T_2 relaxation values, fat suppression, image structure, and lesion morphology and peak enhancement. We have also presented a method for quantitatively comparing the image structure of phantom data with that of patient data. This method permits formulating approaches to further improve the phantom design and production methods.

Our phantom design can be used to quantitatively compare T_1-weighting methods and fat suppression techniques of different imaging protocols, coils, contrast agent dose, and scanners at 1.5 T in terms of lesion detection. The phantom could be validated and used to compare performance at other field strengths as well. Since the lesion volumes are known, the effect of imaging protocol parameters on the ability to estimate lesion volume can also be investigated. Another important

application of the phantom is performing direct lesion detectability comparisons across different institutions since the exact same phantom set can be imaged at a variety of locations. Such comparisons may help illuminate the cause of variations in clinical performance among institutions by determining the contribution of scanner and software variability.

An extension of the phantom design allowing for investigation of dynamic parameters is underway. This will be achieved by modifying the current static lesion design to include validated contrast agent washout kinetics. Once the dynamic lesion is included, the phantom can be applied to the optimization of additional breast MRI parameters such as spatial vs. temporal resolution tradeoffs. We expect that the phantom will also be useful for quantitative evaluation of x-ray imaging since the phantom materials were selected to be similar to human breast tissue components. We are therefore currently working towards characterizing the x-ray properties of the phantom. Such a dual-modality phantom would be useful, not only for quantitative evaluation of separate modalities, but also direct comparisons between x-ray and MRI modalities to help understand which modality is optimal for a given imaging situation. Manuscripts are currently in preparation discussing the x-ray properties of the phantom and a dynamic lesion.

One of the limitations of the phantom design is an improved fat suppression compared to patient data. In addition, tissue structures in the right-left direction are, on average, larger in the current phantom design than those in patient data. Further work is necessary to determine the cause of the difference in fat suppression between patient and phantom images. If the cause of this is improved field

homogeneity in the phantom, this could be addressed by purposely mis-adjusting the shim settings of the MR scanner, or by adding distributed quantities of an MR-invisible material with a different susceptibility constant to the outside of the phantom. Another probable explanation for the difference is that human adipose tissue contains more than only lipids. It also contains vascular cells and is held in a matrix of collagen fibers. The total lipid content of human adipose tissue is 60-85%, but adipose tissue also contains 5-30% water and 2-3% protein [53]. In contrast, the adipose-mimicking material used in our phantom is 100% lipid. A future version of the phantom may address this discrepancy by mixing additional proteins or other organic elements found in vascular cells into the adipose-mimicking material, however the most appropriate materials to be used and their shelf-life must be carefully considered. Variations in fat suppression due to breast shape could be addressed by modifying the phantom jar to reproduce different breast shapes, such as conical shapes and those distorted by contact with the coil.

In terms of tissue structures, the phantom does have more isotropic tissue structures than those in patient data, however the overall size of these structures is similar to that of patient data and presents a significant improvement over what is currently available. The fact that the overall size of structures in the phantom is similar to patient data implies that optimizations performed with the phantom should be appropriate when evaluating detectability as a function of lesion size. Since the phantom has a more isotropic structure than patient data, we expect isotropic lesions to be more difficult to detect in the phantom than in patient data. Similarly, anisotropic lesions will be easier to detect in the phantom than in patient data. The

fact that these differences are quantitatively evaluated in the phantom means that optimization trends derived from the phantom can be intelligently interpreted in terms of their translation to clinical imaging.

There is some anisotropy in the phantom covariance in the direction perpendicular to the patient data. This suggests that it may be possible to adjust the phantom production to improve the phantom tissue structure. Some possibilities include modifying the stirring parameters while the egg is coagulating in the heated lard, rotating the entire phantom while cooling to room temperature or perhaps pushing the raw egg whites through a grid while they enter the heated lard in order to create long, filamentary structures. This approach might also provide fiber-like structures with some ability to control the corresponding distribution of sizes.

4.5   Conclusion

The breast MRI community currently lacks a realistic, anthropomorphic phantom that can be used to quantitatively evaluate the effect of MRI protocol parameters on lesion detectability. In this study, we propose a phantom that addresses this need. Other quantitative MRI phantoms, such as the ACR accreditation phantom and the DCE-MRI phantom under development by the Quantitative Imaging Biomarkers Alliance at the Radiological Society of North America (http://qibawiki.rsna.org), are important tools in MRI technique optimization because they allow for precise measurement of parameters such as slice thickness, resolution, and relaxation time estimation. However, these phantoms are intended

for optimization of specific image quality parameters and have no anthropomorphic shape or structure. Therefore, they are unable to probe exactly how MRI technique parameters influence lesion detectability. Anthropomorphic phantoms have been implemented in other imaging modalities and have been used to demonstrate that simple, non-anthropomorphic phantoms produce misleading results when used to optimize imaging systems [49, 82, 83, 84]. The phantom described in this work will provide a much-needed platform for better understanding the interaction of breast MRI acquisition parameters with lesion detection and estimation.

Clinical applications of breast MRI have been rapidly evolving and have demonstrated potential to improve the detection and characterization of breast lesions, particularly for high-risk patients with dense breast tissue, when compared with current standard-of-care methods. However, the advantages of breast MRI have been overshadowed by issues of performance variability and false positive findings. Our phantom design helps address these issues by allowing quantitative comparisons across breast MRI systems and protocols and by directly relating image acquisition parameters to lesion detection and estimation. Such comparisons will contribute to the standardization of breast MRI and address some of the concerns associated with its widespread clinical use.

Chapter 5

X-ray properties of the anthropomorphic, dual-modality phantom

5.1   Introduction

The[1] current landscape of breast cancer imaging is changing rapidly as researchers investigate new approaches for lesion detection. Although mammography has been shown to decrease mortality for women aged 40 and over [4], it has a low sensitivity for high-risk patients, who tend to have a higher breast density, and detects only 4 out of every 10 cancers [123].

Dynamic contrast-enhanced magnetic resonance imaging (DCE-MRI) has recently emerged as a promising modality for breast cancer detection, particularly for women with dense breasts where mammography suffers from low sensitivity. In studies of high-risk women, DCE-MRI consistently outperforms mammography, with a sensitivity of 71-77% as compared to 36-40% for mammography [123]. As a result, the American Cancer Society recommended DCE-MRI as an adjunct to mammography for screening of high risk women in 2007 [11]. However, as compared with mammography, DCE-MRI has a low and variable specificity [17, 23, 24] that results in more false positives and unnecessary procedures.

Other cutting-edge technologies that are under development are breast tomosynthesis and dedicated breast CT. Both of these modalities attempt to improve

---

[1]Work in this chapter submitted to Physics in Medicine and Biology [122].

on the sensitivity of mammography by including additional three-dimensional information and removing some of the confounding tissue overlap that makes interpretation of high breast density mammograms so problematic. Preliminary studies using tomosynthesis have shown improved lesion visibility and reduced recall rate, but may require additional dose [33, 34, 35]. The use of breast CT seems to improve visualization of masses at the expense of visualization of microcalcifications and the use of an intravenously administered, iodinated contrast medium can further improve lesion and microcalcification conspicuity [36, 37].

With such a variety of technologies available, each with its own unique advantages and disadvantages, the ability to perform quantitative performance comparisons is critical to determining the optimal clinical utility of each modality. The ideal platform for quantitative comparisons would be a well-characterized phantom with realistic tissue structure that can be used to evaluate lesion detection across all of the available modalities.

There are a variety of anthropomorphic physical phantoms already available or under development for x-ray imaging [82, 124, 125, 126, 127, 128, 129] and a smaller number available for MR imaging [51, 52]. Interesting work has also been presented in the area of anthropomorphic, computational phantoms, however these will not be discussed here since they cannot be used to test clinical systems [130, 131, 132, 133].

Anthropomorphic physical x-ray phantoms include the so-called Rachel phantom [124, 125], a phantom made of plastic spheres [82, 126, 127], and a swirled plastic slab phantom [128]. The Rachel phantom consists of a base of variable thickness tissue-equivalent plastic combined with a mercury-enhanced clinical mammogram.

This phantom is able to produce highly realistic images since its design is based on clinical mammograms, however it is difficult to manufacture and only appropriate for mammography. The plastic sphere phantom is made up of a combination of plastic spheres of different diameters contained in a rectangular plastic box. To produce a variety of different background structures, the spheres are simply stirred between data acquisitions. Although the texture is not as realistic as the Rachel phantom, the sphere phantom is very simple to construct and can easily produce different background realizations. The CIRS slab phantom is made of 6 semi-circular, equal-thickness slabs, each of which consists of two tissue-equivalent plastic materials that are swirled together to create a heterogenous structure. The x-ray attenuation co-efficient values of the two plastic materials are based on the breast tissue elemental compositions reported in Hammerstein *et al.*[134]. To create different backgrounds, the slabs can be rearranged in different orders. Although this phantom does have a heterogenous texture, it cannot create a large number of different backgrounds. In addition, it is unclear how realistic the structure is since a comparison of x-ray properties with human tissue has not been presented. Finally, a phantom is under development that is based on a computational model that can generate heterogeneous breast voxel phantoms of different compositions, sizes, and shapes [129]. It is produced by first printing the glandular portion of the phantom with a rapid proto-typing technique and a tissue-equivalent material. The printing is performed in slabs to allow access to the empty spaces, which are then filled with an epoxy-based resin meant to simulate adipose tissue. The slabs are then combined together to create the final phantom. While this phantom does have a heterogeneous structure

119

that is qualitatively similar to clinical images, it is very difficult to manufacture in its current form.

For MR imaging, the only anthropomorphic breast phantoms that the authors are aware of have similar designs that consists of a homogenous adipose-mimicking layer that surrounds a homogenous region of glandular-mimicking material [51, 52]. In both cases, the materials were chosen to match T_1 and T_2 relaxation values of human tissue, but do not have any heterogeneous structure and, therefore, have limited applicability for lesion detection studies.

None of the above phantoms can be used for both x-ray and MR imaging and, therefore, cannot be used to quantitatively compare the two techniques. In this study, we propose a dual-modality (x-ray and MRI), anthropomorphic breast phantom for the quantitative evaluation of lesion detection. The MR properties of the phantom have been previously presented in Chapter 4. Here, we extend our analysis to characterize the x-ray properties of the phantom materials.

5.2   Methods

In the following subsections, we describe the methods for construction of the phantom, comparison of x-ray attenuation coefficients and tissue structure with patient values, and calculations of x-ray scatter of the phantom.

5.2.1 Phantom construction

Procedures for construction of the phantom are similar to those described in Chapter 4. The only difference is a change in the shape of the custom jar to simulate the compressed breast shape in mammography.

Refined lard (Goya Foods, Secaucus, New Jersey or Marquez Brothers International, Inc., San Jose, California) was used to simulate adipose tissue and coagulated, fresh egg whites (Davidson's Safest Choice Pasteurized Shell Eggs, National Pasteurized Eggs, Inc., Lansing, Illinois) to simulate fibroglandular tissue. As previously described in Chapter 4, lard and egg whites were chosen because they both have a similar composition to the human tissues they are meant to simulate. For this reason, we expect our phantom to be useful for the evaluation of multiple modalities.

In Chapter 4 a custom jar was developed to simulate the shape of an uncompressed breast, since MRI is typically performed without compression. Since breast computed tomography is also performed without compression, the same uncompressed jar could be used for that modality. However, since mammography is performed with compression, we have modified the custom jar to have a compressed shape with a thickness of 4.5 cm. The lid attaches to the jar body via a ring of 24 screws through a gasketed connection and has two fill ports that are sealed with teflon tape-coated screw plugs.

To fill the phantom jar, a preservative (0.2% w/v Dowicil 75, The DOW Chemical Company, Midland, Michigan) was added to raw egg whites prior to pouring

into melted lard (heated to 110° C), and heating for 30 s while stirring at a constant rotational velocity (125 rpm). Air bubbles were removed by placing the phantom in a vacuum for 20 minutes. The mixture was then cooled at room temperature in the sealed jar and rotated periodically during cooling to help redistribute the egg whites in the lard. The percent glandular tissue of the phantoms created for the current study was 29.5% by volume (including the jar walls). This volumetric breast density is similar to that of high-risk patients as measured using MRI. In a study of asymptomatic women in the United Kingdom at high genetic risk of breast cancer, the volumetric density as estimated with MRI was 25.0 $\pm$ 15.2 (N=655, range: 2.9-87.7%) [136]. The density of the phantom can be modified by adjusting the amount of egg whites used during its construction. The shelf-life of the phantom was previously measured to be at least 9 months using the change in MRI T_1 and T_2 relaxation values as a metric.

5.2.2   X-ray attenuation coefficient

5.2.2.1   Human values

X-ray attenuation coefficients and elemental compositions of adipose and glandular breast tissues have been measured previously [134, 137, 138, 139, 140].

Johns and Yaffe [137] measured the linear attenuation coefficient (18 to 110 keV) and density of normal fat and fibrous tissue specimens obtained from ten women undergoing reduction mammoplasty and three women at autopsy.

Al-Bahri and Spyrou [138] measured linear attenuation coefficients at 59.50 keV

of adipose and glandular breast tissue samples taken from nine breast cancer menopausal patients who had undergone mastectomy. Most of the glandular tissue samples were known to contain fat tissue as well. Since no density measurements were performed, we have used the density values reported in Johns and Yaffe [137] to convert their reported linear attenuation coefficients to mass attenuation coefficients.

Poletti *et al.*[139] measured the linear attenuation coefficients at 17.44 keV, elemental compositions, and densities of breast adipose (N=4) and glandular (N=3) tissue samples taken from mastectomies. For comparison with our data, we have used their measured elemental compositions to calculate theoretical attenuation coefficient values for mammographically-relevant energies using the material database processing software from PENELOPE [104].

Tomal *et al.*[140] measured the linear attenuation coefficients at 6 discrete energies (8, 11, 15, 20, and 30 keV) of breast adipose (N=28) and glandular (N=4) tissue samples taken from mastectomies and breast reduction surgeries. To convert from linear attenuation coefficient to mass attenuation coefficient, we used the density values reported in Poletti *et al.*[139].

Hammerstein *et al.*[134] measured the density and elemental composition of adipose (N=8) and glandular (N=5) breast tissue samples taken from mastectomies. It was found that the carbon and oxygen components of both adipose and glandular tissues varied greatly between samples, probably due to physiological differences in the amount of fibrous stroma in adipose tissue and the difficulty of removing fatty material from the glandular specimens. The mass attenuation coefficients for these compositions were also estimated using the material database in PENELOPE.

123

Uncertainties were estimated in the attenuation coefficients by using the extreme ranges that were provided for carbon and oxygen.

5.2.2.2 Phantom values

The elemental compositions of lard and fresh egg whites were estimated from the USDA's National Nutrient Database for Standard Reference [55]. The mass attenuation coefficient was derived from these values using the material database in PENELOPE. The linear attenuation coefficient of egg whites has also been measured experimentally by Rao and Gregg [141] at several discrete energies from 27 to 662 keV. Measurements were performed using radioisotopes as x-ray sources and a NaI(Tl) detector. In addition, the specific gravity was measured using a Jolly balance. No further information was provided about the egg white samples or their preparation. The measured linear attenuation coefficients for egg white were 0.426 cm^{-1} at 27 keV and 0.215 cm^{-1} at 60 keV. No uncertainty estimates were provided. The specific gravity of egg white was 1.04. Therefore, the mass attenuation coefficient of egg whites, as derived from their measurements, is 0.410 cm^2/g at 27 keV and 0.207 cm^2/g at 60 keV.

5.2.3 Tissue structure

The tissue structure of the phantom was quantitatively compared with tissue structure from patient data using stationary covariance matrices. A brief overview of the stationary covariance matrix formulation is followed by a description of the

patient and phantom data used in the comparison and a description of the effect of the inclusion of an anti-scatter grid on the stationary covariance.

5.2.3.1   Stationary covariance matrix

The same framework for the comparison using stationary covariance matrices as previously described in Chapter 4 was used here. The stationary covariance matrices were calculated on left and right cranio-caudal (CC) patient and phantom mammography images. In order to combine the results for both right and left CC images, the left CC images were flipped about their vertical axis so that the chest wall was always on the same side of the image. For the patient images, the largest square ROI in the constant thickness region of the breast was selected using the procedure described in Burgess [142]. For the phantom images, the known geometry of the phantom jar was used to select the largest square ROI in the constant thickness region of the phantom.

To create an overall stationary covariance matrix for the entire patient or phantom population, the individual stationary covariance matrices were normalized by their average pixel variance and averaged together. Error bars on the overall stationary covariance matrix were estimated by calculating the standard deviation of the patient-or phantom- specific stationary covariance matrix values at each offset position.

5.2.3.2 Patient and phantom data

Coded patient data were taken from the National Cancer Institute's (NCI) Clinical Genetics Branch's Breast Imaging Study data archive. Use of the data was authorized under IRB approval from both the NCI and FDA. In the study, a total of 198 high-risk patients were imaged using various mammography machine types. Patients were enrolled between June 2002 and February 2007 and included in the study if they were between 25 and 56 years of age and considered at high genetic risk of developing breast cancer [81]. All patients with digital data available were selected for further analysis. Eight patients were excluded because of the presence of an implant or diagnosis of breast cancer before or during the course of the NCI breast imaging study. Forty patients remained for the final analysis. The digital data were acquired with a Hologic Lorad Selenia machine and the following system parameters: 28.9 mean kV (range: 24 - 38), 66 cm source-to-detector distance, 0.3 mm focal spot size, molybdenum anode target, and 70×70 μm detector pixel size. An anti-scatter grid was used during data acquisition. For patients with a compressed breast thickness less than 6.4 cm (N=30), a 30 μm thick molybdenum filter was used, otherwise (N=10) a 30 μm thick rhodium filter was used. CC view images were used for the analysis.

Twenty phantoms were fabricated and imaged[2] on a laboratory system with an x-ray tube (RAD-71SP, Varian Medical Systems, Inc., Palo Alto, CA) with a tungsten anode and a 0.3 mm focal spot and an indirect x-ray detector with 148

---

[2]with the help of Robert J. Jennings and Hugo de las Heras

126

$\times$ 148 μm pixels and 500-550 μm thick CsI (Pixium RF 4343, Thales, France). The source-to-detector distance was set equal to that of the Hologic system used to acquire the patient data. No anti-scatter grid was used. Two images were acquired of each phantom, where the phantom was flipped between exposures, to increase the amount of data available for analysis.

Since the anode material of the experimental setup was different from that used to acquire the patient data, the kV and filters used in the experimental system were adjusted to match the mean energy and half value layer (HVL) of photons absorbed in the detector in the clinical system. Experimentally measured x-ray spectra with Mo and W anodes [143, 144] were used for the analysis and modified using the attenuation coefficients and elemental compositions of each component of the imaging system using the sum rule.

This comparison was performed by first calculating the HVL of photons absorbed in the detector of the clinical system for a Mo anode, 30 μm thick Mo filter, 5.3 cm thick breast, compression plate, support and cover plate, and an amorphous selenium detector. The compression plate was included as a 2 mm thick plate of polycarbonate and the support and cover plate as 3.3 mm of carbon. The experimental system was simulated as a W anode, Mo filter, Al filter, 5.3 cm thick breast, and a CsI detector. In both cases, a 19.3% breast density was assumed (equivalent to the mean breast density from Yaffe *et al.*[145] and the breast composition was taken from the measured values in Hammerstein *et al.*[134]. The kV and Mo and Al filter thicknesses of the experimental system were adjusted until both the mean energy and HVL of photons absorbed in the detector were matched. The mean

energy and HVL of photons absorbed in the clinical system for 28.9 kV were calculated to be 20.18 keV and 0.633 mm Al, respectively. For the experimental system, a 30 μm thick Mo filter and a 0.13 mm thick Al filter with a 28 kV gave a mean energy and HVL of photons absorbed in the detector of 20.16 keV and 0.632 mm Al, respectively.

5.2.3.3   Influence of anti-scatter grid on stationary covariance

To investigate how the stationary covariance would be affected by the presence of an anti-scatter grid, we created simulated images of one of our phantoms using a Monte Carlo program as described in Section 5.2.4.1. Two simulated mammograms with no anti-scatter grid were created, one that included all scatter contributions, and the other with only primary x-rays and no scatter. The stationary covariance was calculated for both images and compared.

5.2.4   X-ray scatter

In order to estimate the amount of scatter produced by the phantom in a mammography geometry, the entire experimental system was simulated using the Monte Carlo radiation transport subroutines PENELOPE with the penEasy[3] main program [104, 146, 147]. Experimental validation of the Monte Carlo results was also performed.

---

[3]The source code of penEasy is available at http://www.upc.edu/inte/en/descarregues.php; penEasy-Imaging, an extension of penEasy for medical imaging simulations, is available at http://code.google.com/p/peneasy-imaging/.

5.2.4.1 Simulations

The experimental setup used to acquire phantom images was reproduced in the Monte Carlo software. The 28 kV tungsten anode spectrum with 0.13 mm Al and 30 μm Mo filters as calculated in Section 5.2.3.2 was used as an input to the program. The focal spot was measured experimentally via pinhole imaging and approximated in the simulation as a 0.25 mm $\times$ 0.25 mm, uniform square source. The detector was assumed to be ideal (*i.e.*, 100% detection efficiency, noise free) and had 148 μm $\times$ 148 μm pixels to match those of the actual detector. Elemental compositions of the phantom materials as estimated in Section 5.2.2.2 were used here. From the simulation, the number of detected primary as well as scattered x rays was recorded. Images were simulated for a structured phantom as well as for a homogeneous version of the phantom[4]. At least 10^{11} histories were simulated for each of the structured and homogeneous phantoms until the average uncertainty of pixels above half the maximum pixel value was below 0.7%.

A structured phantom was included in the simulation by imaging the phantom in a computed tomography (CT) scanner[5] (16 slice 1DT MX 8000, Philips, Andover, MA) and segmenting the resultant image into the various phantom materials. The CT data set was acquired with 120 kV and 300 mAs per slice and the reconstructed data set had a resolution of 0.269 mm $\times$ 0.269 mm $\times$ 0.4 mm. The reconstructed data set was segmented by visually examining a histogram of intensity values of the entire data set and applying thresholds to separate the image into four different

---

[4]by Andreu Badal

[5]with the help of Marios Gavrielides
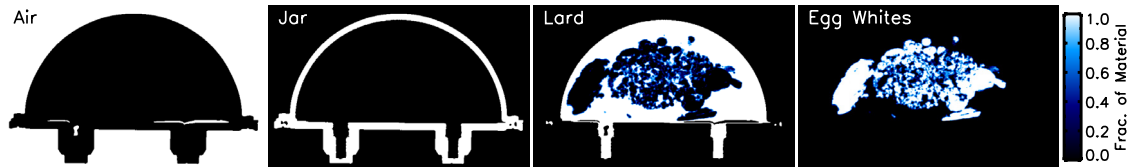
Figure 5.1: Results of segmentation algorithm on a central slice of the phantom for inclusion in the x-ray scatter simulations. For each voxel, the fraction of material that is made up of air, the jar, lard, and egg whites is indicated in each image.

material types: air, plastic jar, lard, and egg whites. Voxels with intensity values between the lard and egg white threshold levels were assigned to be a mixture of egg white and lard based on a linear scaling of the threshold value. In some areas, the simple thresholding algorithm confused voxels belonging to the jar with adipose tissue due to partial volume mixing of the jar with air. This was resolved by using a region growing algorithm with user-selected seed points to isolate the jar voxels or, in areas identified by the user as obviously belonging to the jar, by forcing all voxels above a user-selected threshold to be jar-only voxels. The region growing algorithm classified voxels as being part of the desired region by identifying all neighboring voxels with an intensity within a user-defined range. Figure 5.1 shows the segmentation of the central slice of the phantom.

A homogenous version of the phantom was created by replacing all voxels of the segmented phantom with a mixture of 30% egg whites and 70% lard. This additional simulation was carried out to facilitate comparison with previously published scatter simulations for homogeneous phantoms and to highlight the differences in scatter between homogeneous and heterogeneous phantoms. To the authors knowledge, this is the first description of scatter of a heterogeneous breast model. Therefore, our phantom provides a platform for investigation of scatter rejection and compensation

methods using a more realistic phantom with a complex tissue structure.

5.2.4.2 Experimental validation

The Monte Carlo results were validated by acquiring experimental data using the same phantom and experimental setup as used in the simulation. Images were acquired both with and without a set of 5 tungsten discs. The discs (diameter=10.0 mm, thickness=4.0 mm) were attached to the side of the phantom closest to the x-ray source using a small amount of putty between the disc and the phantom. Simulated images were also created both with and without the discs. The positions of the discs were measured during the experimental data acquisition and included in the same location for the simulations. An estimated scatter to primary ratio (SPR) for each disc was calculated using the following formula for both the simulated and experimental data:

$$SPR(x, y) = \left\langle \frac{g_i^{disc}}{g_i^{no\,disc} - g_i^{disc}} \right\rangle, \qquad (5.1)$$

where x and y indicate the position of the center of the disc, g^{disc} is the image with the disc present, $g^{no\,disc}$ is the image with no discs present, and i runs over all pixels within half a disc radius from the center of the disc. Reported errors are two standard deviations of the individual SPR values. These errors include not only statistical measurement error, but also variation due to the structured background in the phantom. We expect these estimated SPR values to underestimate the true SPR since the finite size of the disc will block low-angle scatter; however, since the
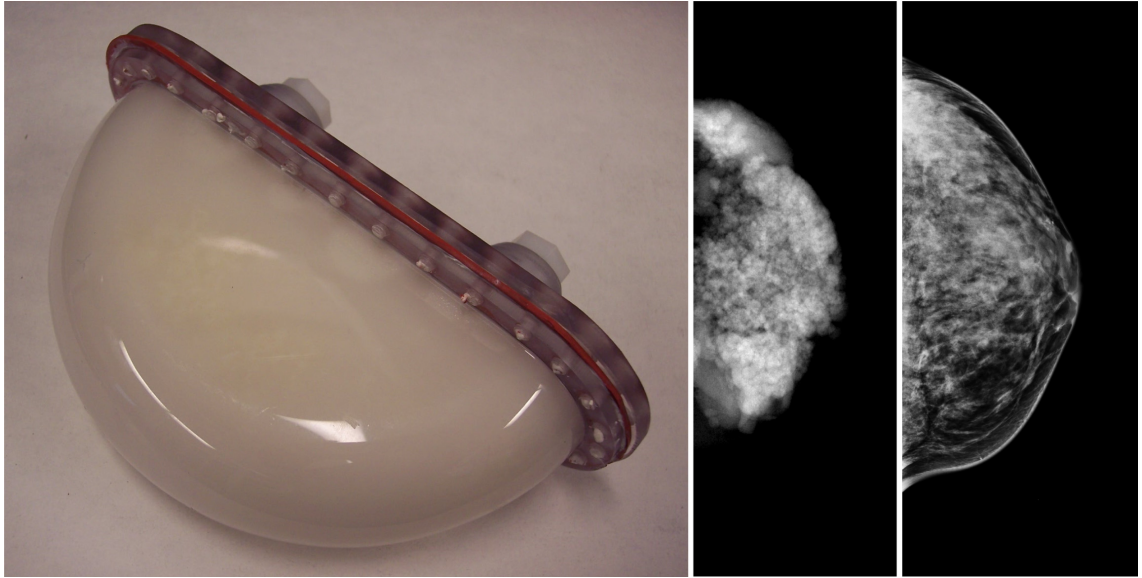
Figure 5.2: Photograph of compressed phantom (left), example x-ray image of phantom (middle), and example patient mammogram (right).

simulations were performed with the exact same geometry, we do not expect this to affect our validation.

5.3   Results

5.3.1   Phantom construction

A photograph of a filled, compressed phantom is shown in Figure 5.2 as well as example patient and phantom mammography images.

5.3.2   Attenuation coefficient

A comparison of the elemental compositions of the phantom materials with human values reported in the literature is provided in Table 5.1. As expected, both lard and egg whites provide a reasonable match to the elemental compositions

of human breast tissue. Lard is particularly well matched to the breast adipose tissue values reported by Poletti *et al.*[139], having carbon, hydrogen, and oxygen compositions that are within two times the measurement errors reported in the human tissue study. The only deviation appears to be the concentration of nitrogen, which is lower in the phantom by about 8 standard deviations. The difference between human tissue compositions reported in Hammerstein *et al.*[134] and Poletti *et al.*[139] may reflect both the difficulty of the measurement as well as the variation in human tissue values. Egg whites have similar composition values to the reported human tissue values, but with a percent carbon about 30% of the human values and a percent oxygen about 20% higher than the human tissue values. As both of the human tissue studies reported difficulty separating adipose from glandular tissue in their glandular tissue samples, it is unclear whether some of this difference is due to human tissue measurement bias. Overall, both lard and adipose tissue have a higher carbon concentration and lower oxygen concentration than both egg whites and glandular tissue.

Figure 5.3 shows a comparison between the human and phantom mass attenuation coefficient values for energies relevant to mammography, tomosynthesis, and breast CT. The ratio of total mass attenuation coefficient for phantom materials and patient tissues is shown. Examination of Figure 5.3 shows that the mass attenuation coefficient for the adipose-mimicking phantom material agrees with all breast adipose tissues values within at least 20%. Some systematic differences below about 40 keV are seen as compared with values reported by Hammerstein *et al.*[134] and Tomal *et al.*[140]. However, the excellent agreement with both experimental

133

Table 5.1: Comparison of elemental composition (reported as percent by weight) of human tissue and phantom materials.

Element	Lard	Breast Adipose		Egg Whites	Breast Glandular	
		Hammerstein et al.[134]	Poletti et al.[139]		Hammerstein et al.[134]	Poletti et al.[139]
C	76.05	61.9 (49.1-69.1)	76.5 ± 1.1	5.59	18.4 (10.8-30.5)	18.4 ± 0.9
H	12.25	11.2	12.4 ± 0.1	10.69	10.2	9.3 ± 0.5
O	11.69	25.1 (18.9-35.7)	10.7 ± 1.3	81.64	67.7 (55.2-75.9)	67.9 ± 2.0
N	0.007	1.7	0.4 ± 0.05	1.56	3.2	4.4 ± 0.6

measurements from Johns and Yaffe [137] as well as values derived from elemental compositions from Poletti *et al.*[139] indicates that this difference could be due to measurement errors or variation in human tissue properties among subjects or samples.

In Figure 5.3, data for the glandular-mimicking phantom material (egg whites) are consistent with all breast glandular values to within at least 15%. There is more deviation from breast tissue values at energies less than about 20 keV. Interestingly, at 27 keV, the experimentally measured egg white attenuation coefficient from Rao and Gregg [141] differs from the breast glandular tissue values in the opposite sense as the theoretically calculated egg white values. This indicates that the differences between experimentally and theoretically calculated mass attenuation coefficients of egg whites is about the same as the difference between the mass attenuation coefficients of egg whites and available breast glandular tissue values. The discrepancy between the measured and theoretical attenuation coefficients for egg white could be due to differences in the elemental composition of the egg white measured experimentally and the values provided by the USDA [55] and/or the inherent limitations in the way PENELOPE calculates linear attenuation coefficients for compounded materials. As commonly implemented in Monte Carlo codes, PENELOPE essentially ignores the effects of molecular binding on the individual atoms and assumes that the molecular cross-sections can be approximated by the sum of the atomic cross sections of all the atoms in the molecule (*i.e.*, the additivity approximation) [104].
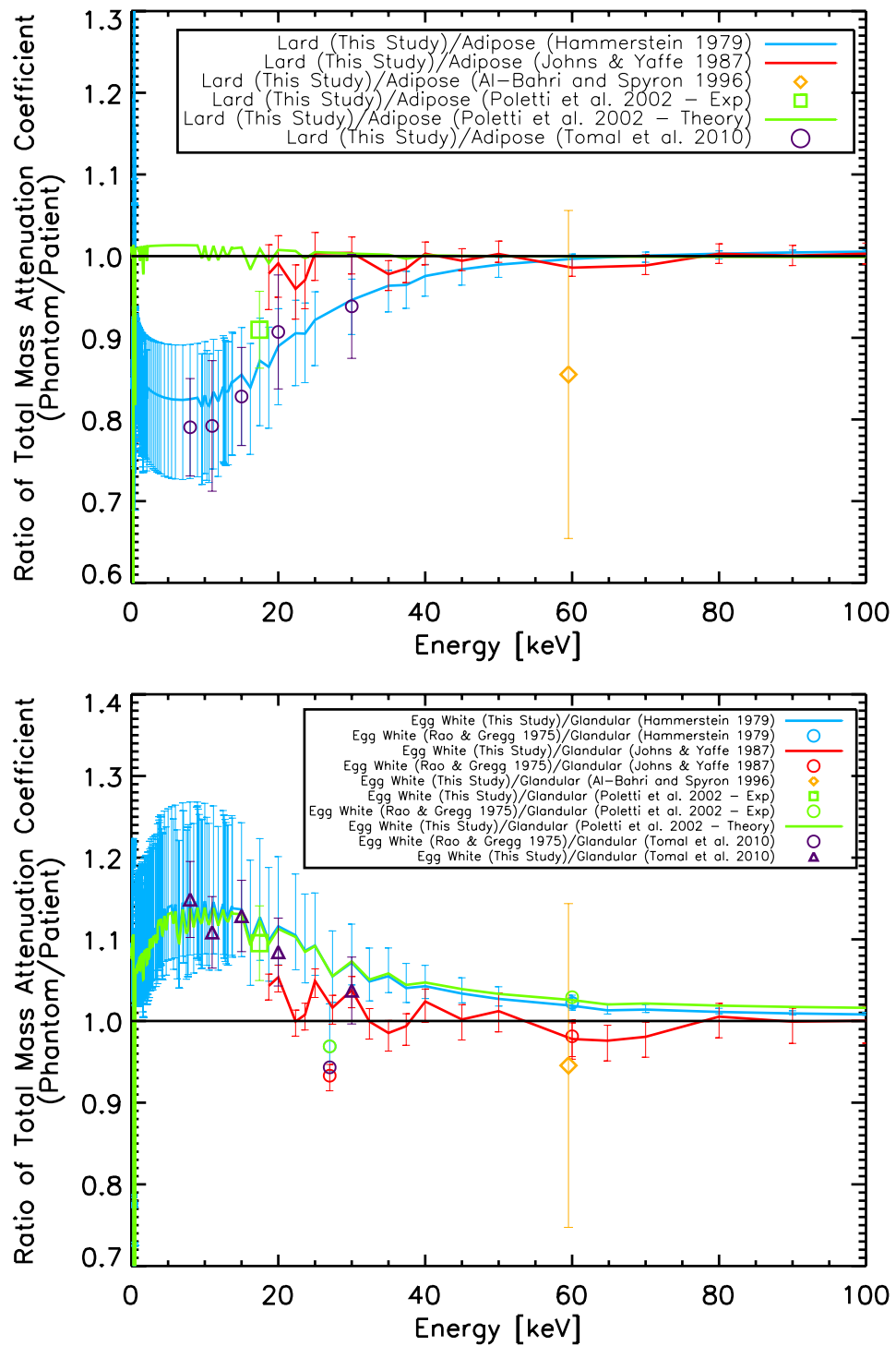
Figure 5.3: Comparison of x-ray mass attenuation coefficients for breast adipose tissue and adipose-mimicking phantom material (top) and for breast glandular tissue and glandular-mimicking phantom material (bottom). The black line represents where the indicated breast tissue and phantom values would be equal.

Given the results presented in Figure 5.3, it appears that the mass attenuation coefficients of the tissue-mimicking phantom materials are consistent with breast tissue values to within at least 20% for adipose tissue and 15% for glandular tissue and the largest discrepancies exist at energies below 20 keV.

As an interesting aside, when the attenuation coefficients of the phantom materials are calculated for energies corresponding to PET (511 keV) and SPECT (140 keV) (data not shown), they match the estimated human tissue attenuation coefficients to within 1% for adipose tissue and 2% for glandular tissue. This comparison was performed by comparing phantom values with human attenuation coefficients derived using the elemental composition from the Hammerstein *et al.*[134] and Poletti *et al.*[139] studies.

5.3.3 Tissue structure

A set of example ROIs taken from the patient and phantom mammograms are shown in Figure 5.4. Overall, the phantom provides a random structure that is qualitatively similar to the patient mammograms, but with structures that appear to be larger than those in the patient data set. Figures 5.5-5.6 show a comparison of the overall stationary covariance matrices from the patient and phantom data sets. Figure 5.5 shows the entire overall stationary covariance matrices, while Figure 5.6 shows cuts through the center of the covariance matrices with uncertainty estimates. The structure sizes are similar in the two data sets, albeit larger on average for the phantom data in the superior-inferior direction and in the anterior-posterior
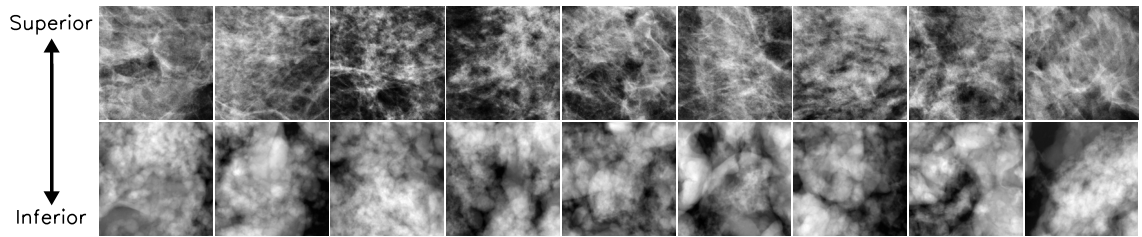
Figure 5.4: Example patient and phantom ROIs. All ROIs represent 3.5×3.5 cm in object space.
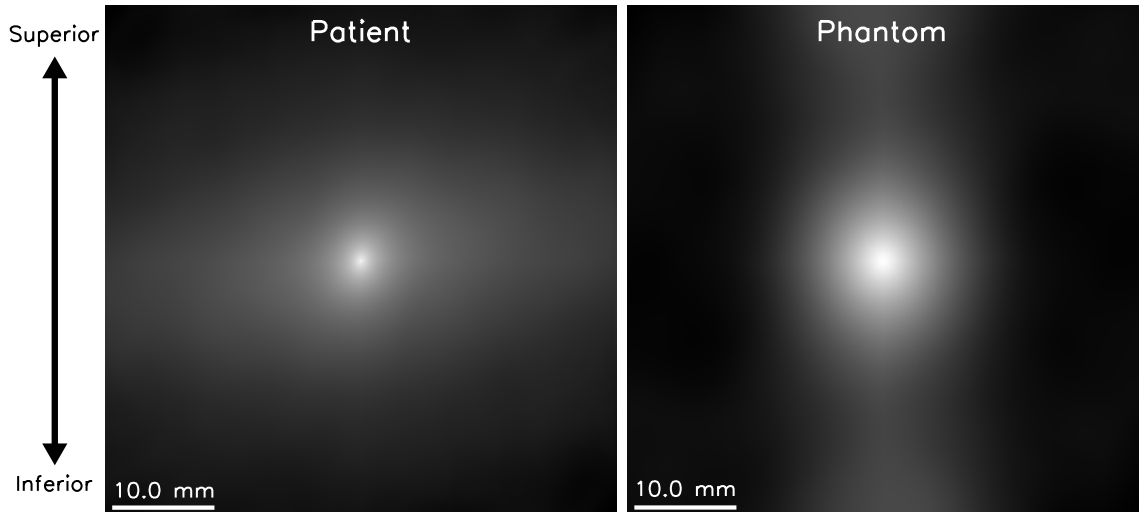
Figure 5.5: Overall stationary covariance matrices for the patient and phantom data sets. The matrices are scaled to have the same intensity at their peak. The phantom and patient overall stationary covariance matrices have similar structure sizes. The patient data set does have larger long-scale correlations in the anterior-posterior direction than the phantom data set.

direction for small distances. The error bars on the phantom covariance matrices are large in comparison to the differences between the phantom and patient data sets. In the anterior-posterior direction, the patient data set exhibits longer correlations than those present in the phantom data set.

Figure 5.7 shows the influence of scatter on the stationary covariance calculation. Cuts through the stationary covariance matrix of a single phantom are shown for simulated mammograms with and without scatter. We see that by eliminating
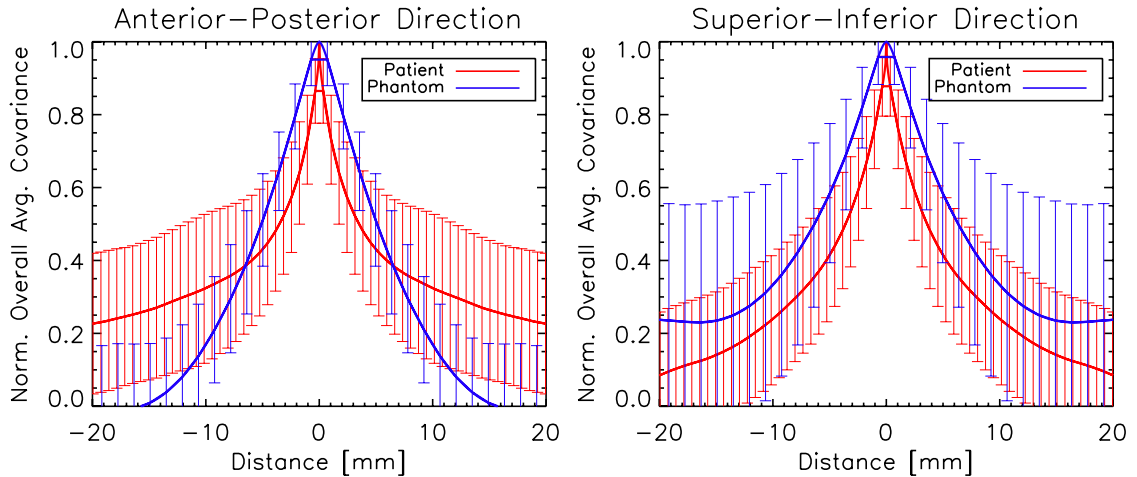
Figure 5.6: Cuts through the patient and phantom overall stationary covariance matrices (shown in Figure 5.5) in the anterior-posterior and superior-inferior directions. The patient and phantom overall stationary covariance matrices are the same to within their error bars. In the anterior-posterior direction, the patient data appears to have longer correlations on average than the patient data. Error bars are the standard deviation of the individual patient (N=80) and phantom-specific (N=40) stationary covariance matrices at each distance.

scatter completely, the stationary covariance is decreased by 15% on average and as much as 33% at larger correlation lengths in the anterior-posterior direction, and 6% on average and as much as 10% in the superior-inferior direction. Therefore, we expect that by not using an anti-scatter grid for our phantom images, we are overestimating the correlations as measured by the stationary covariance to some extent. However, the comparison shown in Figure 5.7 is a worst-case scenario since the anti-scatter grid does not eliminate scatter completely. The use of an anti-scatter grid for acquisition of the phantom data would improve the match between phantom and patient correlations in the superior-inferior direction and in the anterior-posterior direction for small-scale correlations, but potentially exacerbate the differences at larger correlation lengths for the anterior-posterior direction. The magnitude of the scatter effect on the stationary covariance matrix is, in any case, smaller than the
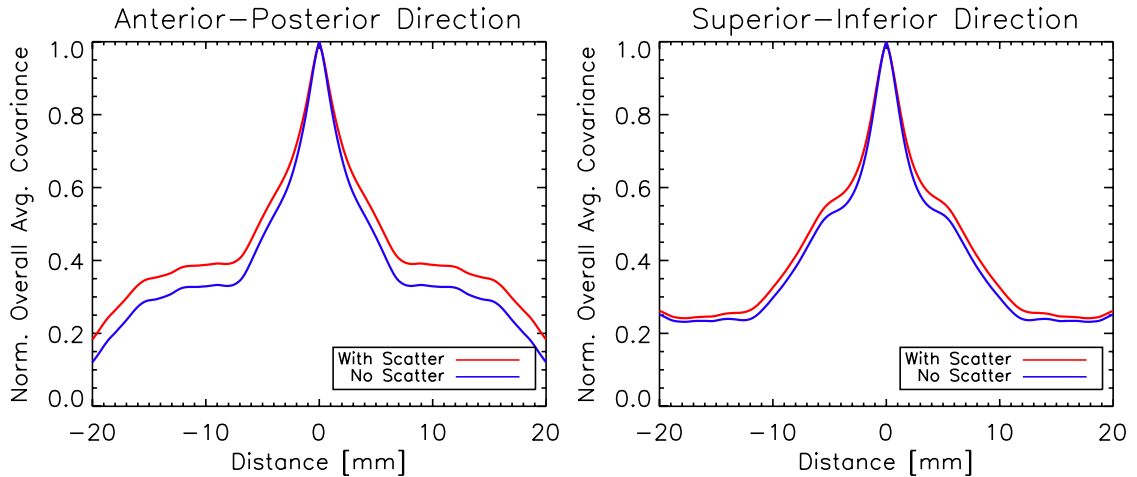
Figure 5.7: Influence of scatter on stationary covariance matrix. Stationary covariance matrices were calculated from simulated images of a single phantom with scatter and with no scatter. Cuts through the resultant stationary covariance matrices are shown in the anterior-posterior and superior-inferior directions. Removal of scatter decreases correlations by 15% on average and as much as 33% in the anterior-posterior direction and 6% on average and as much as 10% in the superior-inferior direction. Since the clinical data was acquired with an anti-scatter grid, but the experimental data was not, this effect may account for some of the differences in stationary covariance matrices between the phantom and patient data.

uncertainties in the overall stationary covariance matrices.

5.3.4   X-ray scatter

5.3.4.1   Simulations

Figure 5.8 shows results of the Monte Carlo simulations to estimate the amount of scatter produced by the phantom. Images including primary and scattered x rays, primary x rays only, and scattered x rays only are included as well as maps of the SPR of the phantom and a homogeneous version of the phantom. The image of primary plus scattered x rays represents an image with no anti-scatter grid in place. The image of the primary x rays only represents the best possible image that can

140
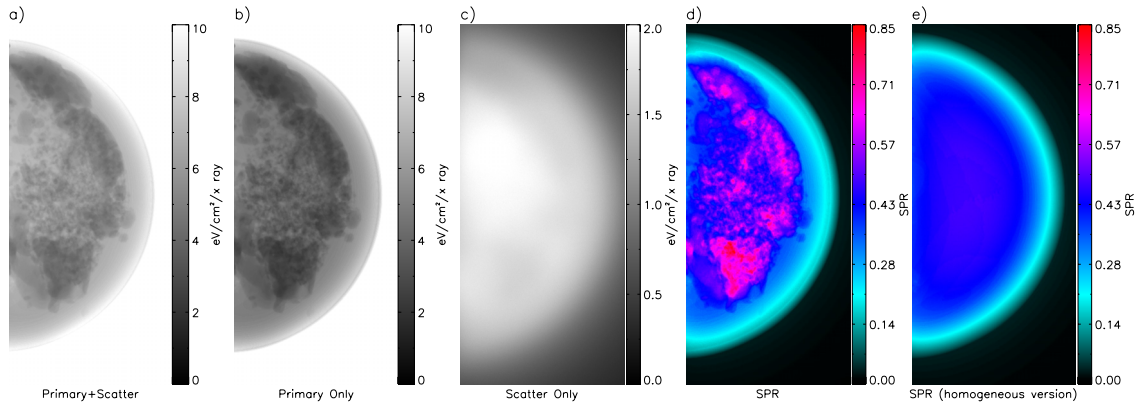
Figure 5.8: Monte Carlo simulations to estimate the amount of scatter produced by the phantom. Simulated images of (a) phantom with primary and all scattered x-rays, (b) phantom with primary x-rays only, (c) phantom with scattered x-rays only, (d) SPR of phantom, (e) SPR of a homogeneous version of the phantom. For e), all voxels of the phantom were converted in the simulation to 30% egg by volume to create a homogeneous phantom.

be achieved by any scatter correction. We see, in the image that includes only the scattered x rays, that the structure of the phantom does have an impact on spatial distribution of the scattered signal. The structure in the scatter only image comes primarily from Rayleigh interactions. The SPR is as high as 85% in some areas of the phantom. For the homogenous version of the phantom, the maximum SPR is 50%, much lower than that of the heterogeneous phantom. Therefore, estimates of patient SPR based on homogeneous phantoms may underestimate the true SPR.

5.3.4.2 Experimental validation

Results of the experimental validation of the Monte Carlo scatter simulations are shown in Figure 5.9. SPRs were experimentally measured and simulated at 5 different locations in the phantom using five tungsten discs. The experimental and simulated SPR values were in good agreement, within the error bars, for all

141
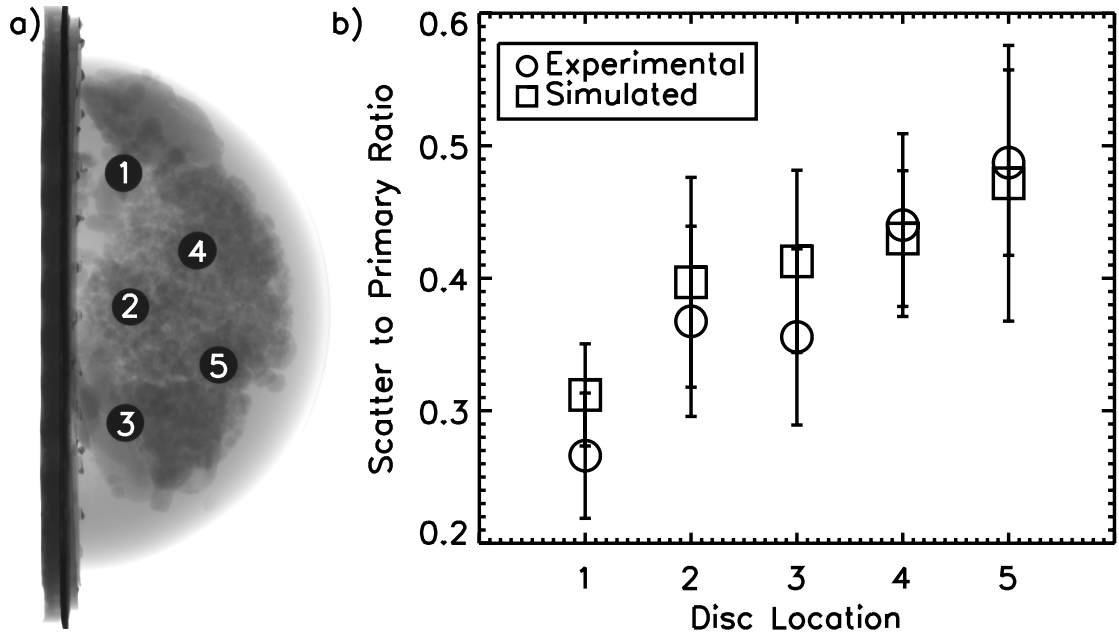
Figure 5.9: Validation of the Monte Carlo simulated scatter results for the heterogeneous phantom. Experimental measurements were performed of SPR at five different locations in the phantom using tungsten discs and also simulated with the same geometry. a) Image of phantom with discs in place. The discs are labelled 1-5. b) Comparison of the estimated scatter-to-primary ratio for each disc location. Error bars are two standard errors.

locations. Uncertainties due to voxelization and segmentation of the phantom as well as errors in replication of the experimental geometry and estimation of the material compositions contribute to the existing differences. Since the discs had a finite size and blocked some portion of the primary beam that would contribute to scattered signal, these are underestimates of the SPR values with no discs. Since the same geometry used for the experiments was reproduced in simulation, this is an appropriate validation of the SPR generated by the Monte Carlo simulations. From examination of the Monte Carlo results, we estimate that the measured SPR values underestimate the true SPR values by approximately 25%.

5.4 Discussion

In this study, we have presented a detailed analysis of our phantom's x-ray imaging properties and their comparison with human tissue properties. These comparisons have demonstrated that the phantom is useful for x-ray breast imaging evaluation and informed the reader as to where and to what extent deviations from human tissue values occur. The x-ray attenuation properties of the two tissue-mimicking materials match human data to within the measurement errors, so we expect images produced with the phantom to have similar contrast to patient images. Interestingly, attenuation coefficients of the phantom materials also match human values for energies relevant to PET and SPECT imaging, indicating that the phantom may also be useful for these modalities. Tissue-structure of the phantom data was the same as patient data to within the uncertainties, however, on average, the phantom was made up of somewhat larger structures than the patient data and has shorter-range correlations in the anterior-posterior direction. These differences should be confirmed with more data since the error bars were large; however, larger structures in the phantom data may mean that it is easier to detect larger lesions in the patient data than in the phantom data. Similarly, the longer correlation lengths in the anterior-posterior direction of the patient data may mean that it is easier to detect elongated structures in the phantom than in the patient. While some differences do exist between the phantom and patient data, they are well-characterized and, therefore, can be taken into account during lesion detection studies. Better matching between the phantom and patient image structures may be possible by

modifying the phantom construction procedures.

In a previous paper, comparisons of MRI T_1 and T_2 relaxation values and tissue structure with human data were presented. T_1 and T_2 relaxation values were shown to be in the range of human values, with better matching for T_1 values, which are most important for breast DCE-MRI. Tissue structures were shown to be similar in size, but to be more isotropic in the phantom than in patient data. This may mean that it is more difficult to detect isotropic lesions in the phantom than in patient data and vice versa for anisotropic lesions.

X-ray scatter of the phantom was also investigated via Monte Carlo simulations. While the authors are not aware of scatter measurements that have been performed on breast tissue in a mammography geometry, there are a variety of simulation studies that have investigated mammography scatter. To our knowledge, this is the first study that has presented scatter results for a non-homogeneous phantom.

A comprehensive simulation study by Boone *et al.*[148] investigated the SPR of breast tissue in mammography for a wide variety of system parameters. The mammography system was simulated without an anti-scatter grid and the simulation code was a Monte Carlo code called SIERRA, which had been previously validated. SPR was determined as a function of beam spectrum, position in the field, breast thickness, tissue composition, and area of the field of view. Homogeneous, mathematical phantoms with thicknesses ranging from 2 to 8 cm consisting of 0, 50, and 100% glandular tissue were investigated. X-ray energy and tissue composition had little effect on the SPR, while position in the field, breast thickness, and area of the field of view were significant variables. According to their equation for the SPR

at the center of mass of a semi-circular breast, they predict a SPR of 0.30 for a phantom with the same diameter and thickness as our phantom.

Another study by Sechopoulos *et al.*[149] simulated SPR of breast tissue in tomosynthesis also for a wide range of system parameters. Their results were produced with a Monte Carlo program based on the Geant4 toolkit. They simulated semi-circular, homogeneous, compressed breasts in both CC and MLO views and included the compression plate, support plate, detector cover plate, and the patient's body. The x-ray tube was simulated as a point source 66 cm from the detector. They calculated SPR at the center of mass of the breast as a function of breast size, compressed breast thickness, glandular fraction, and energy and predict a SPR of 0.55 for a CC view and a tomosynthesis angle of 0 degrees (equivalent to mammography) with a phantom that has the same thickness and average compositions as our phantom.

Our estimated SPR for a homogeneous version of our phantom is bracketed by the simulation results of Boone *et al.*[148] and Sechopoulos *et al.*[149]. The larger SPR reported by Sechopoulos *et al.*[149] as compared with Boone *et al.*[148] may be due to the fact that Sechopoulos *et al.*[149] included a compression plate, support plate, and detector cover plate in their simulations, whereas the Boone *et al.*[148] study did not. For the same reason, we would expect our results to give SPR values slightly lower than those of Sechopoulos *et al.*[149]. The larger SPR that we report, in comparison with Boone *et al.*[148], may be explained by the additional components present in our phantom (the jar lid and fill ports) that cause additional scatter. Another source of variations may be due to the fact that our simulations

used mixtures of egg whites and lard, whereas the previous studies used human tissue-equivalent materials.

The most interesting result from our study is that the actual phantom, with a heterogeneous tissue structure, results in a much larger localized SPR in regions of with a higher percentage of glandular-mimicking material than the homogeneous version of the phantom. Interestingly, this is in contradiction with the results from Boone *et al.*[148], where they find that the SPR varies by less than 0.05 for a 4 cm breast and percent glandular fractions from 0 to 100%. Sechopoulos *et al.*[149] found a somewhat larger change, with SPR varying by about 0.15 as the glandular fraction varied from 0 to 100%. Our results indicate that the glandular fraction may influence SPR more than previously thought. This means that estimates of patient SPR derived from homogeneous phantoms may give misleading results. In addition, for small and medium scattering angles, epoxy and plastic based phantoms produce scatter distributions that are very different from those of breast tissues [139]. Since our phantom materials have similar molecular structures to human tissue (see Chapter 4), it may also be true that the scatter distribution produced by our phantom is more representative of patient scatter than epoxy and plastic based phantoms, however further studies are necessary to confirm this.

5.5   Conclusion

We have developed a dual-modality, x-ray and MRI, anthropomorphic breast phantom for the quantitative evaluation of lesion detection. In this study, the x-

ray attenuation coefficients of the phantom materials as well as the phantom image structure have been shown to be similar to patient data. Estimations of the scatter-to-primary ratio of the phantom demonstrated the strong influence of heterogeneity on the calculated SPR. This platform will allow researchers to not only optimize and standardize the modalities individually, but also to compare them side-by-side. Such comparisons may help inform clinical decisions about the appropriateness of a given modality for a specific situation and improve the overall accuracy of breast imaging.

Chapter 6

MRI dynamic lesion for the anthropomorphic, dual-modality

phantom

6.1 Overview

Dynamic[1] contrast-enhanced MRI (DCE-MRI) of the breast has developed

into an important tool for breast cancer diagnosis and screening of high-risk patients.

Although the use of this technique in the clinic has led to improved sensitivity

for cancer detection, specificity limitations have highlighted a need for improved

standardization. Efforts towards more quantitative approaches to DCE-MRI are

underway, for example the Radiological Society of North America's Quantitative

Imaging Biomarker's Alliance[2], and there is a need for well-characterized phantoms

to quantitatively assess the large variety of available approaches.

Perhaps the most commonly employed phantoms for quantitative DCE-MRI

are vials filled with contrast-agent-doped solutions with varying contrast agent con-

centrations [150, 151, 152, 153, 154, 155][3]. Since MRI sequences do not directly

measure contrast agent concentration, such phantoms can be used to convert sig-

nal intensity in a T_1-weighted MRI image to contrast agent concentration, thus

---

[1]Manuscript in preparation.

[2]http://www.rsna.org/Research/QIBA

[3]and RSNA/Quantitative Imaging Biomarkers Alliance (QIBA) DCE-MRI phantom.
http://qibawiki.rsna.org

potentially improving determination of perfusion parameters. However, static T_1 phantoms inherently do not exhibit dynamic behavior and, therefore, can not be used to directly evaluate dynamic protocols.

Dynamic MRI phantoms have been presented in the literature for various applications [156, 157, 158]. Chai *et al.*[156] developed a perfusion phantom to test the ability of a new arterial spin tagging protocol to produce tagged images where the signal attenuation was linearly proportional to the tissue flow rates. Their phantom consisted of four inlet tubes feeding a plastic cylinder that was filled with a layer of small plastic beads followed by an area filled with a compressed sponge and, finally, emptied via a single outlet tube. Water was pumped through the system at a constant flow rate using a commercially available fluid pump. This phantom was not developed to produce physiological washout curves, however, one could imagine modifications to include a bolus injection of contrast agent solution at the input in an attempt to produce such curves. Further research would be required to understand whether this design could be modified to produce curves that are indeed physiological as well as to understand how the presence of the sponge affects the MRI images.

Ivancevic *et al.*[157] developed a flow phantom to investigate how flow rate affects signal intensity in fast gradient-recalled-echo sequences for quantification of arterial input functions (AIFs). A laboratory-modified, variable-speed pump was set up in closed-circuit with continuous flow of Gd-DTPA-doped solution with velocities ranging from 0-80 cm/s. To create AIFs, Gd-DTPA was injected into the water tank of the system. Continuity of the flow was measured using Doppler ultra-

sound and samples of the circulating solution were taken at the phantom outlet for every measurement and used to determine Gd-DTPA concentration by comparing against a static calibration phantom. Although this phantom is able to produce dynamic curves appropriate for its intended use, it was meant to simulate AIFs, not physiological washout curves. As a result, the entire wash-in and wash-out behavior is confined to approximately 10 s and there is no mechanism to produce longer timescale washout curves.

Finally, Ebrahimi, Swanson, and Chupp [158] have presented a microfabricated dynamic phantom, produced on a silicon wafter, with branching channels that have similar diameters to human vasculature. Their objective was to simulate blood perfusion on the microvasculature level. Washout curves were produced by using an IV pump to feed the supply channels of the phantom and injecting a contrast agent via a stopcock. Since the geometry of the phantom is well-known, fluid transfer simulations can be produced to estimate the flow behavior of the phantom. While this phantom holds promise, there are several issues that limit its applicability to the evaluation of physiological washout curves. Unfortunately, while the authors presented simulation results for flow rate in the phantom, no simulated washout curves were produced. This means that the true behavior of the phantom was unknown and it was not possible to compare MRI measurements of the phantom with the true flow behavior. In addition, the washout curves occurred on a timescale much faster than physiological curves, about 30 s.

The dynamic phantoms discussed above are important tools for the evaluation of dynamic MRI protocols. However, none of these phantoms produce physiological

washout curves or have the ability to be easily modified to mimic the variety of washout curve shapes seen in the clinic. We have previously presented an MR breast phantom with a static enhancing lesion (see Chapter 4). In this study, we extend that phantom with a dynamic lesion that is capable of producing washout curves with similar shapes and timescales as patient washout curves. In addition, the lesion is confined to a physiologically relevant space and can be modified with different border shapes to mimic different lesion types.

6.2   Methods

The overall design of the dynamic lesion phantom is diagrammed in Figure 6.1. A hollow lesion mold made from plastic is inserted in a static breast phantom. The design of the breast phantom has been previously described in Chapter 4 and consists of a breast-shaped plastic jar filled with a mixture of coagulated egg whites and lard that simulates the adipose-glandular tissue structure in human breasts and has relaxation values that match those of breast tissue. For clarity, in Figure 6.1 the phantom is shown without the egg white and lard mixture. The lesion mold has two inlets and one outlet (see Sections 6.2.1.1 and 6.3.1 for further discussion of the inlet/outlet configuration). The two inlets are fed via a fluid pump that has two separately controlled internal pumps. One of the internal pumps controls the flow rate of a tissue-mimicking fluid, while the other controls the flow rate of a contrast agent solution. The total flow rate of fluid exiting both internal pumps is set to a constant value. After both fluids leave the fluid pump, they are mixed together via

a bifurcating tube. This fluid mixture is then separated into two tubes that feed the two inlets of the hollow lesion mold. As fluid flows through the hollow lesion mold, it is expelled through the single outlet and discarded in a waste container. By modifying the relative flow rates of the two internal fluid pumps over time, the shape of the resultant washout curve in the hollow lesion mold can be controlled. The following subsections describe the design of the lesion mold itself, the choice of different washout curves and how they were produced, the x-ray measurements of the washout curve to provide truth, and the MRI measurements of the dynamic phantom.

6.2.1   Lesion mold

The lesion molds are hollow plastic molds designed to mimic mass-like lesions and confine the contrast agent solution to a physiologically relevant area in the breast phantom. The molds were manufactured using stereolithography and were produced with the thinnest possible wall for the technology (0.6 mm). A lesion size of 10 mm was chosen for this study since it is relatively small and difficult to detect. However, modifying this size for future studies would be trivial. The two major considerations in the lesion mold design were producing a reasonably uniform distribution of contrast agent solution in the interior of the mold and simulation of a realistic tumor morphology. Both of these considerations are discussed in further detail below.

Empty Phantom with Hollow Lesion Mold
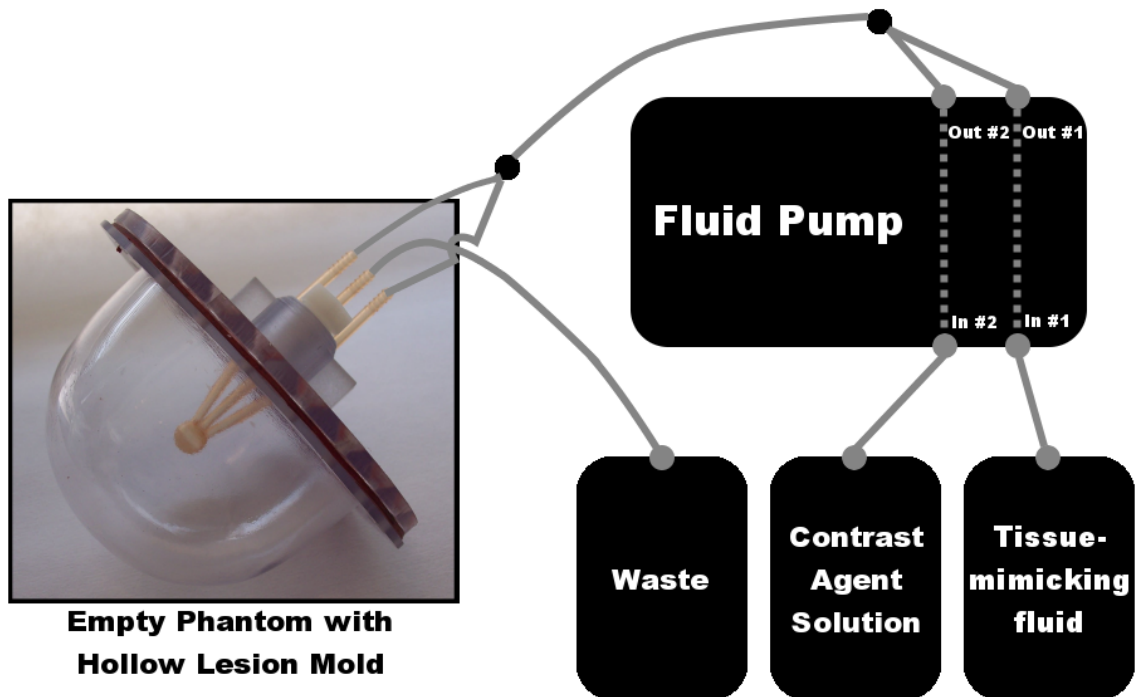
Figure 6.1: Dynamic lesion phantom design overview. On the left is an empty breast phantom jar with a hollow lesion mold inserted. For actual measurements, the phantom jar will be filled with lard and egg to simulate breast tissue, however, in this diagram, the phantom jar was left empty for clarity. The fluid pump takes in a contrast agent solution and a tissue-mimicking fluid and dispenses them separately with different flow rates as a function of time. The total exit flow rate from the fluid pump is kept constant, but the relative fraction of contrast agent solution is varied over time to produce a physiological washout curve. The two fluids are mixed together after exiting the fluid pump via a bifurcating tube. The fluid mixture is then separated and enters the two inlets in the phantom lesion mold. As the fluid exits the phantom via the single outlet tube, it is discarded in a waste container.

6.2.1.1 Distribution of contrast agent

The distribution of contrast agent in two different lesion mold designs was investigated using fluid transfer simulations performed with the computational fluid dynamics software package openFOAM (openCFD, Ltd., Berkshire, UK)[4]. The first design was a 10 mm internal diameter sphere with one 2 mm inner diameter inlet tube and one 2 mm inner diameter outlet tube. The inlet and outlet tubes were colinear and attached to the sphere through its center. This design was chosen as the simplest possible design to manufacture. The second design was also a 10 mm internal diameter sphere, but had two inlets and one outlet, all with 2 mm inner diameters. In this case, all three tubes attached to the sphere on the same side, but were separated by 15 degrees. This design is more complex to manufacture, but is expected to have better mixing properties. Figure 6.2 shows a diagram of the two different designs.

The simulations were performed with a total inlet flow rate of 1.0 ml/s and a mesh size of approximately 0.04 mm. The input fluid was simulated as a mixture of water and $GdCl_3$, where the concentration of $GdCl_3$ started at zero and at a time of 0 s instantaneously jumped to a concentration of 100%. The simulations were run for a total of 10 s. The density and viscosity of water were assumed to be 1.0 g/ml and 1.0 cP, respectively. The diffusion coefficient of $GdCl_3$ in water was assumed to be equal to the self-diffusion coefficient of water (2.66×10^{-2} m^2/s [159]) since the contrast agent solution would be a solution with a small amount of $GdCl_3$ in the

---

[4]by Prasanna Hariharan (FDA/CDRH/OSEL/DSFM)

154
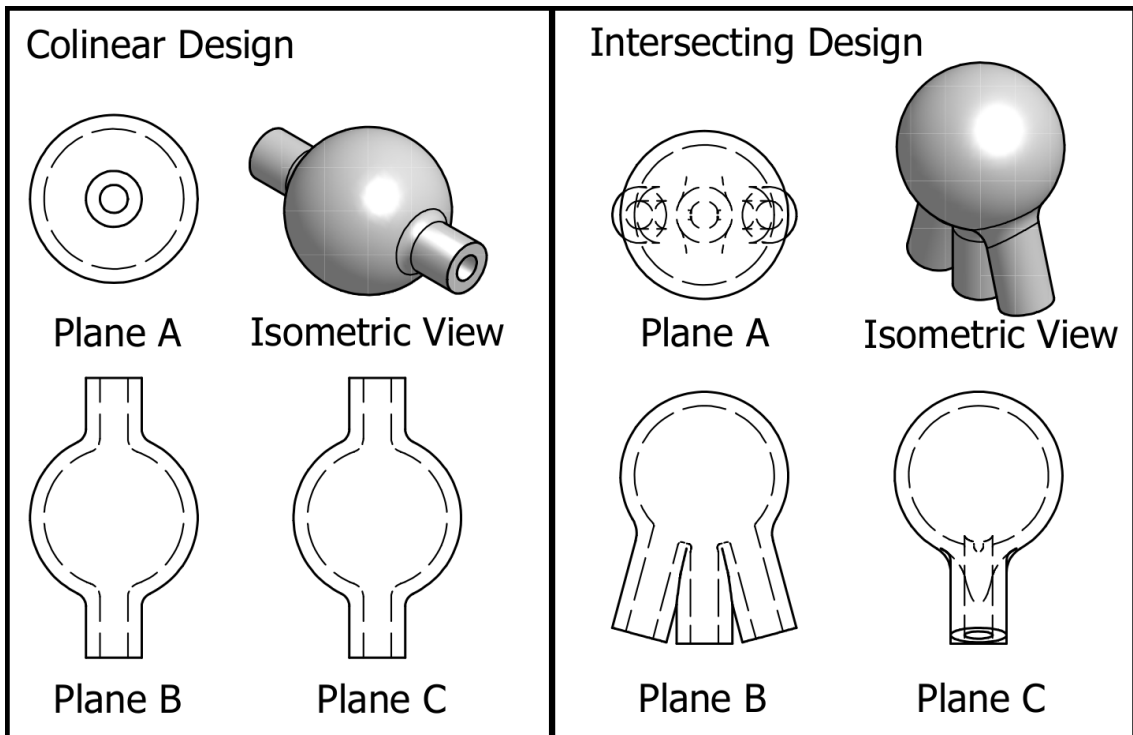
Figure 6.2: Two preliminary lesion mold designs. On the left is a 10 mm inner diameter sphere with a single inlet and a single outlet that are colinear through the center of the lesion mold. On the right is a 10 mm inner diameter sphere with 2 inlets and 1 outlet. The two inlets are on either side of the outlet at an angle of 15 degrees. The inner diameter of all inlets and outlets is 2 mm.

actual experiments.

6.2.1.2 Border shape

The border shape of breast mass-like lesions varies widely and is used as a diagnostic tool [45, 46]. Benign lesions tend to have a more smooth, spherical shape, whereas malignant lesions tend to have more irregular shapes. Here we present lesion molds with two different border shapes to demonstrate the ability of the dynamic lesion to mimic variations in this property. The first border shape is spherical, whereas the second includes three additional lobulations. Using the technique selected for producing the lesion molds (stereolithography), a variety of border shapes could easily be produced.

6.2.2 Washout curve shape

The washout curve shape was controlled via a fluid pump that interfaced with the lesion molds previously described. In the following subsections we discuss human washout curve shapes and the design of the fluid pump.

6.2.2.1 Human washout curves

In a study by Fan *et al.*[160], high temporal resolution dynamic contrast-enhanced data at 1.5 T were acquired of 22 patients with a variety of lesion types. Based on pathology, there were 6 benign, 9 ductal carcinoma in situ, two infiltrative ductal carcinoma, and one infiltrative lobular carcinoma lesions. Four patients either

had lesions missed by DCE-MRI or no lesions. In that study, the measured signal intensities were converted to contrast agent concentration and fitted to an empirical mathematical model given by

$$C\left(t\right) = A\left(1 - e^{-\alpha t}\right)^q \ e^{-\beta t} \ \frac{1 + e^{-\gamma t}}{2},$$ (6.1)

where $C\left(t\right)$ is the concentration of the contrast agent as a function of time, A is the upper limit of the concentration, α is the rate of contrast uptake (min^{-1}), β is the overall rate of contrast washout (min^{-1}), γ is the initial rate of contrast washout (min^{-1}), and q is related to the slope of early uptake and the curvature of the transition from uptake to washout. Their reported average coefficients and associated errors for all of the benign lesions were $A{=}4.0{\pm}2.1$, $\alpha{=}1.00{\pm}1.96 \ \text{min}^{-1}$, $\beta{=}0.006{\pm}0.011 \ \text{min}^{-1}$, and $q{=}0.8{\pm}0.7$. For all of the malignant lesions, the coefficients were $A{=}5.7{\pm}3.0$, $\alpha{=}1.77{\pm}0.77 \ \text{min}^{-1}$, $\beta{=}0.020{\pm}0.014 \ \text{min}^{-1}$, and $q{=}0.8{\pm}0.5$. For both benign and malignant lesions, γ was set to zero.

The objective of our phantom is to reproduce washout curve shapes such as these in the lesion mold. Although these washout curve shapes were derived from MRI measurements, we expect them to be reasonably close to the true washout curve shapes since an approximate conversion from MRI signal intensity to contrast agent concentration was performed [160]. Inaccuracies in this conversion will not affect our study since we have the ability to measure the true washout curves via x-ray measurements, as described in the following sections.

There is a considerable amount of overlap in the curve parameters for be-

nign and malignant lesions, which explains why the specificity of DCE-MRI is not consistently 100%. This overlap is probably due to both biological as well as instrumentational effects. The objective of the current study is to address the instrumentational contributions to the curve distribution overlap. While this will only address one component of the source of the overlap, it could potentially improve the separation between benign and malignant wash-out curves and, consequently, improve the specificity of DCE-MRI. For the current study, two washout curve shapes were chosen as representative benign and malignant wash-out curves. The two selected wash-out curves were generated using Eq. 6.1 with the average coefficient values for benign and malignant lesions.

6.2.2.2 Fluid pump

The fluid pump was a custom-built, MRI-compatible, programmable, dual-fluid pump (Shelley Medical Imaging Technologies, London, Ontario, Canada). It was manufactured to simultaneously pump two different liquids at different fluid flow rates that could be modified as a function of time. Fluid flow rates of the two liquids were updated on a timescale of 100 ms. One fluid was a tissue-mimicking fluid and the second was a mixture of tissue-mimicking fluid and contrast agent. These two fluids are described in more detail in the following two subsections. After exiting the fluid pump, the two fluid streams were mixed together via a bifurcated tube. The fluid pump was programmed to output a constant fluid flow rate. The relative fluid flow rates of the two liquids over time were varied by the user to the desired

values. In this way, the concentration of the contrast agent in the combined output flow could be modified by the user to reproduce any desired curve as a function of time. For both the x-ray truth and the MRI measurements, the distance between the fluid pump output and the bifurcation where the two fluids joined was 100 cm, the distance between the two bifurcation points was 40 cm, and the distance from the last bifurcation point to the inlets of the lesion mold was 200 cm. The tubing inner diameter was 4 mm.

6.2.3 X-Ray measurement of washout curve

6.2.3.1 Experimental setup

The x-ray source was a Varian B180 (Varian Corp., Salt Lake City, UT) x-ray tube with a tungsten anode, 0.3 mm focal spot, and 1.0 mm Al internal filtration. The detector, which has been previously described (see Chapter 2), was a high-resolution CCD camera (Quantix 6303 Photometrics 3072×2048 array, 9×9 μm pixels, Photometrics, Tucson, AZ) modified with a 4.5 cm length one-to-one fiber optic faceplate with 4.5 μm fibers. This fiber optic faceplate is bonded to the CCD on one side and a Hamamatsu CsI screen (0.15 mm thick CsI, Part No. J8734-01, Hamamatsu Corporation, Bridgewater, NJ) is pressure fitted to the opposite side. The entire camera assembly is covered with a 0.635 mm thick beryllium window cap. Measurements of the detector response to a 30 μm wide beam incident perpendicular to the CsI surface were performed using the same methods described in Chapter 2. The full-width at half maximum of the response is 62.2 microns, or 6.9 pixels. Since

159

the incident beam is 30 μm wide, if we assume that the CsI point response function (PRF, the detector response to an infinitely thin beam) and the incident beam can be well represented by Gaussian functions, we expect that the CsI PRF is about 54.5 μm or 6.1 pixels wide. Therefore, we can expect this amount of blur in the images of the tumor molds.

Data were acquired with the following parameters: 120 kVp, 6.4 mAs, 80 ms exposure time, temporal resolution that varied between 2.6 and 24.7 s, a single projection view, and the spherical lesion mold. The lesion mold was imaged with no surrounding jar or other phantom structure. Data were acquired with a magnification of 1.2, so the interior of the tumor mold was sampled with 1312 pixels, or approximately 215 (=1312/6.1) resolution elements. This means that, although data overlap occurs in the direction of the x-ray incidence, good spatial resolution of the lesion mold was achieved in the perpendicular direction. The lesion mold was simultaneously imaged with a vial of constant Gd-DTPA concentration to calibrate the x-ray tube output. Two x-ray experiments were performed and are described in detail in the following two subsections.

For these experiments, the tissue-mimicking fluid was a mixture of 40% glycerol and 60% deionized water, by volume, as specified by the manufacturer for appropriate lubrication of the fluid pump. The contrast agent solution was 40% glycerol by volume, 60% deionized water by volume, and 150 mM Gd-DTPA. The Gd-DTPA was prepared according to procedures described in Strich et $al.$[161] using GdCl$_3$6H$_2$O (GFS Chemicals, Columbus, OH), DTPA (Agros Organics, NJ), and NaOH (Sigma-Aldrich, St. Louis, MO).

6.2.3.2   Derivation of average lesion contrast concentration

The spatially-resolved lesion concentration was derived using the knowledge that the number of primary x-rays incident on any given location in the detector is given by

$$I = I_o \exp\left(-\mu l\right), \tag{6.2}$$

where I_o is the number of x-rays incident on the object being imaged, μ is the attenuation coefficient of the object material, and l is the size of the object along the path of the x-rays. Note that all variables in this section are a function of the position on the detector. The incoming x-rays are assumed to be parallel. In our case, the object being imaged is the lesion mold filled with a mixture of tissue-mimicking and contrast agent solutions. Therefore, we can consider the object to consist of three materials; the plastic making up the lesion mold walls, a, the tissue-mimicking fluid, b, and the contrast agent solution, c. Table 6.1 summarizes the variables used in this section and Appendix C. For any given x-ray path through the lesion mold, Eq. 6.2 can be written as

$$I = I_o \exp\left[-\left(\mu_a l_a + \mu_b l_b + \mu_c l_c\right)\right]. \tag{6.3}$$

Let's define $l_a + l_b + l_c \equiv l_{mold}$, so we can rewrite this equation as

$$I = I_o \exp\left[-\left(\mu_a f_a + \mu_b f_b + \mu_c f_c\right) l_{mold}\right], \tag{6.4}$$

where f_a, f_b, and f_c are fractional distances, and $f_a + f_b + f_c$ is always equal to one.

Table 6.1: Definition of variables for Section 6.2.3.2 and Appendix C.

Symbol		Definition
I	$\equiv$	number of x-rays incident on the detector
I_o	$\equiv$	number of x-rays incident on the lesion mold
μ	$\equiv$	linear attenuation coefficient
l	$\equiv$	distance along path of x-ray
a	$\equiv$	denotes plastic material in lesion mold walls
b	$\equiv$	denotes tissue-mimicking fluid
c	$\equiv$	denotes contrast agent solution
f	$\equiv$	fractional distance along path of x-ray
l_{mold}	$\equiv$	thickness of entire lesion mold along path of x-ray
1	$\equiv$	denotes image of lesion when no contrast agent solution is present
2	$\equiv$	denotes image of lesion when the maximum amount of contrast agent solution is present
x	$\equiv$	spatial coordinate in plane of detector
y	$\equiv$	spatial coordinate in plane of detector
E	$\equiv$	energy of x-rays
N	$\equiv$	number of detected photons
γ	$\equiv$	number of optical photons generated in the CsI crystal per incoming x-ray energy
η_{ph}	$\equiv$	efficiency of the optical detector
μ_{csi}	$\equiv$	x-ray linear attenuation coefficient of the CsI crystal
t_{csi}	$\equiv$	thickness of the CsI crystal
S	$\equiv$	normalized spectral shape of incoming x-ray beam
A	$\equiv$	$\sum_E E\,S(E)\,[1 - \exp\left(-\mu_{csi}(E)t_{csi}\right)]$
a_0	$\equiv$	coefficient describing how A varies with f_{c2}
a_1	$\equiv$	coefficient describing how A varies with f_{c2}

162

Now, if we have two images, the first of which has no contrast agent solution, 1, and the second which has an unknown amount of contrast agent solution, 2, then $f_{a1} + f_{b1} = 1$ and $f_{a2} + f_{b2} + f_{c2} = 1$. In addition, since the amount of plastic in the lesion mold never changes, $f_{a1} = f_{a2} = f_a$. I_{o1} and I_{o2} can also be assumed to be equal. Although the x-ray tube output does vary over time, the lesion mold was imaged with a vial of constant Gd-DTPA concentration to allow for normalization of the x-ray tube output. Calculating I_2/I_1 and solving for f_{c2}, we find

$$f_{c2} = \frac{1}{l_{mold}\left(\mu_b - \mu_c\right)} \ln \frac{I_2}{I_1}.$$ (6.5)

We can now normalize by the maximum fraction of f_{c2}, so that l_{mold}, μ_a, and μ_c drop out and we have

$$\frac{f_{c2}}{\max f_{c2}} = \frac{\ln \frac{I_2}{I_1}}{\ln \left(\frac{I_2\big|_{f_{c2}=max(f_{c2})}}{I_1}\right)}.$$ (6.6)

The detector efficiency is assumed to be the same for all cases, so I_1, I_2, and $I_2\big|_{f_{c2}=max(f_{c2})}$ are the image values when there is no contrast agent solution in the lesion mold, an unknown, variable amount of contrast agent solution, and a maximum amount of contrast agent solution, respectively. The error incurred by assuming that the detector efficiency is the same for any concentration of contrast agent is negligible (see Appendix C for details).

Once the normalized contrast agent fraction, $f_{c2}/\left(\max f_{c2}\right)$, was calculated for all locations in the lesion mold for each acquired image, an average normalized contrast agent fraction was calculated by averaging the values inside a circular, user-

selected region-of-interest that included the entire area inside of the lesion mold.

6.2.3.3 Flow rate measurements

X-ray data were acquired for the malignant curve shape and four different constant fluid flow rates: 1.5, 1.0, 0.5, 0.25 ml/s to determine the lowest possible fluid flow rate that would reproduce the physiological curves. It is preferable to reduce this flow rate as much as possible since rapid flow rates can affect MRI images and an increased flow rate means more fluid waste.

6.2.3.4 Benign and malignant curves

The ability of the fluid pump to repeatably create the benign and malignant washout curves was evaluated by acquiring x-ray data for five identical runs for both the benign and malignant curve shapes. Since the x-ray data were acquired at irregularly spaced time points, the resultant average normalized contrast agent concentration values were linearly interpolated to a regular grid before the average and standard deviations were calculated.

6.2.4 MRI measurements

All MRI data were acquired on a 1.5 T Siemens Magnetom scanner with an extremity coil and a fat-suppressed, 3D spoiled gradient-echo imaging protocol[5]. The scan parameters were: repetition time (TR) = 4.4 ms, echo time (TE) = 1.58 ms, flip angle = 10 degrees, field-of-view = 256×256 mm. This imaging sequence was taken

---
[5]with the help of Jacco A. de Zwart (NIH/NINDS/AMRI)

from a routine protocol used at a clinical institution with experience in breast imaging. Data were acquired of a spherical lesion with benign and malignant washout curve shapes and four different spatial (temporal) resolutions: 0.5×0.5×1.5 mm (127 s), 0.8×0.8×1.5 mm (79 s), 1.0×1.0×1.5 mm (63 s), 1.3×1.3×1.5 mm (47 s). There was no pause between temporal samples in a single dynamic acquisition. Note that the spatial resolution of the MRI data was at least 10 times worse than the spatial resolution of the x-ray truth data. Washout curves were calculated as the mean image signal in a hand-selected ROI that contained the entire lesion. Lesion average signal values were divided by the average signal in a circular ROI including glandular-mimicking tissue to correct for drift in the MRI signal.

The tissue-mimicking fluid consisted of 5.0 mM Ni-DTPA in a solution of 40% glycerol and 60% deionized water by volume. Ni-DTPA was used to match the T_1 value of the fluid to that of the glandular-mimicking component of the phantom and was produced following the method described in Tofts et al. [162]. The contrast agent solution has the same composition as the tissue-mimicking fluid, but with an additional 4.5 mM Gd-DTPA. A value of 4.5 mM Gd-DTPA was chosen as a representative maximum contrast concentration in breast lesions during DCE-MRI studies [160].

6.2.5 MRI signal behavior

In order to put the MRI measurements in context and understand how to improve them, the signal equation for a spoiled gradient-echo sequence was examined

for different flip angles and Gd doses. MRI signal intensity can be related to Gd concentration using the following equation if steady-state and the fast-exchange limit are assumed [163]

$$S = M_o \sin \alpha \; \frac{\exp^{-TE(R_{2,0}^* + r_2^* C)} \left(1 - \exp^{-TR(R_{1,0} + r_1 C)}\right)}{1 - \cos \alpha \exp^{-TR(R_{1,0} + r_1 C)}}, \qquad (6.7)$$

where M_o is the proton concentration, TR is the repetition time, TE is the echo time, α is the flip angle, C is the contrast agent concentration, $R_{1,0}$ and $R_{2,0}^*$ are the inverses of the pre-contrast longitudinal and effective transverse relaxation times ($R_{1,0} = 1/T_{1,0}$ and $R_{2,0}^* = 1/T_{2,0}^*$), and r_1 and r_2^* are the longitudinal and transverse contrast relaxitivites. In our analysis, we have chosen TR (=4.4 ms), TE (=1.58 ms), and α (=10 degrees) values equal to those used to acquire our MRI data. $T_{1,0}$ and $T_{2,0}$ values were measured on the tissue-mimicking fluid, using maximum likelihood methods that have been previously described [38], and found to be $T_{1,0}$=449.3 ms and $T_{2,0}$=136.2 ms. The measured $T_{1,0}$ value was used in the equation and $T_{2,0}^*$ was set to half of the measured $T_{2,0}$ value. The contrast relaxivity values were assumed to be equal to $r_1 = 4.5 \pm 0.04$ s^{-1}mM^{-1} and $r_2 = 5.49 \pm 0.06$ s^{-1}mM^{-1} as measured on aqueous Gd-DTPA solutions at 1.5 T [162]. Note that the addition of glycerol to an aqueous solution of Gd-DTPA is known to modify its relaxivity values because of the change in fluid viscosity [165]. However, we have chosen to use the relaxivity values for an aqueous solution here since it is unclear how the transverse relaxivity would be modified.

6.3 Results

6.3.1 Lesion molds

Figure 6.3 shows the results of the fluid transfer simulations for two different planes in the two preliminary lesion mold designs. The contrast agent distribution is presented between 2 and 10 s for every two s of the simulation for planes A and B as defined in Figure 6.2. The top row shows the results for the colinear design and the bottom row for the intersecting design. The contrast agent solution is distributed throughout the lesion mold on a much faster timescale for the intersecting design than for the colinear design. This indicates that the intersecting design will produce a more realistic immitation of actual lesions and, as a result, this inlet/outlet configuration was selected for all further development. An interesting implication is that it may be possible to produce different patterns of homogeneity or heterogeneity, to mimic different lesion types, by modifying the inlet/outlet configuration.

Photographs of lesion molds with two different border shapes are shown in Figure 6.4 to demonstrate the ability to control the morphology of the lesion. A spherical lesion mold was create as well as a lesion with three additional lobulations.

6.3.2 X-ray measurements of washout curves

Figure 6.5 shows the results of a series of experiments to determine the optimal total flow rate for the system. Four different total flow rates were investigated (0.25, 0.5, 1.0, 1.5 ml/s). Measured washout curves are compared with the desired curve
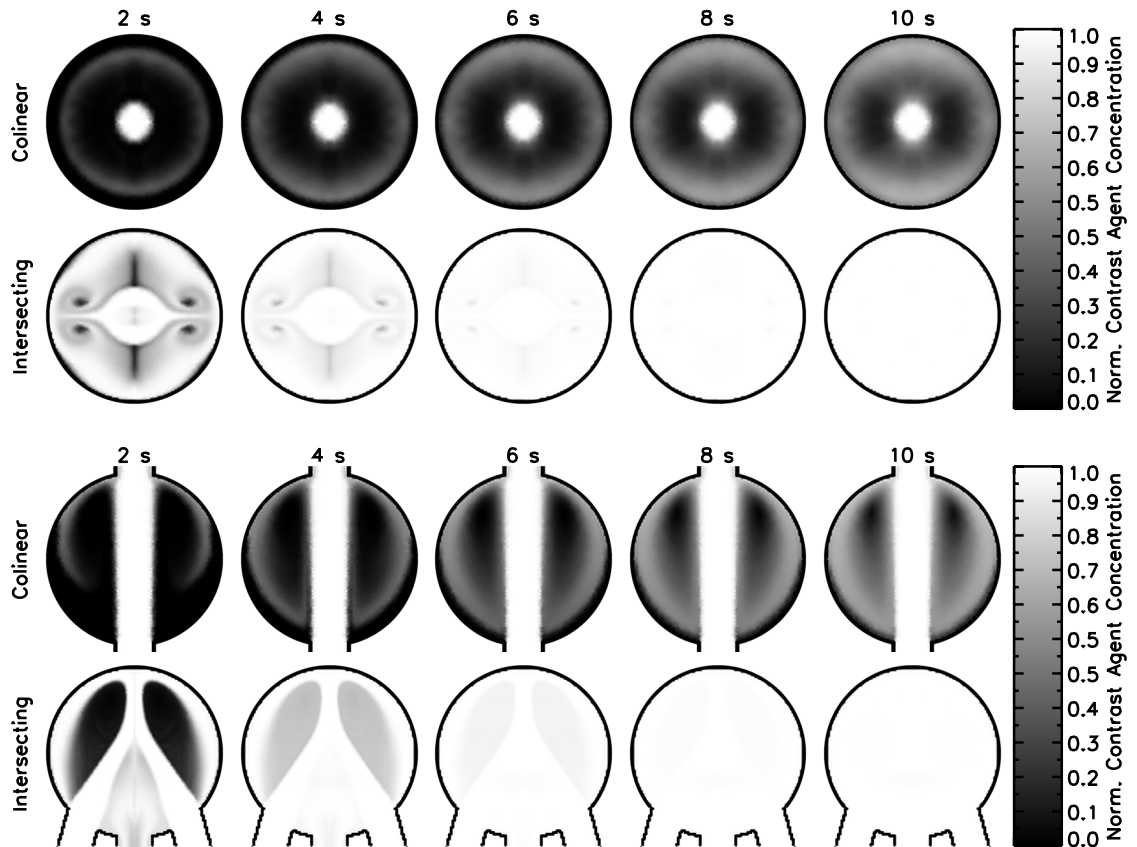
Figure 6.3: Comparison of contrast agent distribution in two different mold designs as a function of time (Views: Plane A on left, Plane B on right). The total flow rate for both mold designs was 1.0 ml/s and the mold began filled with water. At a time of 0 s, the inlet concentration of contrast agent solution instantaneously increased to 100%. The contrast solution distributes more evenly in the intersecting design than the colinear design.
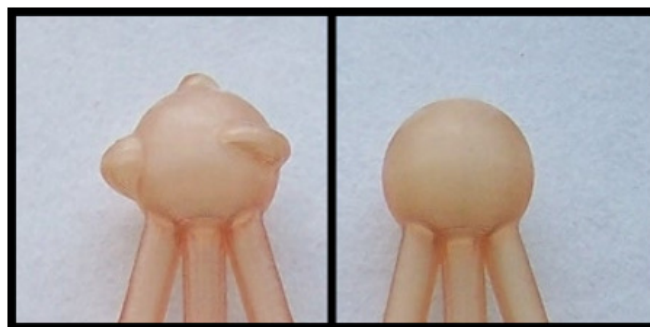
Figure 6.4: Demonstration of ability to produce lesion molds with different border shapes mimicking different mass-like lesion types. (left) lesion mold with three different irregular border shapes, or lobulations, representing a malignant lesion (right) lesion mold with smooth, spherical border shape, representing a benign lesion.
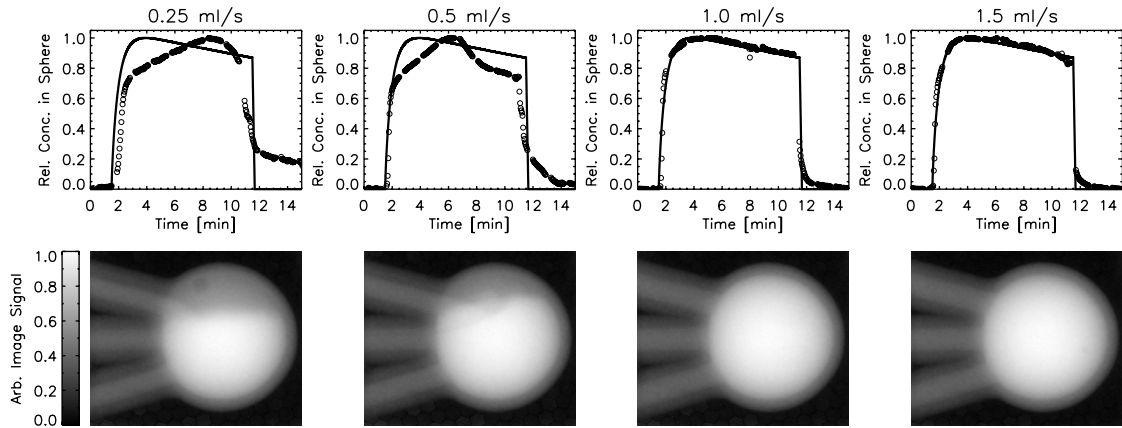
Figure 6.5: (top row) Plots of average normalized contrast agent concentration in the lesion versus time for four different total flow rates (0.25, 0.5, 1.0, 1.5 ml/s). The solid lines indicate what the fluid pump was commanded to output and the circles are values derived from the acquired data. (bottom row) Representative x-ray images of the lesion mold (inner diameter = 10 mm) for each total flow rate (at time = 5 min). A total flow rate of 1.0 ml/s is the lowest flow rate that provides good contrast agent solution mixing and a good reproduction of the desired curve.

shapes and representative x-ray images of the lesion mold for each of the flow rates are shown. Flow rates of 1.0 and 1.5 ml/s were both able to reproduce the desired curves and had an even distribution of the contrast agent solution throughout the lesion mold. Lower flow rates (0.25 and 0.5 ml/s) were unable to counteract the effect of gravity on the contrast agent solution and resulted in contrast agent solutions that settled in the bottom of the lesion mold and produced washout curves that were significantly different from the desired curves. A total flow rate of 1.0 ml/s was selected for all further studies, since it was the lowest flow rate that reliably reproduced the desired washout curve shapes.

The ability of the pump to produce benign and malignant curves is demonstrated in Figure 6.6. Average normalized contrast agent concentrations are compared with fluid pump commands for the benign and malignant curve shapes. In

169
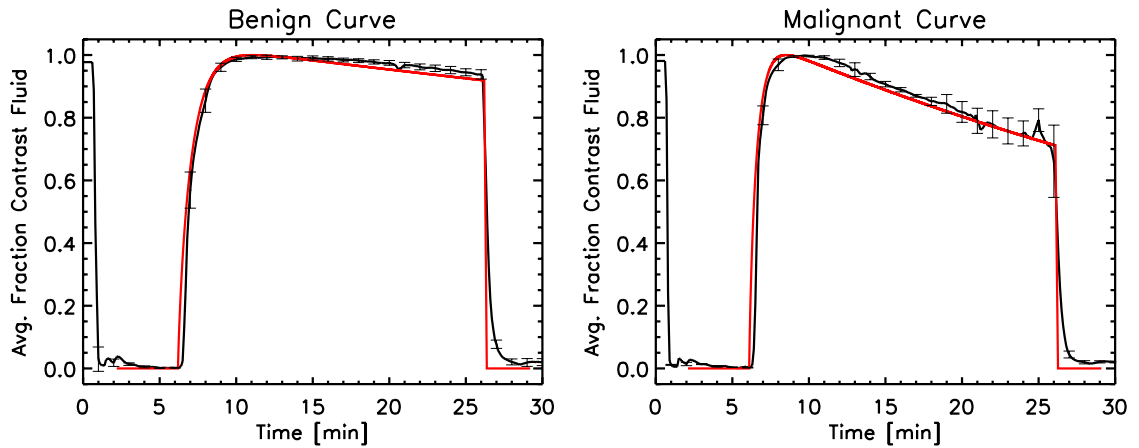
Figure 6.6: Average normalized contrast agent concentration curves for two curve shapes; benign (left) and malignant (right). The commands given to the fluid pump are shown in red and the measured values in the lesion mold averaged over five identical runs are shown in black. Error bars were calculated as standard deviations of the five runs for some of the time points. The high values in the first minute are due to the pump homing before beginning the curves and introducing contrast agent solution in the lesion mold. The system is able to reliably reproduce the two different curve types.

both cases, the desired curves are well reproduced.

6.3.3   MRI measurements

Figure 6.7 shows a comparison between the x-ray truth measurements and the MRI measurements at different resolutions. In all cases the MRI curves are flatter than the true curves, as measured by x-ray, making them more difficult to distinguish than the actual curves. This effect is most likely due to the non-linear relationship between MRI signal intensity and contrast agent concentration and will be explored further in the following subsection.
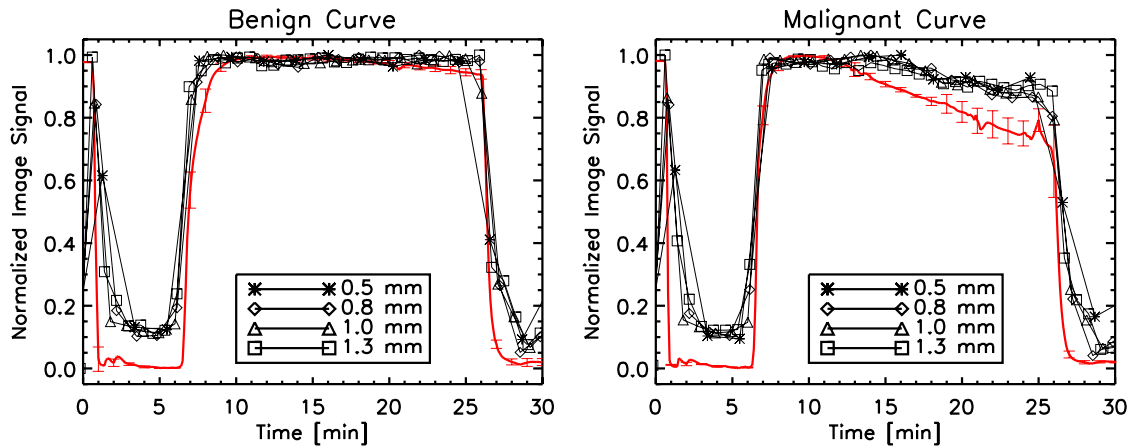
Figure 6.7: Comparison of x-ray truth measurements (red) and MRI results (black) acquired with different spatial and temporal resolutions. All curves were normalized to have the same minimum and maximum values.

6.3.4   MRI signal behavior

Figure 6.8 shows the how MRI signal intensity relates to Gd concentration for a spoiled gradient-echo sequence and parameters representative of the data acquired of our phantom. The effect of that signal behavior on the measured washout curves is also presented. As the flip angle decreases, the relationship between MRI signal intensity and Gd concentration becomes more non-linear, making it more difficult to distinguish different Gd concentrations. This effect can be seen in the middle plot of Figure 6.8, where as the flip angle decreases, the predicted measured washout curves become flatter. As seen in the right plot of Figure 6.8, the effect of decreasing flip angle on the measured washout curves can be mitigated somewhat by reducing the Gd dose. This is possible because data is collected at lower Gd concentrations, where, even at low flip angles, the MRI signal intensity varies almost linearly with Gd concentration.

171
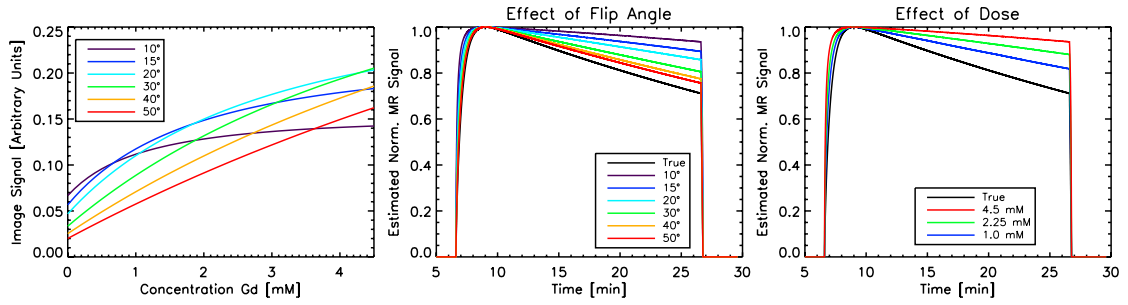
Figure 6.8: Theoretical curves showing the predicted MRI signal intensity as a function of Gd concentration are shown for different flip angles for a spoiled gradient-echo sequence (left). Predicted measured MRI curves for the same set of flip angles are shown for a dose of 4.5 mM Gd-DTPA (middle). Predicted measured MRI curves for different doses of contrast agent and a flip angle of 10 degrees are also presented (right). The true concentration versus time curve used for the calculations is shown in black in the middle and right plots. (Simulated MR parameters: Mo=1.0, TR=4.4 ms, TE=1.58 ms, T_{1o}=1242 ms, T_{2o}^*=339 ms, r1=4.5 mM^{-1}s^{-1}, r2=5.49 mM^{-1}s^{-1})

6.4   Discussion

We have produced a dynamic lesion phantom that can mimic physiological washout curves and border shapes. The shape of the washout curve can be easily modified by simply adjusting the relative fluid flow rates over time of the tissue-mimicking and contrast agent solutions. In addition, we have measured the true lesion washout curves for two specific cases using high spatial and temporal resolution x-ray imaging. Therefore, the ability of an MRI system or protocol to measure true washout curve shapes as well as differences between curve shapes can be quantitatively examined. Since differences in washout curve shape are used in the clinic for lesion diagnosis, the ability to quantitatively evaluate this property gives researchers an important tool for system and protocol optimization and has the potential to provide radiologists with data that more closely represent the true physiology.

In addition, the lesion volumes and border shapes are also known parameters that can be easily modified in the phantom and allow for quantitative studies of these properties. The ability to quantitatively evaluate lesion volume and border shape can lead to improved patient staging and aid radiologists in the differentiation of benign and malignant lesions.

Although in the current study washout curves were produced using ROIs covering the entire lesion, ROI placement for clinical exams typically covers only a small portion of the lesion and is generally a subjective practice. Using the high spatial resolution x-ray measurements of the contrast agent distribution in the lesion, studies examining the effect of differences in ROI placement on washout curve estimation can also be performed.

In the current study, washout curves measured by MRI were flatter that the true curves, as measured by x-ray, thus suggesting a more persistent uptake. This effect is likely due to the non-linear relationship between MRI signal intensity and Gd concentration. Since the true benign curve already exhibits persistent uptake, the signal behavior affects the malignant curve to a greater extent, making the benign and malignant curves appear more similar than they really are. The clinical implication is that the choice of MRI sequence can make differentiation of benign and malignant lesions more difficult. Although the current study examined only two representative curves for benign and malignant lesions, we expect this effect to apply to any realistic wash-out curve shape. Further studies could examine a larger range of wash-out curve shapes. Possible approaches to improve the matching between the measured MRI curves and the true, x-ray, curves include the use of calibration

vials with known concentrations of contrast agent as discussed in the introduction, use of a higher flip angle, or use of a lower dose of contrast agent. Each of these approaches has its own advantages and disadvantages. The use of calibration vials could allow for the correction of washout curves, however, the noise in the images would make estimation of the contrast concentration difficult, especially for signal versus Gd concentration curves that are more strongly saturated. In addition, the calibration vials would have to be placed outside of the breast, where the MR signal properties, such as coil sensitivity and flip angle, may change. Therefore, an accurate calibration would require additional measurements such as coil sensitivity maps and corrections for variation in flip angle over the image. Use of a higher flip angle would produce a more linear signal-contrast concentration relationship, however, for the short repetition times used, the overall signal level would decrease. Lower doses may also improve the linearity of the MR signal, however, this may detrimentally affect visualization of lesion morphology, such as thin spiculations. Therefore, the optimal combination of acquisition parameters must include a careful analysis that takes into account all aspects of the clinical objective.

Some areas for potential improvement of the current dynamic lesion phantom include: 1) modification of the interior structure of the lesion to allow a realistic AIF, and 2) use of an alternative lubricant for the fluids. In its current implementation, the washout curve shape in the dynamic lesion itself is essentially unchanged from the output of the fluid pump. This precludes studies examining the effect of AIF measurement on estimation of pharmacokinetic model parameters, however, the use of non-model techniques can be investigated [160, 164]. The curve shape could

174

also potentially be modified in the phantom to reproduce AIF-like shapes, thus making studies on estimation of the AIF itself possible, albeit independently from the estimation of the washout curve itself. The dynamic lesion is currently a hollow, plastic mold, however, it may be possible to include an internal porous structure to allow for both AIF and washout curve production at the same time.

In terms of the fluid lubricant, proper operation of the fluid pump requires the use of lubricant in the fluids themselves. In the present study, we use 40% glycerol by volume as a lubricant, which is recommended by the fluid pump manufacturer. Glycerol is known to affect the relaxivity of Gd-DTPA due to its viscosity, with an approximately three times increased spin-lattice relaxivity for a Gd-DTPA solution with 40% glycerol as compared with a purely aqueous solution [165]. This means that the relationship between MRI signal intensity and contrast concentration will be different for a phantom with Gd-DTPA in a solution of 40% glycerol as compared with a solution of water only. The viscosities of 100% water and a solution of 40% glycerol in water are approximately 1.0 and 5.0 cP at room temperature, respectively [166]. However, the lesion microenvironment is also known to affect relaxivity [167] and has viscosities that are higher than pure water, approximately 1.8-2.9 cP [168], meaning that a lower percentage of glycerol may be necessary to appropriately reproduce physiological viscosity. Phantoms produced with purely aqueous solutions of Gd-DTPA would have similar limitations.

It is also known that fluid flow rates can affect MRI signal intensity [157]. In the current phantom, the total flow rate is 1.0 ml/s, which corresponds to a linear flow rate of approximately 16 cm/s in each of the two inlet tubes, 32 cm/s in the

outlet tube, and lower values in the lesion itself. A study, using ultrasound Doppler imaging to measure tumor flow velocities in breast cancer patients, found that peak tumor flow velocities were in the range of 0 - 49 cm/s [169], which is consistent with the flow rates in our phantom.

An additional parameter that could be adjusted in future modifications of the phantom is the internal heterogeneity of the contrast agent uptake, which is also used by clinicians to aid in lesion diagnosis. As demonstrated in Sections 6.3.1 and 6.3.2, the configuration of the inlet/outlet tubes of the lesion and the fluid flow rate both have an effect on the interior spatial distribution of the contrast agent. Therefore, it may be possible to adjust these parameters to produce lesions with different internal heterogeneities. Extension of the fluid transfer simulations to the full timescale of physiological washout curves is currently underway. While the x-ray measurements provide a planar view of the lesion molds, the fluid transfer simulations can provide fully three-dimensional results that can be compared with MRI measurements.

In conclusion, we have developed a dynamic lesion phantom capable of re-producing physiological washout curves and border shapes for mass-like benign and malignant lesions. Since the phantom washout curves have been independently measured to provide truth, this phantom is useful for the quantitative evaluation of dynamic contrast-enhanced MRI protocols. MRI measurements of the phantom with washout curves representing benign and malignant curves shapes show that a protocol currently being used in the clinic produces MRI signal intensity curves that are less specific to lesion type than the true contrast agent concentration curves as measured by x-ray. Further development of the dynamic lesion may include adjust-

ment of the phantom parameters to control internal heterogeneity of the contrast

agent uptake.

Chapter 7

Conclusion

A variety of imaging modalities, each with its own unique set of advantages and disadvantages, are currently available or under development for breast cancer lesion detection, including dynamic contrast-enhanced MRI and x-ray techniques such as mammography, tomosynthesis, and computed tomography. The optimal acquisition parameters and clinical application of these techniques is currently an open research question. In order to provide a platform for quantitative comparison of these techniques, we have developed a multi-modality anthropomorphic breast phantom for lesion detection and discrimination. This phantom allows for system optimizations within a single modality as well as comparisons across modalities.

X-ray properties of the phantom including x-ray attenuation coefficients and tissue structure were quantitatively compared with human data and found to provide a good match. X-ray attenuation coefficients for both the glandular and adipose-mimicking phantom materials matched human values to within their measurement error. Stationary covariance matrices of phantom and patient images show that the tissue structures in the phantom have a similar characteristic size to those in patient data, but are slightly larger on average. Correlations in the patient data appear to be longer than those in the phantom data in the anterior-posterior direction, however they are within the error bars of the measurement. Detailed knowledge of x-ray

detectors was used to facilitate the tissue structure comparison. Simulated scatter-to-primary ratio values of the phantom images demonstrated the strong influence of tissue heterogeneity on these values suggesting that SPR may be underestimated by current techniques that use homogeneous phantoms.

MRI properties of the phantom, including a dynamic lesion, were also evaluated. T_1 and T_2 relaxation values of the phantom materials were found to be stable over a period of at least 9 months and in good agreement with human values, particularly for T_1 values, which are most relevant for DCE-MRI. Tissue structure in phantom images, as measured by stationary covariance matrices, matched patient data structure to within the error bars in the anterior-posterior direction and to within 2 error bars in the right-left direction. A dynamic, enhancing lesion with an adjustable border shape and washout curve behavior was also included in the phantom. Two border shapes representing benign and malignant morphologies were produced as well as two washout curve shapes typical of benign and malignant breast lesions. Truth measurements quantifying the concentration of contrast agent in the lesions over time for both of the washout curve shapes were performed using a high spatial and temporal resolution x-ray imaging system with knowledge of the x-ray detector behavior. The x-ray truth measurements were compared with dynamic MRI data of the phantom using a clinical protocol. The MRI data produced signal intensity curves that were more similar than the x-ray derived contrast agent concentration curves and examination of the spoiled gradient-echo signal equation indicated that it may be possible to improve lesion diagnosis by adjusting protocols currently being used in the clinic.

179

Chapter 8

Future Work

We have developed a dual-modality, x-ray and MRI, anthropomorphic breast phantom for quantitative evaluation of breast imaging protocols, performed quantitative comparisons with human data for the main parameters that influence image contrast and texture, and included a dynamic lesion with associated truth measurements. Several areas where the current work can be extended are discussed below.

In terms of MRI properties, 3D truth measurements of the dynamic lesion could be acquired to determine the 3D distribution of contrast agent solution in the lesion. This would allow for more detailed, spatially-resolved comparisons with the MRI data. The fluid transfer simulations could also be extended to timescales of the MRI data collection to produce maps of the 3D distribution of contrast agent in the lesion for different fluid pump commands and fluid flow rates. Additional studies of inlet/outlet configurations for the lesion may provide a method to control the internal heterogeneity of the contrast agent distribution, which is another parameter used by clinicians to diagnose lesions. One current limitation of the phantom is the inability to reproduce glandular tissue contrast agent uptake. Methods to simulate this phenomenon may also be investigated.

In terms of x-ray properties, identification of a tissue-mimicking liquid that

could be included in the lesion component of the phantom would allow for x-ray lesion detection studies. Aqueous solutions with dissolved proteins may be an option since they may have similar x-ray properties to egg whites. One possibility is a solution of denatured egg white proteins, which can be found in any supermarket. In addition to the x-ray properties of these solutions, the viscosity and coagulation properties must be investigated. In addition, while compressed versions of the phantom have been produced, ideally the phantom would be reversibly compressible so that images of the same phantom could be acquired with modalities that use compression and those that do not. The addition of microcalcifications in the phantom could also be investigated.

Preliminary evaluation of attenuation coefficients of the phantom materials also suggests that the phantom may be useful for PET and/or SPECT imaging. Characterization of the phantom material properties for these modalities would allow for additional cross-modality investigations.

For both x-ray and MRI, the lesion could be extended to a variety of sizes and to have additional border shapes. So far two example mass-like lesions have been produced, but a more careful analysis of lesion shapes in both x-ray and MRI could be performed and used to inform more realistic lesion models for the phantom. The breast density of the phantom could also be modified to cover the range of patient values. These modification would both be trivial given the phantom construction procedures. Phantom construction procedures could also be modified to improve the matching between phantom and patient tissue structure.

Numerous protocol comparisons could be performed with the phantom. As

a follow-up to the dynamic MRI data already acquired of the phantom Chapter 6, methods for improving the matching between MRI signal intensity and true contrast agent concentration could be investigated. Possible approaches are imaging vials with known contrast concentration simultaneously with the phantom to determine and apply a post-processing correction to the MRI signal intensity or increasing the flip angle or reducing the contrast agent dose of the MRI imaging protocol. All of these approaches have advantages an disadvantages, so a full analysis including all relevant effects would be required. Other MRI studies that could be performed include comparisons of imaging protocols and hardware at different institutions, analysis of the tradeoff between spatial and temporal resolution, and the effect of (contrast agent and radiation) dose on lesion detection and discrimination. Direct comparisons between x ray and MRI techniques could also be performed to determine which modality is appropriate for different patient characteristics, including breast density and size, and lesion size and morphology.

Appendix A

Integrating the PRF equation over depth

Here we derive the solution to

$$PRF(x, y, \theta, \phi, E) = \int_0^{z_{max}} PRF_z(x, y, z, \theta, \phi, E) \, \mathrm{d}z, \tag{A.1}$$

where

$$PRF_z(x, y, z, \theta, \phi, E) = \frac{\gamma E N_o \, \mu_{pe}(E) \, [a_0 \, (E) \, z + a_1 \, (E)] \, (b_0 \, z + b_1)}{1 + \left(\frac{2}{g_0 z + g_1}\right)^2 [(x - z \tan\theta)^2 + (y - z \tan\phi)^2]}. \tag{A.2}$$

To simplify the notation we can define a few variables;

$$p\,(E) \equiv \gamma E N_o \mu_{pe}(E), \tag{A.3}$$

$$q \equiv b_0, \tag{A.4}$$

$$u \equiv \tan\theta, \tag{A.5}$$

$$v \equiv \tan\phi, \tag{A.6}$$

$$m \equiv g_0^2 + 4(u^2 + v^2), \tag{A.7}$$

183

$$n \equiv 2g_0g_1 - 8(ux + vy), \tag{A.8}$$

and

$$s \equiv g_1^2 + 4(x^2 + y^2). \tag{A.9}$$

Now our integral becomes

$$PRF_z(x, y, z, \theta, \phi, E) = \int_0^{z_{max}} p\left(E\right) \left[a_0\left(E\right)z + a_1\left(E\right)\right] \left(qz + b_1\right) \left(\frac{g_0^2 z^2 + 2g_0 g_1 z + g_1^2}{mz^2 + nz + s}\right) \mathrm{d}z. \tag{A.10}$$

For the case of $x = y = \theta = \phi = 0$ this integral simplifies to

$$PRF_z(0, 0, z, 0, 0, E) = \int_0^{z_{max}} p\left(E\right) \left[a_0\left(E\right)z + a_1\left(E\right)\right] \left(qz + b_1\right) \mathrm{d}z, \tag{A.11}$$

whose solution is simply

$$PRF_z(0, 0, z, 0, 0, E) = p\left(E\right) \left[\left(\frac{a_0 q}{3}\right)z_{max}^3 + \left(\frac{a_0 b_1 + a_1 q}{2}\right)z_{max}^2 + a_1 b_1 z_{max}\right]. \tag{A.12}$$

Otherwise, we can break down the integral by multiplying it out and separating it into twelve smaller integrals $(I\text{-}XII)$ given by

$$I \equiv p\left(E\right) a_0\left(E\right) q\, g_0^2 \int_0^{z_{max}} \frac{z^4}{mz^2 + nz + s}\, \mathrm{d}z \tag{A.13}$$

184

$$II \equiv 2\, p\,(E)\ a_0\,(E)\ q\, g_0\, g_1 \int_0^{z_{max}} \frac{z^3}{mz^2 + nz + s}\, \mathrm{d}z \qquad (A.14)$$

$$III \equiv p\,(E)\ a_0\,(E)\ q\, g_1^2 \int_0^{z_{max}} \frac{z^2}{mz^2 + nz + s}\, \mathrm{d}z \qquad (A.15)$$

$$IV \equiv p\,(E)\ a_0\,(E)\ b_1\, g_0^2 \int_0^{z_{max}} \frac{z^3}{mz^2 + nz + s}\, \mathrm{d}z \qquad (A.16)$$

$$V \equiv 2\, p\,(E)\ a_0\,(E)\ b_1\, g_0\, g_1 \int_0^{z_{max}} \frac{z^2}{mz^2 + nz + s}\, \mathrm{d}z \qquad (A.17)$$

$$VI \equiv p\,(E)\ a_0\,(E)\ b_1\, g_1^2 \int_0^{z_{max}} \frac{z}{mz^2 + nz + s}\, \mathrm{d}z \qquad (A.18)$$

$$VII \equiv p\,(E)\ a_1\,(E)\ q\, g_0^2 \int_0^{z_{max}} \frac{z^3}{mz^2 + nz + s}\, \mathrm{d}z \qquad (A.19)$$

$$VIII \equiv 2\, p\,(E)\ a_1\,(E)\ q\, g_0\, g_1 \int_0^{z_{max}} \frac{z^2}{mz^2 + nz + s}\, \mathrm{d}z \qquad (A.20)$$

$$IX \equiv p\,(E)\ a_1\,(E)\ q\, g_1^2 \int_0^{z_{max}} \frac{z}{mz^2 + nz + s}\, \mathrm{d}z \qquad (A.21)$$

$$X \equiv p\,(E)\ a_1\,(E)\ b_1\, g_0^2 \int_0^{z_{max}} \frac{z^2}{mz^2 + nz + s}\, \mathrm{d}z \qquad (A.22)$$

$$XI \equiv 2\, p\,(E)\ a_1\,(E)\ b_1\, g_0\, g_1 \int_0^{z_{max}} \frac{z}{mz^2 + nz + s}\, \mathrm{d}z \qquad (A.23)$$

$$XII \equiv p\left(E\right) a_1\left(E\right) b_1 g_1^2 \int_0^{z_{max}} \frac{1}{mz^2 + nz + s} \, \mathrm{d}z \qquad (\text{A.24})$$

In order to solve these integrals we make use of standard integral solutions from the CRC standard mathematical tables and formulae [170]. Since Integrals I-XII have some standard integrals in common, we can define the solutions to those integrals as the shown below.

$$S_4 \equiv \int_0^{z_{max}} \frac{z^4}{mz^2 + nz + s} \, \mathrm{d}z \qquad (\text{A.25})$$

$$= \left[\frac{2m^2 z_{max}^3 - 3nm z_{max}^2 + 6z_{max}(n^2 - sm)}{6m^3} \right. \qquad (\text{A.26})$$

$$- \left(\frac{n^3 - 2snm}{2m^4} \right) \left[\ln\left(mz_{max}^2 + nz_{max} + s\right) - \ln\left(s\right) \right] \qquad (\text{A.27})$$

$$+ \left[\frac{n^4 - 4sn^2 m + 2s^2 m^2}{m^4 \sqrt{4sm - n^2}} \right] * \left[\tan^{-1}\left(\frac{2mz_{max} + n}{\sqrt{4sm - n^2}} \right) - \tan^{-1}\left(\frac{n}{\sqrt{4sm - n^2}} \right) \right] \left. \right] \qquad (\text{A.28})$$

$$S_3 \equiv \int_0^{z_{max}} \frac{z^3}{mz^2 + nz + s} \, \mathrm{d}z \qquad (\text{A.29})$$

$$= \left[\frac{mz_{max}^2 - 2nz_{max}}{2m^2} \right. \qquad (\text{A.30})$$

$$+ \left(\frac{n^2 - sm}{2m^3} \right) \left[\ln\left(mz_{max}^2 + nz_{max} + s\right) - \ln\left(s\right) \right] \qquad (\text{A.31})$$

$$+ \left(\frac{3snm - n^3}{m^3 \sqrt{4sm - n^2}} \right) * \left[\tan^{-1}\left(\frac{2mz_{max} + n}{\sqrt{4sm - n^2}} \right) - \tan^{-1}\left(\frac{n}{\sqrt{4sm - n^2}} \right) \right] \left. \right] \qquad (\text{A.32})$$

$$S_2 \equiv \int_0^{z_{max}} \frac{z^2}{mz^2 + nz + s} \, dz \tag{A.33}$$

$$= \left[\frac{z_{max}}{m} - \frac{n}{2m^2} \left[\ln\left(mz_{max}^2 + nz_{max} + s\right) + \ln\left(s\right) \right] \right. \tag{A.34}$$

$$\left. + \frac{n^2 - 2sm}{m^2\sqrt{4sm - n^2}} * \left[\tan^{-1}\left(\frac{2mz_{max} + n}{\sqrt{4sm - n^2}}\right) - \tan^{-1}\left(\frac{n}{\sqrt{4sm - n^2}}\right) \right] \right] \tag{A.35}$$

$$S_1 \equiv \int_0^{z_{max}} \frac{z}{mz^2 + nz + s} \, dz \tag{A.36}$$

$$= \left[\frac{1}{2m} \left[\ln\left(mz_{max}^2 + nz_{max} + s\right) - \ln\left(s\right) \right] \right. \tag{A.37}$$

$$\left. - \frac{n}{m\sqrt{4sm - n^2}} * \left[\tan^{-1}\left(\frac{2mz_{max} + n}{\sqrt{4sm - n^2}}\right) - \tan^{-1}\left(\frac{n}{\sqrt{4sm - n^2}}\right) \right] \right] \tag{A.38}$$

$$S_0 \equiv \int_0^{z_{max}} \frac{1}{mz^2 + nz + s} \, dz \tag{A.39}$$

$$= \frac{2}{\sqrt{4sm - n^2}} \left[\tan^{-1}\left(\frac{2mz_{max} + n}{\sqrt{4sm - n^2}}\right) - \tan^{-1}\left(\frac{n}{\sqrt{4sm - n^2}}\right) \right] \tag{A.40}$$

Now the solutions to Integrals I-XII are simply

$$I = p(E) \, a_0(E) \, q \, g_0^2 \, S_4, \tag{A.41}$$

$$II = 2 \, p(E) \, a_0(E) \, q \, g_0 \, g_1 \, S_3, \tag{A.42}$$

$$III = p(E) \, a_0(E) \, q \, g_1^2 \, S_2, \tag{A.43}$$

187

$$IV = p\,(E)\ a_0\,(E)\ b_1\,g_0^2\,S_3, \tag{A.44}$$

$$V = 2\,p\,(E)\ a_0\,(E)\ b_1\,g_0\,g_1\,S_2, \tag{A.45}$$

$$VI = p\,(E)\ a_0\,(E)\ b_1\,g_1^2\,S_1, \tag{A.46}$$

$$VII = p\,(E)\ a_1\,(E)\ q\,g_0^2\,S_3, \tag{A.47}$$

$$VIII = 2\,p\,(E)\ a_1\,(E)\ q\,g_0\,g_1\,S_2, \tag{A.48}$$

$$IX = p\,(E)\ a_1\,(E)\ q\,g_1^2\,S_1, \tag{A.49}$$

$$X = p\,(E)\ a_1\,(E)\ b_1\,g_0^2\,S_2, \tag{A.50}$$

$$XI = 2\,p\,(E)\ a_1\,(E)\ b_1\,g_0\,g_1\,S_1, \tag{A.51}$$

and

$$XII = p\,(E)\ a_1\,(E)\ b_1\,g_1^2\,S_0. \tag{A.52}$$

Appendix B

Influence of different detectors on covariance comparison of patient and phantom data

The influence of the use of different detector types in the acquisition of the patient and phantom data used to calculate the stationary covariances is discussed and shown to be negligible. A general discussion of how the stationary covariance matrix is influenced by different imaging systems is followed by specific discussions of the actual clinical and laboratory systems used in this study and a comparison of the two systems.

B.0.1 Comparison of covariance matrices

Since the phantom and human data were acquired on two different imaging systems, the difference between these two systems becomes confounded with differences in the objects themselves when comparing data covariances. To understand how the imaging system contributes to the data covariance, let us examine the governing equations.

We can rewrite Eq. **??** in matrix notation as

$$\mathbf{K_g} = \left\langle (\mathbf{g} - \overline{\mathbf{g}}) (\mathbf{g} - \overline{\mathbf{g}})^t \right\rangle, \tag{B.1}$$

where the data are assumed to be real-valued and $\mathbf{g}$ is a vector containing a single

image. As defined in Barrett and Myers (2004), $\mathbf{g}$ can be related to the original object via the following equation

$$\mathbf{g} = \mathbf{Hf} + \mathbf{n}, \tag{B.2}$$

where $\mathbf{f}$ is the object, $\mathbf{H}$ is the deterministic system response operator, and $\mathbf{n}$ is additive noise. The data covariance can be broken down into two independent components and written as

$$\mathbf{K_g} = \overline{\mathbf{K}}_\mathbf{n} + \mathbf{K}_{\overline{\mathbf{g}}}, \tag{B.3}$$

where $\overline{\mathbf{K}}_\mathbf{n}$ is the noise covariance matrix averaged over all $\mathbf{f}$, and $\mathbf{K}_{\overline{\mathbf{g}}}$ is the object variability as seen in the mean image (Barrett and Myers 2004). The noise covariance term is independent of $\mathbf{H}$ and the object variability term can be written as

$$\mathbf{K}_{\overline{\mathbf{g}}} \;=\; \left\langle \left[\overline{\mathbf{g}}(\mathbf{f}) - \overline{\overline{\mathbf{g}}}\right]\left[\overline{\mathbf{g}}(\mathbf{f}) - \overline{\overline{\mathbf{g}}}\right]^t \right\rangle_\mathbf{f}, \tag{B.4}$$

where $\overline{\mathbf{g}}(\mathbf{f}) = \mathbf{Hf}$ and $\overline{\overline{\mathbf{g}}} = \mathbf{H}\overline{\mathbf{f}}$. Replacing $\overline{\mathbf{g}}(\mathbf{f})$ and $\overline{\overline{\mathbf{g}}}$ in Eq. B.4 and rearranging some terms, we find that

$$\mathbf{K}_{\overline{\mathbf{g}}} = \mathbf{HK_fH}^t. \tag{B.5}$$

Now, plugging Eq. B.5 into Eq. B.3, we find that

$$\mathbf{K_g} = \overline{\mathbf{K}}_\mathbf{n} + \mathbf{HK_fH}^t. \tag{B.6}$$

190

Therefore, in order to directly compare the object covariances, $\mathbf{K_f}$, we must estimate not only the data covariance, $\mathbf{K_g}$, but also the noise covariance $\overline{\mathbf{K}}_\mathbf{n}$ and the deterministic system response operator, $\mathbf{H}$. The following three subsections describe how we estimated $\mathbf{H}$ and $\overline{\mathbf{K}}_\mathbf{n}$ for the clinical and laboratory imaging systems and how they were taken into account when comparing the data covariances. Note that, while the above derivation uses the full covariance matrix for simplification of the mathematical representation, it is also applicable to the stationary covariance matrix when appropriately averaged.

B.0.2 Clinical detector: $\mathbf{H}$ and stationary $\overline{\mathbf{K}}_\mathbf{n}$

A study by Lazarri et al. [171] measured the modulation transfer function (MTF) and normalized noise power spectrum (NNPS) of a clinical, Lorad Selenia detector, which is the same detector type used to acquire the patient data used in our study. For both measurements a Mo-Mo anode-filter combination at 28 kVp was used and the anti-scatter grid was removed. To estimate the point spread function (PSF) of the system, which we will assume is equivalent to the stationary deterministic system response operator, we selected a Gaussian PSF with a FWHM (=128.8 μm) that provided the lowest RMS difference with the MTF measured in Lazzari et al. [171].

To estimate the noise covariance matrix, we calculated the stationary covariance matrix of the noise images collected in the Lazzari et al. [171] study which were used to calculate the NNPS in that paper. Referring to Eq. B.6, the contri-

bution of the noise stationary covariance to the data stationary covariance can be considered negligible when the noise stationary covariance values are much less than the data stationary covariance values. Comparing our calculated noise stationary covariance values with the patient stationary covariance values, we find that the noise stationary covariance values are a maximum of 0.5% of the patient data stationary covariance values. As a result, we can consider the noise covariance to be negligible compared with the covariance associated with the patient tissue structure and ignore it for the purposes of comparing patient and phantom covariances.

B.0.3   Laboratory detector: $\mathbf{H}$ and stationary $\overline{\mathbf{K}_\mathbf{n}}$

The detector PSF for the laboratory detector was simulated using the MANTIS Monte Carlo simulation package[1] [90] with parameters equal to those described in Chapter 2. The thickness of the CsI layer was assumed to be 550 μm, which is the upper limit of the manufacturer's specification and, therefore, a worst-case scenario for investigating the effect of the detector PSF on the phantom stationary covariance. In addition, a columnar tilt of 5 degrees was assumed and a reflective substrate was used. The resultant PSF had a FWHM of 70.6 μm.

The noise covariance matrix was estimated from noisy images acquired in the lab with the same imaging parameters used to acquire the phantom data. A 0.85 mm thick Al filter was placed between the x-ray source and detector to simulate the x-ray spectrum when the phantom was in the beam. The x-ray exposure was also decreased so that the average detector pixel value was the same as with a phantom

---

[1]http://code.google.com/p/mantismc

in the beam. The noise stationary covariance values were a maximum of 0.3% of the data covariance values. Again, the effect of the noise covariance on the data covariance can be considered negligible and ignored.

B.0.4 Comparison of clinical and laboratory detectors

The clinical detector has a PSF with a FWHM (128.8 μm) of about twice that of the laboratory system (70.6 μm). However, we expect that the true PSF of the laboratory system will be larger than its simulated value. In a previous study, simulated PRFs for a CsI screen (denoted Screen 3 in that paper; 450 μm thick CsI screen with a reflective backing), similar to that used here in the experimental system, were compared with experimentally measured PRFs for a spectrum with a mean photon energy of 25.6 keV. In that study, it was found that MANTIS predicted a FWHM of the PRFs that was about 55% less than the experimental results (see Chapter 2). Therefore, we also calculated a PSF for the laboratory system that has been corrected for the expected underestimation from MANTIS. Its FWHM is 129.6 μm. Within the simulation errors of MANTIS, the clinical and laboratory detectors have comparable FWHM values. Note that the true PSF of the laboratory detector may be even larger than what is estimated here since the detector cover and packaging layers were not included in the MANTIS simulation or its experimental validation.

As a result of the similarity of the estimated clinical and laboratory detector PSFs, we assume that the differences in the deterministic response operators of the

two imaging systems are negligible for our purposes and directly compare the left-hand side of Eq. B.6 to compare tissue-structure of the patient and phantom data. Although this assumption is not strictly true, it is appropriate for our purposes. The covariance lengths associated with both the patient and phantom data are much longer than the covariance length imposed by either detector, so small differences in the detector PSF will not affect the final tissue structure comparison. As mentioned in Sections B.0.2-B.0.3, the noise covariance contribution to the data covariance is negligible when compared with the object variations.

Appendix C

Estimated error in contrast agent concentration due to detector

efficiency approximation

To derive the spatially-resolved lesion concentration from the x-ray data with

the detector efficiency accurately included, we must start from the following equation

$$I(x, y, E) = I_o(x, y, E) \exp \left[-\mu \left(x, y, E \right) l \left(x, y \right) \right],$$ (C.1)

which is equivalent to Eq. 6.2, but has the full spatial and energy dependence ex-

plicitly included. In this equation x and y are the spatial locations in the detector

plane and E is the energy. Now, the number of detected photons can be described

as

$$N \left(x, y \right) = \sum_E \gamma \, E \, \eta_{ph} I(x, y, E) \left[1 - \exp \left(-\mu_{csi}(E) t_{csi} \right) \right],$$ (C.2)

where γ is the number of optical photons generated in the CsI crystal per incoming

x-ray energy, η_{ph} is the efficiency of the optical detector, $\mu_{csi}(E)$ is the x-ray linear

attenuation coefficient of the CsI crystal, and t_{csi} is the thickness of the CsI crystal.

If we express $I(x, y, E)$ as

$$I(x, y, E) = I(x, y)S(E),$$ (C.3)

where $I(x, y)$ is the total number of x-ray photons incident on the detector at a given

spatial location and $S(E)$ is the percentage of x-rays at any given energy, then we can rewrite Eq. C.2 as

$$N\left(x, y\right) = \gamma \, \eta_{ph} \, I(x, y) \sum_{E} E \, S(E) \left[1 - \exp\left(-\mu_{csi}(E) t_{csi}\right)\right] \qquad \text{(C.4)}$$

$$\equiv \gamma \, \eta_{ph} \, I(x, y) \, A. \qquad \text{(C.5)}$$

We can assume that the quantities γ and η_{ph} are constant with contrast agent concentration in the lesion mold, however both $I(x, y)$ and A will change with the contrast agent concentration. Now, let's examine these two contributions in more detail to understand their dependence on contrast agent concentration. $I(x, y)$ is equal to

$$I(x, y) = I_o(x, y) \exp\left[-\mu\left(x, y\right) l\left(x, y\right)\right]. \qquad \text{(C.6)}$$

Following from Section 6.2.3.2, if we consider the object to consist of three materials $(a,\, b,\, c)$, we find that

$$\ln \frac{I_2(x, y)}{I_1(x, y)} = l_{mold}(x, y) f_{c2}(x, y) \left[\mu_b(x, y) - \mu_c(x, y)\right]. \qquad \text{(C.7)}$$

Now, we can examine how A of Eq. C.5 depends on the concentration of the contrast agent. The quantity $S(E)$ depends on contrast agent concentration since the amount of contrast agent present in the lesion will modify the spectral signature of the x-ray beam. The spectrum of x-rays entering the lesion mold was calculated using a program called SpekCalc [172] for the x-ray source used in the experimental setup. This spectrum was modified using the x-ray attenuation coefficients in the

NIST x-ray mass attenuation coefficients database[1] to calculate spectra of the x-ray beam exiting the lesion mold for different concentrations of contrast agent. The quantity A was calculated from those spectra and a linear fit was applied to determine the following relationship

$$A(f_{c2}) = a_0 + a_1 \, f_{c2}, \tag{C.8}$$

where $a_0 = 23.6139$ and $a_1 = 0.00276$. Now, combining Eqs. C.5, C.7, and C.8, we find

$$\ln \frac{N_2}{N_1} = [l_{mold} f_{c2} [\mu_b - \mu_c]] + \ln \left(\frac{a_0 + a_1 f_{c2}}{a_0} \right). \tag{C.9}$$

The second term on the right-hand side of this equation has been added by not assuming that the detector efficiency is constant with contrast agent concentration. If we estimate f_{c2} from $\frac{N_2}{N_1}$ using Eqs. 6.5 and C.9 we find that the maximum error in the estimated f_{c2} is 5×10^{-5}, where values of f_{c2} can range from 0 to 1. Therefore, the approximate model as described in Section 6.2.3.2 was used for all further analyses.

---

[1]http://www.nist.gov/pml/data/xraycoef/index.cfm

Bibliography

[1] American Cancer Society. *Cancer Facts & Figures* (American Cancer Society, Atlanta, GA, 2008).

[2] R.A. Smith, D. Saslow, K.A. Sawyer, W. Burke, M.E. Costanza, W.P. Evans III, R.S. Foster Jr., E. Hendrick, H.J. Eyre, and S. Sener. "American Cancer Society Guidelines for Breast Cancer Screening: Update 2003," CA Cancer J. Clin. **53**, 141-169 (2003).

[3] L. Bartella, C.S. Smith, D.D. Dersaw, and L. Liberman. "Imaging Breast Cancer," Radiol. Clin. N. Am. **45**, 45-67 (2007).

[4] L.L. Humphrey, M. Helfand, B.K.S. Chan, and S.H. Woolf. "Breast cancer screening: A summary of the evidence for the U.S. Preventative Services Task Force," Annals of Internal Medicine **137**, 5, E347-E367 (2002).

[5] J.A. Smith and E. Andreopoulou. "An overview of the status of imaging screening technology for breast cancer," Annals of Oncology **15**, Supplement 1, i18-i26 (2004).

[6] J.N. Wolfe. "Risk for breast cancer development determined by mammographic parenchymal pattern," Cancer **37**, 5, 2486-2492 (1976).

[7] B. Threatt, J.M. Norbeck, N.S. Ullman, R. Kummer, and P. Roselle. "Association between mammographic parenchymal pattern classification and incidence of breast cancer," Cancer **45**, 10, 2550-2556 (1980).

[8] P.M. Vacek and B.M. Geller. "A prospective study of breast cancer risk using routine mammographic breast density measurements," Cancer Epidemiol. Biomarkers Prev. **13**, 5, 715-722 (2004).

[9] J. Whitehead, T. Carlile, K.J. Kopecky, D.J. Thompson, F.I. Gilbert Jr., A.J. Present, B.A. Threatt, P. Krook, and E. Hadaway. "Wolfe mammographic parenchymal patterns. A study of the masking hypothesis of Egan and Mosteller," Cancer **56** 1280-1286 (1985).

[10] D.S. Buist, P.L. Porter, C. Lehman, S.H. Taplin, and E. White. "Factors contributing to mammography failure in women aged 40-49 years," J. Natl. Cancer Inst. **96** 1432-1440 (2004).

[11] D. Saslow, C. Boetes, W. Burke, S. Harms, M.O. Leach, C.D. Lehman, E. Morris, E. Pisano, M. Schnall, S. Sener, R.A. Smith, E. Warner, M. Yaffe, K.S.

Andrews, C.A. Russell, et al. "American Cancer Society guidelines for breast screening with MRI as an adjunct to mammography," CA Cancer J. Clin. **57**, 75-89 (2007).

[12] M.D. Schnall, J. Blume, D.A. Bluemke, G.A. DeAngelis, N. DeBruhl, S. Harms, S.H. Heywang-Kbrunner, N. Hylton, C.K. Kuhl, E.D. Pisano, P. Causer, S.J. Schnitt, D. Thickman, C.B. Stelling, P.T. Weatherall, C. Lehman, and C.A. Gatsonis. "Diagnostic architectural and dynamic features at breast MR imaging: Multicenter study," Radiology **238**, 1, 42-53 (2006).

[13] M.O. Leach. "MRI for breast cancer screening," Ann. Oncol. **17(Suppl 10)**, x325-x331 (2006).

[14] C.K. Kuhl, "Current status of breast MR imaging. Part 2. Clinical applications," Radiology **244**, 672-691 (2007).

[15] F. Sardanelli, G.M. Giuseppetti, P. Panizza, M. Bazzocchi, A. Fausto, G. Simonetti, V. Lattanzio, and A. Del Maschio for the Italian Trial for Breast MR in Multifocal/Multicentric Cancer. "Sensitivity of MRI versus mammography for detecting foci of multifocal, multicentric breast cancer in fatty and dense breasts using the whole-breast pathologic examination as a gold standard," AJR **183**, 1149-1157 (2004).

[16] M. Van Goethem, W. Tjalma, K. Schelfout, I. Verslegers, I. Biltjes, and P. Parizel. "Magnetic resonance imaging in breast cancer," EJSO **32**, 901-910 (2006).

[17] W.A. Berg, L. Gutierrez, M.S. NessAiver, W.B. Carter, M. Bhargavan, R.S. Lewis, and O.B. Ioffe. "Diagnostic accuracy of mammography, clinical examination, US, and MR imaging in preoperative assessment of breast cancer," Radiology **233**, 830-849 (2004).

[18] C.D. Lehman, C. Gatsonis, C.K. Kuhl, R.E. Hendrick, E.D. Pisano, L. Hanna, S. Peacock, S.F. Smazal, D.D. Maki, T.B. Julian, E.R. DePeri, D.A. Bluemke, and M.D. Schnall for the ACRIN Trial 6667 Investigators Group. "MRI evaluation of the contralateral breast in women with recently diagnosed breast cancer," N Engl J Med **356**, 13, 1295-1303 (2007).

[19] C. Kuhl, W. Kuhn, M. Braun, and H. Schild. "Pre-operative staging of breast cancer with breast MRI: One step forward, two steps back?," The Breast **16**, S34-S44 (2007).

[20] Aurora breast MRI well poised to help meet increased demand for breast MRI screening of high risk patients per new guidelines

from American Cancer Society, Andover, MA, March 29, 2007, http://www.auroramri.com/mri/news/news-increased-demand.shtml.

[21] http://www.cancer.gov/newscenter/pressreleases/MRIContralateralQandA, Posted 03/28/2007, National Cancer Institute.

[22] S. McElroy. "Christina Applegate battling cancer," August 4, 2008, The New York Times, http://www.nytimes.com/2008/08/04/arts/04arts-CHRISTINAAPP_BRF.html?_r=1&oref=slogin.

[23] S.H. Heywang-Köbrunner, P. Viehweg, A. Heinig, and C. Küchler, "Contrast-enhanced MRI of the breast: accuracy, value, controversies, solutions," Eur. J. Radiol. **24**, 94-108 (1997).

[24] S.H. Heywang-Köbrunner, U. Bick, W.G. Bradley, Jr., B. Boné, J. Casselman, A. Coulthard, U. Fischer, M. Müller-Schimpfle, H. Oellinger, R. Patt, J. Teubner, M. Friedrich, G. Newstead, R. Holland, A. Schaener, E.A. Sickles, L. Tabar, J. Waisman, and K.D. Wernecke. "International investigation of breast MRI: results of a multicentre study (11 sites) concerning diagnostic parameters for contrast-enhanced MRI based on 519 histopathologically correlated lesions," Eur. Radiol. **11**, 531-546 (2001).

[25] K.Y. Bilimoria, A. Cambic, N.M. Hansen, and K.P. Bethke. "Evaluating the impact of preoperative breast magnetic resonance imaging on the surgical management of newly diagnosed breast cancers," Arch. Surg. **142**, 441-445 (2007).

[26] K. Hede. "Possible MRI-mastectomy link sparks debate on MRIs role in breast cancer management," J. Natl. Cancer Inst. **100**, 1052-1054 (2008).

[27] M. Morrow. "Magnetic resonance imaging in the preoperative evaluation of breast cancer: primum non nocere," J. Am. Coll. Surg. **198**, 240-241 (2004).

[28] I. Bedrosian, R. Mick, S.G. Orel, M. Schnall, C. Reynolds, F.R. Spitz, L.S. Callans, G.P. Buzby, E.F. Rosato, D.L. Fraker, and B.J. Czerniecki. "Changes in the surgical management of patients with breast carcinoma based on preoperative magnetic resonance imaging," Cancer **98**, 3, 468-473 (2003).

[29] N. Houssami, S. Ciatto, P. Macaskill, S.J. Lord, R.M. Warren, J.M. Dixon, and L. Irwig. "Accuracy and surgical impact of magnetic resonance imaging in breast cancer staging: Systematic review and meta-analysis in detection of multifocal and multicentric cancer," J. Clin. Oncol. **26**, 19, 3248-3257 (2008).

[30] K.E. Pengel, C.E. Loo, H.J. Teertstra, S.H. Muller, J. Wesseling, J.L. Peterse, H. Bartelink, E.J. Rutgers, and K.G.A. Gihuijs. "The impact of preoperative

MRI on breast-conserving surgery of invasive cancer: a comparative cohort study," Breast Cancer Res. Treat. **116**, 1, 161-169 (2009).

[31] A. Hlawatsch, A. Teifke, M. Schmidt, and M. Thelen. "Preoperative assessment of breast cancer: Sonography versus MR imaging," AJR **179**, 1493-1501 (2002).

[32] K. Pettit, M.E. Swatske, F. Gao, L. Salavaggione, W.E. Gillanders, R.L. Aft, B.S. Monsees, T.J. Eberlein, J.A. Margenthaler. "The impact of breast MRI on surgical decision-making: are patients at risk for mastectomy?" Journal of Surgical Oncology **100**, 7, 553-558 (2009).

[33] S.P. Poplack, T.D. Tosteson, C.A. Kogel, and H.M. Nagy. "Digital breast to-mosynthesis: initial experience in 98 women with abnormal digital screening mammography," AJR Am. J. Roentgenol. **189**, 616-623 (2007).

[34] I. Andersson, D.M. Ikeda, S. Zackrisson, M. Ruschin, T. Svahn, P. Timberg, and A. Tingberg. "Breast tomosynthesis and digital mammography: a comparison of breast cancer visibility and BIRADS classification in a population of cancers with subtle mammographic findings" Eur. Radiol. **18**, 2817-2825 (2008).

[35] D. Gur, G.S. Abrams, D.M. Chough, M.A. Ganott, C.M. Hakim, R.L. Per-rin, G.Y. Rathfon, J.H. Sumkin, M.L. Zuley, and A.I. Bandos. "Digital breast tomosynthesis: observer performance study," AJR Am J Roentgenol **193**, 586-591 (2009).

[36] K.K. Lindfors, J.M. Boone, T.R. Nelson, K. Yang, A.L.C. Kwan, and D.F. Miller. "Dedicated breast CT: initial clinical experience," Radiology **246**, 725-733 (2008).

[37] N.D. Prionas, K.K. Lindfors, S. Ray, S.Y. Huang, L.A. Beckett, W.L. Mon-sky, and J.M. Boone. 'Contrast-enhanced dedicated breast CT: initial clinical experience," Radiology **256**, 714-723 (2010).

[38] M. Freed, J.A. de Zwart, J.T. Loud, R.H. El Khouli, K.J. Myers, M.H. Greene, J.H. Duyn, and A. Badano. "An anthropomorphic phantom for quantitative evaluation of breast MRI," Med. Phys. accepted (2010).

[39] C. Kuhl. "The current status of breast MR imaging. Part I. Choice of technique, image interpretation, diagnostic accuracy, and transfer to clinical practice," Radiology **244**, 356-378 (2007).

[40] R. Katipamula, A.C. Degnim, T. Hoskin, J.C. Boughey, C. Loprinzi, C.S. Grant, K.R. Brandt, S. Pruthi, C.G. Chute, J.E. Olson, F.J. Couch, J.N. Ingle,

and M.P. Goetz. "Trends in mastectomy rates at the Mayo Clinic Rochester: effect of surgical year and preoperative MRI," J. Clin. Oncol. **27**, 4082-4088 (2009).

[41] M.A. Dinan, L.H. Curtis, B.G. Hammill, E.F. Patz Jr, A.P. Abernethy, A.M. Shea, and K.A. Schulman, "Changes in the use and costs of diagnostic imaging among Medicare beneficiaries with cancer 1999-2006," JAMA **303**, 1625-1631 (2010).

[42] K. Hede. "Preoperative MRI in breast cancer grows contentious," J. Natl. Cancer Inst. **101**, 1667-1669 (2009).

[43] N. Houssami and D.F. Haynes. "Review of preoperative magnetic resonance imaging (MRI) in breast cancer: should MRI be performed on all women with newly diagnosed, early stage breast cancer?," CA Cancer J/ Clin. **59**, 290-302 (2009).

[44] L.J. Solin. "Counterview: pre-operative breast MRI (magnetic resonance imaging) is not recommended for all patients with newly diagnosed breast cancer," Breast **19**, 7-9 (2010).

[45] D.M. Ikeda, N.M. Hylton, K. Kinkel, M.G. Hochman, C.K. Kuhl, W.A. Kaiser, J.C. Weinreb, S.F. SMazal, H. Degani, P. Viehweg, J. Barclay, amd M.D. Schnall. "Development, standardization, and testing of a lexicon for reporting contrast-enhanced breast magnetic resonance imaging studies," J. Magn. Reson. Imaging **13**, 889-895 (2001).

[46] American College of Radiology. *Breast imaging reporting and data system (BI-RADS) - MRI* (American College of Radiology, Reston, VA, 2003), 1st ed.

[47] P.S. Tofts, G. Brix, D.L. Buckley, J.L. Evelhoch, E. Henderson, M.V. Knopp, H.B. Larsson, T.Y. Lee, N.A. Mayr, G.J. Parker, R.E. Port, J. Taylor, and R.M. Weisskoff. "Estimating kinetic parameters from dynamic contrast-enhanced T(1)-weighted MRI of a diffusable tracer: standardized quantities and symbols," J. Magn. Reson. Imaging **10**, 223-232 (1999).

[48] S.G. Orel and M.D. Schnall. "MR imaging of the breast for the detection, diagnosis, and staging of breast cancer," Radiology **220**, 13-30 (2001).

[49] X. He, E.C. Frey, J.M. Links, K.L. Gilland, W.P. Segars, and B.M.W. Tsui. "A mathematical observer study for the evaluation and optimization of compensation methods for myocardial SPECT using a phantom population that realistically models patient variability," IEEE Trans. Nucl. Sci. **51**, 218-224 (2004).

[50] B.G. Steinbach, S.K. Hiskes, J.R. Fitzsimmons, and L. Lanier. "Phantom evaluation of imaging modalities for silicone breast implants," Invest. Radiol. **27**, 841-846 (1992).

[51] G.P. Mazzara, R.W. Briggs, Z. Wu, and B.G. Steinbach. "Use of a modified polysaccharide gel in developing a realistic breast phantom for MRI," Magn. Reson. Imaging **14**, 639-648 (1996).

[52] G.P. Liney, D.J. Tozer, and L.W. Turnbull. "A simple and realistic tissue-equivalent breast phantom for MRI," J. Magn. Reson. Imaging **10**, 968-971 (1999).

[53] P.R. Johnson and M.R.C. Greenwood. "The Adipose Tissue" in *Cell and Tissue Biology: A Textbook of Histology*, edited by L. Weiss (Urban and Schwarzenberg, Baltimore, 6th ed, 1988), pp. 193.

[54] B.D. Flickinger and N. Matsuo. "Diacylglycerols," in *Baileys industrial oil and fat products: Volume 3. Edible oil and fat products: specialty oils and oil products*, edited by F. Shahidi (John Wiley & Sons, Inc., Hoboken, New Jersey, 6th ed, 2005), p.38.

[55] U.S. Department of Agriculture, Agricultural Research Service, USDA National Nutrient Database for Standard Reference, Release 22. Nutrient Data Laboratory Home Page, http://www.ars.usda.gov/ba/bhnrc/ndl (2009).

[56] C.M. Nelson and M.J. Bissell. "Of extracellular matrix, scaffolds, and signaling: tissue architecture regulates development, homeostasis, and cancer," Annu. Rev. Cell Dev. Biol. **22**, 287-309 (2006).

[57] L. Ronnov-Jessen, O.W. Petersen, and M.J. Bissell. "Cellular changes involved in conversion of normal to malignant breast: importance of the stromal reaction," Physiol. Rev. **76**, 69-125 (1996).

[58] B. Weigert and M.J. Bissell. "Unraveling the microenvironmental influences on the normal mammary gland and breast cancer," Semin. Cancer Biol. **18**, 311-321 (2008).

[59] P.J. Keely, J.E. Wu, and S.A. Santoro. "The spatial and temporal expression of the $\alpha 2 \beta 1$ integrin and its ligands, collagen I, collagen IV, and laminin, suggest important roles in mouse mammary morphogenesis," Differentiation **59**, 1-13 (1995).

[60] K. Wolf, S. Alexander, V. Schacht, L.M. Coussens, U.H. von Andrian, J. van Rheenen, E. Deryugina, and P. Friedl. "Collagen-based cell migration models in vitro and in vivo," Semin. Cell Dev. Biol. **20**, 931-941 (2009).

[61] A.M. Campbell and D.V. Land. "Dielectric properties of female human breast tissue measured in vitro at 3.2 GHz," Phys. Med. Biol. **37**, 193-210 (1992).

[62] R.W. Burley and D.V. Vadehra. *The avian egg: chemistry and biology*, 1st ed. (John Wiley & Sons, Inc., New York, 1989), p.72, Table 4.3.

[63] E.G. Young. "Occurrence, classification, preparation and analysis of proteins," in *Comprehensive Biochemistry: Proteins (Part 1)*, edited by M. Florkin and E.H. Stotz (Elsevier Publishing Company, Amsterdam, 1st ed, 1963), p.28.

[64] Y. Mine. "Recent advances in the understanding of egg white protein functionality," Trends Food Sci. Technol. **6**, 225-232 (1995).

[65] A. Rinberg, E. Bågeman, C. Rose, C. Ingvar, and H. Jernstrm. "Of cup and bra size: reply to a prospective study of breast size and premenopausal breast cancer incidence," Int. J. Cancer **119**, 2242-2243 (2006).

[66] N. Maril, C.M. Collins, R.L. Greenman, and R.E. Lenkinski. "Strategies for shimming the breast, Magn. Reson. Med. **54**, 1139-1145 (2005).

[67] C. Klifa, J. Carballido-Gamio, L. Wilmes, A. Laprie, J. Shepherd, J. Gibbs, B. Fan, S. Noworolski, and N. Hylton. "Magnetic resonance imaging for secondary assessment of breast density in a high-risk cohort," MRI **28**, 8-15 (2010).

[68] R.H. Byrd, P. Lu, J. Nocedal, and C. Zhu. "A limited memory algorithm for bound constrained optimization," SIAM J. Sci. Comput. **16**, 1190-1208 (1995).

[69] J. Sijbers and A.J. den Dekker. "Maximum likelihood estimation of signal amplitude and noise variance from MR data," Magn. Reson. Med. **51**, 586-594 (2004).

[70] O.T. Karlsen, R. Verhagen, and W.M.M.J. Bovée. "Parameter estimation from rician-distributed data sets using a maximum likelihood estimator: application to T1 and perfusion measurements," Magn. Reson. Med. **41**, 614-623 (1999).

[71] J. Sijbers, A.J. den Dekker, E. Raman, and D. Van Dyck. "Parameter estimation from magnitude MR images," International Journal of Imaging Systems and Technology **10**, 109-114 (1999).

[72] P.B. Kingsley, R.J. Ogg, W.E. Reddick, and R.G. Steen. "Correction of errors caused by imperfect inversion pulses in MR imaging measurement of T1 relaxation times," MRI **16**, 1049-1055 (1998).

[73] P.B. Kingsley. "Signal intensities and T1 calculations in multiple-echo sequences with imperfect pulses," Concepts Magn. Reson. **11**, 29-49 (1999).

[74] M. Tashiro, N. Ishida, S. Shimotakahara, S. Tanabe, and A. Okubo. "Ontogenetic changes of the water status in the heated quails egg as studies by nuclear magnetic resonance imaging," Anal. Sci. **19**, 933-936 (2003).

[75] P.A. Bottomley, C.J. Hardy, R.E. Argersinger, and G. Allen-Moore. "A review of 1H nuclear magnetic resonance relaxation in pathology: are T1 and T2 diagnostic?," Med. Phys. **14**, 1-37 (1987).

[76] T.E. Merchant, G.R. Thelissen, P.W. de Graaf, C.W. Nieuwenhuizen, H.C. Kievit, and W. Den Otter. "Application of a mixed imaging sequence for MR imaging characterization of human breast disease," Acta Radiol. **34**, 356-361 (1993).

[77] S.J. Graham, S. Ness, B.S. Hamilton, and M.J. Bronskill. "Magnetic resonance properties of ex vivo breast tissue at 1.5 T," Magn. Reson. Med. **38**, 669-677 (1997).

[78] R. Rakow-Penner, B. Daniel, H. Yu, A. Sawyer-Glover, and G.H. Glover. "Relaxation times of breast tissue at 1.5T and 3T measured using IDEAL," J. Magn. Reson. Imaging **23**, 87-91 (2006).

[79] H.H. Barrett and K.J. Myers *Foundations of Image Science*, 1st ed. (John Wiley & Sons, Inc., New York, 2004).

[80] S.K. Park and Schowengerdt R.A. "Image reconstruction by parametric cubic convolution," Comput. Vision Graph. **23**, 258-272 (1983).

[81] J.T. Loud, A.C.M. Thibaut, A.D. Abati, A.C. Filie, K. Nichols, D. Danforth, R. Giusti, S.A. Prindiville, and M.H. Greene. "Ductal lavage in women from BRCA1/2 families: is there a future for ductal lavage in women at increased genetic risk of breast cancer?," Cancer Epidemiol. Biomarkers Prev. **18**, 12431251 (2009).

[82] S. Park, H. Liu, R. Jennings, R. Leimbach, I. Kyprianou, A. Badano, and K. Myers. "A task-based evaluation method for x-ray breast imaging systems using variable-background phantoms," Proc. SPIE **7258**, 72581L-1-72581L-9 (2009).

205

[83] D.R. Dance, R.A. Hunt, P.R. Bakic, A.D. Maidment, M. Sandborg, G. Ullman, and G. Alm Carlsson. "Breast dosimetry using high-resolution voxel phantoms," Radiat. Prot. Dosimetry **114**, 359-363 (2005).

[84] M.A. Hobson, E.L. Madsen, G.R. Frank, J. Jiang, H. Shi, T.J. Hall, and T. Varghese. "Anthropomorphic phantoms for assessment of strain imaging methods involving saline-infused sonohysterography," Ultrasound Med. Biol. **34**, 1622-1637 (2008).

[85] M. Freed, S. Miller, K. Tang, and A. Badano. "Experimental validation of Monte Carlo (MANTIS) simulated x-ray response of columnar CsI phosphor screens," Med. Phys. **36**, 11, 4944-4956 (2009).

[86] A.R. Cowen, S.M. Kengyelics, and A.G. Davies. "Solid-state, flat-panel, digital radiography detectors and their physical imaging characteristics," Clin. Radiol. **63**, 487-498 (2008).

[87] T. Jing, C.A. Goodman, J. Drewery, G. Cho, W.S. Hong, H. Lee, S.N. Kaplan, A. Mireshghi, V. Perez-Mendez, and D. Wildermuth. "Amorphous silicon pixel layers with cesium iodide converters for medical radiography," IEEE Trans. Nucl. Sci. **41**, 4, 903-909 (1994).

[88] V.V. Nagarkar, T.K. Gupta, S.R. Miller, Y. Klugerman, M.R. Squillante, and G. Entine. "Structured CsI(Tl) scintillators for x-ray imaging applications," IEEE Trans. Nuc. Sci. **45**, 3, 492-496 (1998).

[89] J. Kyprianou, A. Badano, B.D. Gallas, and K.J. Myers. "Singular value description of digital radiographic detector: Theory and measurements," Med. Phys. **35**, 10, 4744-4756 (2008).

[90] A. Badano, and J. Sempau. "Combined x-ray, electron, and optical Monte Carlo simulations of indirect radiation imaging systems," Phys. Med. Biol. **51**, 1545-1561 (2006).

[91] M.A. Mosleh-Shirazi, W. Swindell, and P.M. Evans. "Optimization of the scintillation detector in a combined 3D megavoltage CT scanner and portal imager," Med. Phys. **25**, 10, 1880-1890 (1998).

[92] A. Sawant, H. Zeman, S. Samant, G. Lovhoiden, B. Weinberg, F. DiBianca. "Theoretical analysis and experimental evaluation of a CsI(Tl) based electronic portal imaging system," Med. Phys. **29**, 6, 1042-1053 (2002).

[93] T.T. Monajemi, S. Steciw, B.G. Fallone, and S. Rathee. "Modeling scintillator-photodiodes as detectors for megavoltage CT," Med. Phys., **31**, 5, 1225-1234 (2004).

[94] P.M. Evans, M.A. Mosleh-Shirazi, E.J. Harris, and J. Seco. "Monte Carlo and Lambertian light guide models of the light output from scintillation crystals at megavoltage energies," Med. Phys. **33**, 6, 1797-1809 (2006).

[95] A. Sawant, L.E. Antonuk, Y. El-Mohri, Q. Zhao, Y. Wang, Y. Li, H. Du, and L. Perna. "Segmented crystalline scintillators: empirical and theoretical investigation of a high quantum efficiency EPID based on an initial engineering prototype CsI(Tl) detector," Med. Phys. **33**, 4, 1053-1066 (2006).

[96] J. Tickner, and G. Roach. "PHOTON - An optical Monte Carlo code for simulating scintillation detector responses," Nucl. Instrum. Meth. B **263**, 1, 149-155 (2007).

[97] J.C. Blakesley, and R. Speller. "Modeling the imaging performance of prototype organic x-ray imagers," Med. Phys. **35**, 1, 225-239 (2008).

[98] A. Badano, I.S. Kyprianou, R.J. Jennings, and J. Sempau. "Anisotropic imaging performance in breast tomosynthesis," Med. Phys. **34**, 11, 4076-4091 (2007).

[99] A. Badano, I.S. Kyprianou, M. Freed, R.J. Jennings, and J. Sempau. "Effect of oblique x-ray incidence in flat-panel computed tomography of the breast," IEEE Trans. Med. Imaging **28**, 5, 696-702 (2008).

[100] W. Zhao, G. Ristic, and J. A. Rowlands. "X-ray imaging performance of structured cesium iodide scintillators," Med. Phys. **31**, 9, 2594-2605 (2004).

[101] Radiation Management Service (business of Fluke Biomedical) product catalog, "Diagnostic Imaging" section. "X-Ray Pinhole Assemblies Models 07-611 to 07-633". www.flukebiomedical.com/rms (2005).

[102] A. Badano, J. Sempau, and R.J. Jennings. "Statistics of the scintillation output using a combined x-ray/electron/optical Monte Carlo method," Proc. SPIE **5045**, 361-365 (2005).

[103] A. Badano, J. Sempau, and J.S. Boswell. "Combined x-ray/electron/optical Monte Carlo code based on PENELOPE and DETECT-II," Proc. SPIE **5045**, 870-876 (2005).

207

[104] F. Salvat, J.M. Fernández-Varea, and J. Sempau. "PENELOPE-2006: A code system for Monte Carlo simulation of electron and photon transport," Nuclear Energy Agency (OECD) Issy-les-Moulineaux (2006). http://www.nea.fr.

[105] K. Cranley, B.J. Gilmore, G.W.A. Fogarty, and L. Desponds. "Catalogue of diagnostic x-ray spectra and other data", IPEM Report 78 (York: IPEM, 1997).

[106] J. G. Mainprize, A. K. Bloomquist, M. P. Kempston, and M. J. Yaffe. "Resolution at oblique incidence angles of a flat panel imager for breast tomosynthesis", Med. Phys., **33**, 9, 3159-3164 (2006).

[107] A. Badano. "Optical blur and collection efficiency in columnar phosphors for x-ray imaging," Nucl. Instrum. Meth. A **508**, 3, 467-479 (2003).

[108] A. Badano, I. S. Kyprianou, M. Freed, R. J. Jennings, and J. Sempau. "Effect of oblique x-ray incidence in flat-panel computed tomography of the breast," IEEE Trans. Med. Imaging **28**, 5, 696-702 (2009).

[109] A. Badano, I.S. Kyprianou, K.H. Tang, and A. Saha. "Validation of simulated point response of columnar phosphor screens," Proc. SPIE **6510** (2007).

[110] J. Kyprianou, A. Badano, B.D. Gallas, S. Park, and K.J. Myers. "A practical method for measuring the H matrix of digital x-ray and cone beam CT imaging systems," Proc. SPIE **6142** (2006).

[111] M. Freed, S. Park, and A. Badano. "A fast, angle-dependent, analytical model of CsI detector response for optimization of 3D x-ray breast imaging systems," Med. Phys. **37**, 6, 2593-2605 (2010).

[112] S. Richard, and J.H. Siewerdsen. "Cascaded systems analysis of noise reduction algorithms in dual-energy imaging," Med. Phys. **35**, 2, 586-601 (2008).

[113] G.K. Yadava, A.T. Kuhls-Gilcrist, S. Rudin, V.K. Patel, K.R. Hoffmann, and D.R. Bednarek. "A practical exposure-equivalent metric for instrumentation noise in x-ray imaging systems," Phys. Med. Biol. **53**, 18, 5107-5121 (2008).

[114] Y. Chen, J.Y. Lo, and J.T. Dobbins III. "Importance of point-by-point back projection correction for isocentric motion in digital breast tomosynthesis: Relevance to morphology of structures such as microcalcifications," Med. Phys. **34**, 10, 3885-3892 (2007).

[115] T. Wu, R.H. Moore, E.A. Rafferty, and D.B. Kopans. "A comparison of reconstruction algorithms for breast tomosynthesis," Med. Phys. **31**, 9, 2636-2647 (2004).

[116] A. Badano, I.S. Kyprianou, and J. Sempau. "Anisotropic imaging performance in indirect x-ray imaging detectors," Med. Phys. **33**, 8, 2698-2713 (2006).

[117] A. Badano, I.S. Kyprianou, R.J. Jennings, and J. Sempau. "Anisotropic imaging performance in breast tomosynthesis," Med. Phys. **34**, 11, 4076-4091 (2007).

[118] B.D. Gallas, J.S. Boswell, A. Badano, R.M. Gagne, and K.J. Myers. "An energy- and depth-dependent model for x-ray imaging," Med. Phys. **31**, 11, 3132-3149 (2004).

[119] J. Sempau, E. Acosta, J. Baró, J. M. Fernández-Varea, and F. Salvat. "An algorithm for Monte Carlo simulation of coupled electron-photon transport," Nucl. Instrum. Meth. B **132**, 377-390 (1997).

[120] D.J. Robbins. "On predicting the maximum efficiency of phosphor systems excited by ionizing radiation,' J. Electrochem. Soc. **127**, 12, 2694-2702 (1980).

[121] G. Knoll. *Radiation detection and measurement* (John Wiley and Sons, Inc., New York, NY, 2000).

[122] M. Freed, A. Badal, R.J. Jennings, H. de las Heras, K.J. Myers, and A. Badano. "X-ray properties of an anthropomorphic breast phantom for MRI and x-ray imaging," Phys. Med. Biol. submitted (2010).

[123] M.O. Leach, C.R. Boggis, A.K. Dixon, D.F. Easton, R.A. Eeles, D.G. Evans, F.J. Gilbert, I. Griebsch, R.J. Hoff, P. Kessar, S.R. Lakhani, S.M. Moss, A. Nerurkar, A.R. Padhani, L.J. Pointon, D. Thompson, R.M. Warren, et al. "Screening with magnetic resonance imaging and mammography of a UK population at high familial risk of breast cancer: a prospective multicentre cohort study (MARIBS)," Lancet **365**, 1769-1778 (2005).

[124] C.B. Caldwell and M.J. Yaffe. "Development of an anthropomorphic breast phantom," Med. Phys. **17**, 273-280 (1990).

[125] M.J. Yaffe, J.W. Byng, C.B. Caldwell, and N.R. Bennett. "Anthropomorphic radiological phantoms for mammography," Med. Prog. Technol. **19**, 23-30 (1993).

[126] G.J. Gang, D.J. Tward, J. Lee, and J.H. Siewerdsen. "Anatomical background and generalized detectability in tomosynthesis and cone-beam CT," Med. Phys. **37**, 1948-1965 (2010).

[127] S. Park, R.J. Jennings, H. Liu, A. Badano, and K.J. Myers. "A task-based evaluation method for three-dimensional x-ray breast imaging systems using variable-background phantoms," Med. Phys., in press (2010).

[128] Computerized Imaging Reference Systems Mammography BR3D Phantom, Norfolk, VA, USA, www.cirsinc.com

[129] A.K. Carton, P. Bakic, C. Ullbert, and A.D.A. Maidment. "Development of a 3D high-resolution physical anthropomorphic breast phantom," Proc. SPIE **7622**, 762206-1-762206-8 (2010).

[130] P.R. Bakic, M. Albert, D. Brzakovic, and A.D.A. Maidment. "Mammogram synthesis using a 3D simulation. I. Breast tissue model and image acquisition simulation," Med. Phys. **29**, 2131-2139 (2002).

[131] P.R. Bakic, M. Albert, D. Brzakovic, and A.D.A. Maidment. "Mammogram synthesis using a 3D simulation. II. Evaluation of synthetic mammogram texture," *Med. Phys.* **29** 2140-2151 (2002).

[132] P.R. Bakic, M. Albert, D. Brzakovic, and A.D.A. Maidment. "Mammogram synthesis using a three-dimensional simulation. III. Modeling and evaluation of the breast ductal network," Med. Phys. **30**, 1914-1925 (2003).

[133] C.M. Li, W.P. Segars, G.D. Tourassi, J.M. Boone, and J.T. Dobbins III. "Methodology for generating a 3D computerized breast phantom for empirical data," Med. Phys. **36**, 3122-3131 (2009).

[134] G.R. Hammerstein, D.W. Miller, D.R. White, M.E. Masterson, H.Q. Woodard, and J.S. Laughlin. "Absorbed radiation dose in mammography," Radiology **130**, 485-491 (1979).

[135] M. Freed, J.A. de Zwart, J.T. Loud, R.H. El Khouli, K.J. Myers, M.H. Greene, J.H. Duyn, and A. Badano. "An anthropomorphic phantom for quantitative evaluation of breast MRI," Med. Phys., accepted (2010).

[136] D.J. Thompson, M.O. Leach, G. Kwan-Lim, S.A. Gayther, S.J. Ramus, I. Warsi, F. Lennard, M. Khazen, E. Bryant, S. Reed, C.R. Boggis, D.G. Evans, R.A. Eeles, D.F. Easton, R.M. Warren, et al. "Assessing the usefulness of a novel MRI-based breast density estimation algorithm in a cohort of women at high genetic risk of breast cancer: the UK MARIBS study," Breast Cancer Res. **11** R80 (2009).

[137] P.C. Johns and M.J. Yaffe. "X-ray characterization of normal and neoplastic breast tissues," Phys. Med. Biol. **32**, 675-695 (1987).

[138] J.S. Al-Bahri and N.M. Spyrou. "Photon linear attenuation coefficients and water content of normal and pathological breast tissues," Appl. Radiat. Isot. **47**, 777-784 (1996).

[139] M.E. Poletti, O.D. Goncalves, and I. Mazzaro. "X-ray scattering from human breast tissues and breast-equivalent materials," Phys. Med. Biol. **47**, 47-63 (2002).

[140] A. Tomal, I. Mazarro, E.M. Kakuno, and M.E. Poletti. "Experimental determination of linear attenuation coefficient of normal, benign and malignant breast tissues," Radiation Measurements **45**, 1055-1059 (2010).

[141] P.S. Rao and E.C. Gregg. "Attenuation of monoenergetic gamma rays in tissues," Am. J. Roent. **123**, 631-637 (1975).

[142] A.E. Burgess. "Mammographic structure: data preparation and spatial statistics analysis," Proc. SPIE **3661**, 0277-786X (1999).

[143] J.M. Boone, T.R. Fewell, and R.J. Jennings. "Molybdenum, rhodium, and tungsten anode spectral models using interpolating polynomials with application to mammography," Med. Phys. **24**, 1863-1874 (1997).

[144] R.J. Jennings, P.W. Quinn, and T.R. Fewell. "Measured x-ray spectra for mammography," 43rd annual meeting of the AAPM **7129** (2001).

[145] M.J. Yaffe, J.M. Boone, N. Packard, O. Alonzo-Proulx, S.Y. Huang, C.L. Peressotti, A. Al-Mayah, and K. Brock. "The myth of the 50-50 breast," Med. Phys. **36**, 5437-5443 (2009).

[146] A. Badal "Development of advanced geometric models and acceleration techniques for Monte Carlo simulation in Medical Physics" *PhD dissertation* Universitat Politecnica de Catalunya (2008) ISBN: 978-84-691-6235-4 http://www.tesisenxarxa.net/TDX-0523108-095624

[147] J. Sempau, A. Badal, and L. Brualla. "penEasy and penEasyLinac, a penelope-based system for the Monte Carlo simulation of linacs and voxelised geometries. Application to far-from-the-axis fields," Med. Phys., submitted (2010).

[148] J.M. Boone, K.K. Lindfors, V.N. Cooper III, and J.A. Seibert. "Scatter/primary in mammography: comprehensive results," Med. Phys. **27**, 2408-2416 (2000).

[149] I. Sechopoulos, S. Suryanarayanan, S. Vedantham, C.J. D'Orsi, and A. Karellas. "Scatter radiation in digital tomosynthesis of the breast," Med. Phys. **34**, 564-576 (2007).

[150] J.P. Vallée, H.D. Sostman, and J.R. MacFall. "MRI quantitative myocardial perfusion with compartmental analysis: a rest and stress study," Magn. Reson. Med. **38**, 981-998 (1997).

[151] N. Wilke, M. Jerosch-Herold, Y. Wang, Y. Huang, B.V. Christensen, A.E. Stillman, K. Ugurbil, K. McDonald, and R.F. Wilson. "Myocardial perfusion reserve: assessment with multisection quantitative, first-pass MR imaging," Radiology **204** 373-384 (1997).

[152] J.P. Vallée, F. Lazeyras, L. Kasuboski, P. Chatelain, N. Howarth, A. Righetti, and D. Didier. "Quantification of myocardial perfusion with FAST sequence and Gd bolus in patients with normal cardiac function," J. Magn. Reson. Imaging **9** 197-203 (1999).

[153] M.K. Ivancevic, I. Zimine, F. Lazeyras, D. Foxall, and J.P. Vallée. "FAST sequences optimization for contrast media pharmacokinetic quantification in tissue," J. Magn. Reson. Imaging **14** 771-778 (2001).

[154] R.L. Perrin, M.K. Ivancevic, S. Kozerke, and J.P. Vallée. "Comparative study of FAST gradient echo MRI sequence: phantom study," J. Magn. Reson. Imaging **20** 1030-1038 (2004).

[155] B. Morgan, J.F. Utting, A. Higginson, A.L. Thomas, W.P. Steward, and M.A. Horsfield. "A simple, reproducible method for monitoring the treatment of tumors using dynamic contrast-enhanced MR imaging," Br. J. Cancer **94** 1420-1427 (2006).

[156] J.W. Chai, J.H. Chen, Y.H. Kao, J.R. Liao, C.C. Chen, S.K. Lee, and W.C. Chu. "Spoiled gradient-echo as an arterial spin tagging technique for quick evaluation of local perfusion," J. Mag. Reson. Imaging **16** 51-59 (2002).

[157] M.K. Ivancevic, I. Zimine, X. Montet, J.N. Hyacinthe, F. Lazeyras, D. Foxall, and J.P. Vallée. "Inflow effect correction in fast gradient-echo perfusion imaging," Magn. Reson. Med. **50** 885-891 (2003).

[158] B. Ebrahimi, S.D. Swanson, and T.E. Chupp. "A microfabricated phantom for quantitative MR perfusion measurements: validation of singular value decomposition deconvolution method," IEEE Trans. Biomed. Eng. **57** 2730-2736 (2010).

[159] J.H. Wang, C.V. Robinson, and I.S. Edelman. "Self-diffusion and structure of liquid water. III. Measurement of the self-diffusion of liquid water with H^2, H^3 and O^18 as tracers," J. Am. Chem. Soc. **75** 466-470 (1953).

[160] X. Fan, M. Medved, G.S. Karczmar, C. Yang, S. Foxley, S. Arkani, W. Recant, M.A. Zamora, H. Abe, and G.M. Newstead. "Diagnosis of suspicious breast lesions using an empirical mathematical model for dynamic contrast-enhanced MRI," Magn. Reson. Imaging **25** 593-603 (2007).

[161] G. Strich, P.L. Hagan, K.H. Gerber, and R.A. Slutsky. "Tissue distribution and magnetic resonance spin lattice relaxation effects of Gadolinium-DTPA," Radiology **154** 723-726 (1985).

[162] P.S. Tofts, B. Shuter, and J.M. Pope. "Ni-DTPA doped agarose gel - a phantom material for Gd-DTPA enhancement measurements," Magn. Reson. Imaging **11** 125-133 (1993).

[163] M.C. Schabel and D.L. Parker. "Uncertainty and bias in contrast concentration measurements using spoiled gradient echo pulse sequences," Phys. Med. Biol. **53** 2345-2373 (2008).

[164] H.L.M. Cheng. "Improved correlation to quantitative DCE-MRI pharmacokinetic parameters using a modified initial area under the uptake curve (mIAUC) approach," J. Magn. Reson. Imaging **30** 864-872 (2009).

[165] G. Hernandez, M.F. Tweedle, R.G. Bryant. "Proton magnetic relaxation dispersion in aqueous glycerol solutions of $Gd(DTPA)^{2-}$ and $Gd(DOTA)^{-}$," Inorg. Chem. **29** 5109-5113 (1990).

[166] J.B. Segur and H.E. Oberstar. "Viscosity of glycerol and its aqueous solutions," Ind. Eng. Chem. **43** 2117-2120 (1951).

[167] G.J. Stanisz and R.M. Henkelman. "Gd-DTPA relaxivity depends on macromolecular content," Magn. Reson. Med. **44** 665-667 (2000).

[168] H.J. Halpern, G.V.R. Chandramouli, E.D. Barth, C. Yu, M. Peric, D.J. Grdina, and B.A. Teicher. "Diminished aqueous microviscosity of tumors in murine models measured with in vivo radiofrequency electron paramagnetic resonance," Cancer Res. **59** 5836-5841 (1999).

[169] C. Peters-Engl, M. Medl, M. Mirau, C. Wanner, S. Bilgi, P. Sevelda, and A. Obermair. "Color-coded and spectral Doppler flow in breast carcinomas - relationship with tumor microvasculature," Breast Cancer Res. Treat. **47** 83-89 (1998).

[170] *CRC standard mathematical tables and formulae*, 30th Ed. Daniel Zwillinger Editor-in-Chief. (CRC Press, Washington D.C., 1996).

[171] B. Lazzari, G. Belli, C. Gori, and M.R. Del Turco. "Physical characteristics of five clinical systems for digital mammography," Phys. Med. Biol. **34**, 2730-2743 (2007).

[172] G. Poludniowski, G. Landry, F. DeBlois, P.M. Evans, and F. Verhaegen. "SpekCalc: a program to calculate photon spectra from tungsten anode x-ray tubes," Phys. Med. Biol. **54**, N433-N438 (2009).